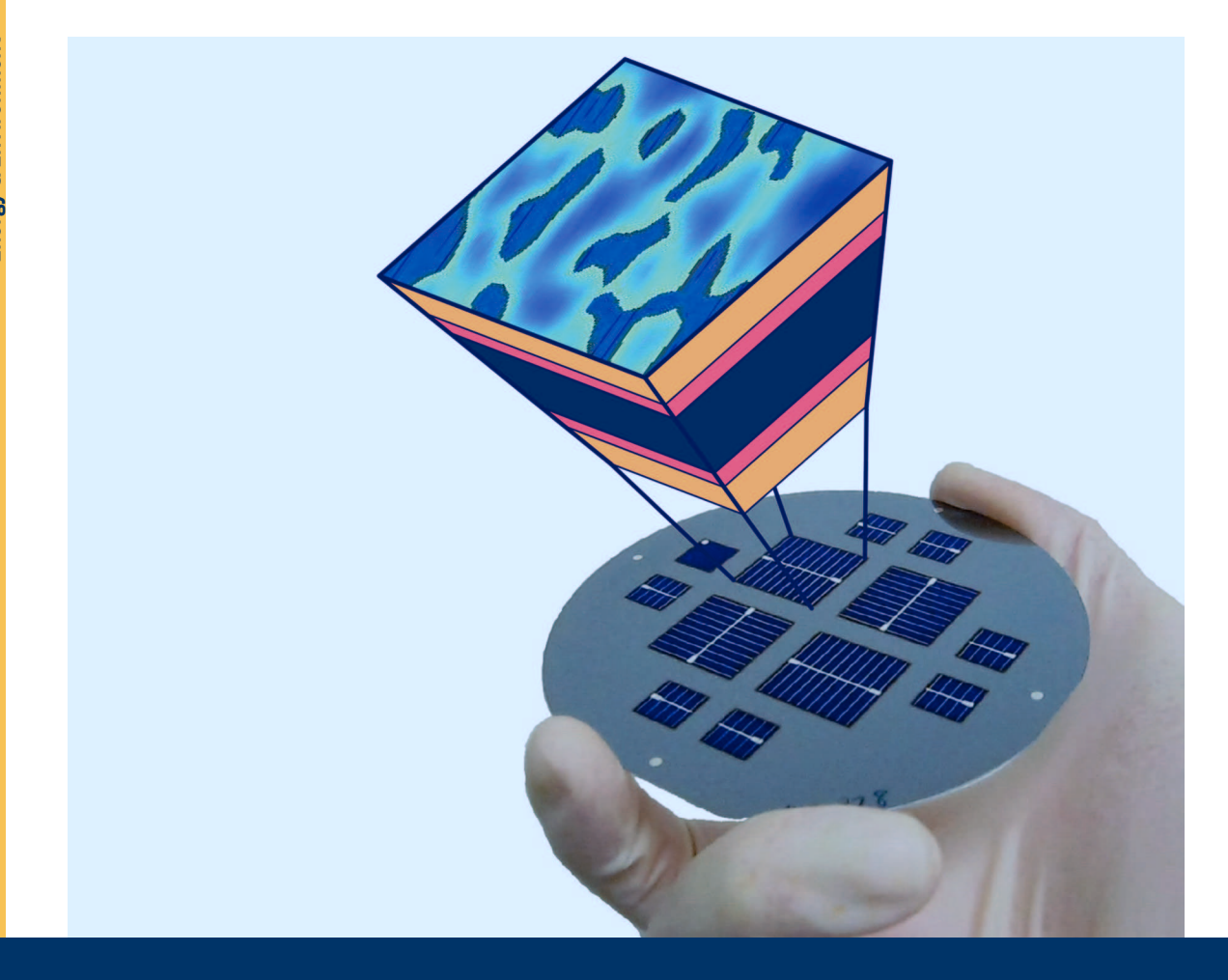
Energie & Umwelt Energy & Environment

Nanocrystalline Silicon Oxide in SHJ Solar Cells



416

Nanocrystalline Silicon Oxide in Silicon Heterojunction Solar Cells

Alexei Richter

Energie & Umwelt / Energy & Environment Band / Volume 416 ISBN 978-3-95806-310-5

ovei Dichte

Energie & Umwelt / Energy & Environment Band / Volume 416 ISBN 978-3-95806-310-5





Schriften des Forschungszentrums Jülich Reihe Energie & Umwelt / Energy & Environment

Band / Volume 416

Forschungszentrum Jülich GmbH Institut für Energie- und Klimaforschung IEK-5 Photovoltaik

Nanocrystalline Silicon Oxide in Silicon Heterojunction Solar Cells

Alexei Richter

Schriften des Forschungszentrums Jülich Reihe Energie & Umwelt / Energy & Environment Bibliografische Information der Deutschen Nationalbibliothek. Die Deutsche Nationalbibliothek verzeichnet diese Publikation in der Deutschen Nationalbibliografie; detaillierte Bibliografische Daten sind im Internet über http://dnb.d-nb.de abrufbar.

Herausgeber Forschungszentrum Jülich GmbH

und Vertrieb: Zentralbibliothek, Verlag

52425 Jülich

Tel.: +49 2461 61-5368 Fax: +49 2461 61-6103 zb-publikation@fz-juelich.de www.fz-juelich.de/zb

Umschlaggestaltung: Grafische Medien, Forschungszentrum Jülich GmbH

Grafische Medien, Forschungszentrum Jülich GmbH Druck:

Copyright: Forschungszentrum Jülich 2018

Schriften des Forschungszentrums Jülich Reihe Energie & Umwelt / Energy & Environment, Band / Volume 416

D 82 (Diss., RWTH Aachen University, 2018)

ISSN 1866-1793 ISBN 978-3-95806-310-5

Vollständig frei verfügbar über das Publikationsportal des Forschungszentrums Jülich (JuSER) unter www.fz-juelich.de/zb/openaccess.



This is an Open Access publication distributed under the terms of the Creative Commons Attribution License 4.0, which permits unrestricted use, distribution, and reproduction in any medium, provided the original work is properly cited.

Contents

Αŀ	ostrac	t	5
Zι	ısamı	nenfassung	9
1.	Intr	oduction	13
2.	Lite	rature review	17
	2.1.	Nanocrystalline silicon oxide	17
	2.2.	Silicon heterojunction solar cells	22
		2.2.1. Material research	26
		2.2.2. Device design	30
3.	Exp	erimental methods	33
	3.1.	Material and solar cell fabrication	33
	3.2.	Material characterization	38
	3.3.	Solar cell characterization	45
4.	Mat	erial development	51
	4.1.	Development of $<\!\!\mathrm{p}\!\!>$ nc-SiO_x:H at very high frequency	51
		4.1.1. Effect of deposition power and deposition pressure	52
		4.1.2. Optimization of the gas flows \hdots	56
	4.2.	Classification of nc-SiO_x:H films	60
		4.2.1. The deposition regions	61
		4.2.2. Microstructure of the nc-SiOx:H films	65
		4.2.3. Practical use of the model \hdots	71
	4.3.	Comparison of n- and p-type VHF/RF nc-SiO $_{\!x}:\!H$	75

Contents

5.	Plar	79			
	5.1.	a-SiO_x:H passivated solar cells	79		
		5.1.1. a-SiO _x :H passivation layers	80		
		5.1.2.	84		
		5.1.3. Rear-emitter SHJ solar cells	90		
	5.2.	a-Si:H passivated solar cells	91		
		5.2.1. Passivating crystalline Si wafers with $<\!\!i\!\!>$ a-Si:H \ldots	92		
		5.2.2.	94		
		5.2.3. OPAL 2 simulations of the front layer stack	99		
	5.3.	Nano-imprint lithography for anti-reflection coatings	103		
6.	Tex	tured silicon heterojunction solar cells	111		
	6.1.	a-Si:H passivation for textured solar cells	112		
	6.2.	nc-SiOx:H in textured SHJ solar cells	116		
		6.2.1. Successful implementation of nc-SiO $_{\rm x}:H$	116		
		6.2.2. Comparison to literature	120		
		6.2.3. Surface texture optimization via OPAL 2	123		
	6.3.	Stability of nc-SiO $_{\! x} : \! H$ SHJ solar cells	127		
7.	Sun	nmary and outlook	131		
	7.1.	Summary	132		
	7.2.	Outlook	138		
Α.	A. Symbols and abbreviations 141				
В.	List	147			
C.	Curi	149			
Re	References 1				
Αc	knov	165			

Abstract

To advance the contribution of photovoltaic (PV) systems in a transition towards fully sustainable energy generation, the costs of the associated systems need to decrease. In particular, a constant evolution of their solar energy conversion efficiency (η) is an effective way to reduce the overall costs of the energy production of a solar cell. In the recent decade high η have been achieved by the silicon heterojunction (SHJ) solar cell technology, which allows for a very high open circuit voltage ($V_{\rm oc}$). However, the parasitic absorptance ($A_{\rm paras}$) within the doped hydrogenated amorphous silicon (a-Si:H) layers still causes a significant reduction in the short circuit current density ($J_{\rm sc}$) of a SHJ solar cell. In contrast, thin films of hydrogenated nanocrystalline silicon oxide (nc-SiO_x:H) are significantly more transparent. This is related to their advantageous microstructure, in which a conductive network of crystalline silicon (c-Si) is combined with a silicon dioxide (SiO₂)-like matrix at the nanoscale. Nevertheless, a trade-off between a high conductivity and a high transparency has to be considered due to the conflicting properties of the two phases.

Accordingly, the aim of this thesis was to develop doped nc-SiO_x:H films at an increased deposition frequency (very high frequency (VHF)) to improve the optoelectronic trade-off of the films. Furthermore, these layers were applied in SHJ solar cells to achieve a low $A_{\rm paras}$ and, thereby, an enhanced $J_{\rm sc}$. Additionally, a continuous enhancement of η was accomplished by changes in the design of the solar cells.

In detail, films of nc-SiO_x:H were optimized at VHF using plasma enhanced chemical vapor deposition (PECVD). By exploiting the increased atomic H density at VHF, an improved phase separation was achieved in comparison to films deposited at radio frequency (RF) within the same deposition system and the devel-

oped films were comparable to the best-performing $\operatorname{nc-SiO}_x$:H films deposited at RF in literature. Within these variations four distinct regions of $\operatorname{nc-SiO}_x$:H deposition were identified according to their microstructure and their properties. In particular these are: a region of amorphous growth ("fully amorphous region"), a region with low amounts of the nanocrystalline silicon ($\operatorname{nc-Si}$) phase and the hydrogenated amorphous silicon oxide (a-SiO_x:H) phase ("onset of $\operatorname{nc-Si}$ formation"), $\operatorname{nc-SiO}_x$:H films of high $\operatorname{nc-Si}$ and $\operatorname{a-SiO}_x$:H phase contents ("O and $\operatorname{nc-Si}$ enrichment"), and a region with a preferential incorporation of $\operatorname{a-SiO}_x$:H against $\operatorname{nc-Si}$ (" $\operatorname{nc-Si}$ deterioration"). Particularly, films deposited at the transition between the "O and $\operatorname{nc-Si}$ enrichment" and the " $\operatorname{nc-Si}$ deterioration" region exhibited a high optoelectronic performance. A detailed investigation of the microstructure via atom probe tomography (APT) revealed the intricate three-dimensional structure of the $\operatorname{nc-Si}$ network and indicated a nearly homogeneous distribution of the dopant atoms across all phases in contrast to thermally produced $\operatorname{nc-Si}$ in SiO₂.

After the material development, the VHF nc-SiO_x:H layers were applied in SHJ solar cells. Starting with planar substrates passivated by intrinsic (<i>) a-SiO_x:H layers, n-type doped (<n>) nc-SiO_x:H front-emitter layers led to an increase in J_{sc} of the solar cells with an increasing a-SiO_x:H content in the nc-SiO_x:H layers. At the same time, highly transparent nc-SiO_x:H layers severely limited the fill factor (FF) of the solar cells. A significant enhancement of η was achieved by substituting the <i> a-SiO_x:H by <i> a-Si:H, which increased the open circuit voltage (V_{oc}) by about 20 mV due to a superior surface passivation of c-Si by the annealed a-Si:H layers. Furthermore, an improved nucleation of nc-Si on a-Si:H for nc-SiO_x:H in comparison to hydrogenated microcrystalline silicon (μ c-Si:H) layers was found by the deposition of nc-SiO_x:H front surface field (FSF) layers on a-Si:H passivated solar cells. Simulations using a freeware program for the optical analysis of the front surface of a solar cell (OPAL 2) indicated the thin nc-SiO_x:H layers deposited in solar cells to be more transparent than suggested by their optical properties determined from significantly thicker films.

To enhance the effect of using a nc-SiO_x:H FSF layer with a high optical band gap (E_{04}) , the reflectance (R) of the planar solar cells was reduced by the implementation of an anti-reflection (AR) coating. In detail, nano-imprint lithography (NIL)

was employed to produce a Si random pyramid textured SiO₂-like AR coating, which enhanced the light incoupling significantly and resulted in an increase of $J_{\rm sc}$. Overall, a planar SHJ solar cell with an active area solar energy conversion efficiency ($\eta_{\rm act}$) of 20.4% and a $J_{\rm sc}$ of 37.7 mA cm⁻² was produced.

The combination of an increased light incoupling and increased light trapping was achieved by Si random pyramid textured Si substrates. Here, the surface passivation of the absorber by <i> a-Si:H was confirmed to be comparable to the planar absorbers by considering the effect of the increased surface area and the absorber thickness. However, the nc-SiO_x:H films developed at VHF deteriorated the a-Si:H passivation layer by etching due to a high amount of atomic H during the deposition. A successful implementation of nc-SiO_x:H layers was possible by using RF and a lower H₂ flow to reduce the amount of atomic H. In total, a $\eta_{\rm act}$ of 21.4% was achieved with $V_{\rm oc} = 721\,\rm mV$, $FF = 75.4\,\%$, and $J_{\rm sc} = 39.4\,\rm mA\,cm^{-2}$. Furthermore, OPAL 2 simulations suggested an increase of $J_{\rm sc}$ by about 0.3 mA cm⁻² for implementing an inverted pyramid texture with a characteristic angle of 70° as compared to the Si random pyramid texture. Lastly, the performance of a SHJ solar cell with a nc-SiO_x:H FSF and emitter layer was subjected to a stability test. It degraded during storage in air for several months as well as under extended light exposure, which was partially reversible.

Zusammenfassung

Um den Beitrag von Photovoltaiksystemen (PV) zum Übergang zu einer vollständig nachhaltigen Energiegewinnung zu erhöhen, müssen die Kosten der entsprechenden Systeme gesenkt werden. Insbesondere die stetige Steigerung der Solarenergiewandlungseffizienz (η) bietet einen effektiven Weg, um die Gesamtkosten der Energiegewinnung einer Solarzelle zu reduzieren. In den vergangenen Jahrzehnten sind hohe η mit der Siliziumheterostruktur (SHJ) Technologie erreicht worden, welche sehr hohe offene Klemmspannungen ($V_{\rm oc}$) ermöglicht. Derzeit führt die parasitäre Absorption ($A_{\rm paras}$) in den dotierten amorphen Siliziumschichten (a-Si:H) jedoch zu einer erheblichen Verminderung des Kurzschlussstroms ($J_{\rm sc}$) einer SHJ Solarzelle. Im Gegensatz zum a-Si:H sind Dünnschichten aus nanokristallinem Siliziumoxid (nc-SiO_x:H) deutlich transparenter. Dies geht auf ihr vorteilhaftes Gefüge zurück, in der ein elektrisch leitfähiges Netzwerk aus kristallinem Silizium (c-Si) nanoskalig in einer Siliziumdioxid-ähnlichen Matrix eingebettet ist. Allerdings ist hier wegen der konträren Eigenschaften der beiden Phasen eine sorgfältige Abwägung zwischen einer hohen elektrischen Leitfähigkeit und einer hohen optischen Transparenz nötig.

Entsprechend war es ein Ziel dieser Arbeit, nc-SiO_x:H Schichten bei einer höheren Depositionsfrequenz (very high frequency (VHF)) zu entwickeln, um die optoelektronischen Eigenschaften der Schichten zu verbessern. Des Weiteren wurden diese Schichten in SHJ Solarzellen angewandt, um ein geringes $A_{\rm paras}$ zu erreichen und so $J_{\rm sc}$ zu erhöhen. Zudem wurde durch Anpassungen des Solarzellendesigns eine stetige Zunahme von η erreicht.

Zunächst wurden nc-SiO $_x$:H Schichten mittels plasmaunterstützter chemischer Gasphasenabscheidung (PECVD) bei VHF optimiert. Durch Nutzung der erhöhten Dichte an atomarem H bei VHF wurde eine verbesserte Phasentrennung im Vergleich zu Schichten erreicht, die im Hochfrequenzbereich (radio frequency (RF)) im

Zusammenfassung

gleichen Depositionssystem abgeschieden wurden. Außerdem waren die entwickelten Schichten auf vergleichbarem Niveau wie die besten RF nc-SiO_x:H Schichten in der Literatur. Innerhalb der variierten Parameter konnten vier einzelne Gebiete der nc-SiO_x:H Abscheidung nach ihren Schichteigenschaften und nach dem Gefüge unterschieden werden. Dies sind im Einzelnen: Ein Gebiet rein amorphen Wachstums ("fully amorphous region"), ein Gebiet mit geringen Anteilen an nanokristallinem Si (nc-Si) und amorphem Siliziumoxid (a-SiO_x:H) ("onset of nc-Si formation"), nc-SiO_x:H Schichten mit hohen Gehalten an nc-Si und a-SiO_x:H ("O and nc-Si enrichment") und ein Gebiet mit bevorzugtem Einbau von a-SiO_x:H zu Lasten von nc-Si ("nc-Si deterioration"). Insbesondere Schichten aus dem Übergangsgebiet zwischen den Gebieten "O and nc-Si enrichment" und "nc-Si deterioration" zeigten vielversprechende optoelektronische Eigenschaften. Eine detaillierte Untersuchung des Gefüges mittels Atomsondentomographie (APT) offenbarte die komplexe dreidimensionale Struktur des nc-Si Netzwerks und deutete auf eine nahezu homogene Verteilung der Dotieratome über alle Phasen hinweg. Dieser Befund steht im Gegensatz zu thermisch erzeugtem nc-Si in SiO_2 .

Nach der Materialentwicklung wurden die VHF nc-SiO_x:H Schichten in SHJ Solarzellen eingesetzt. Ausgehend von flachen Substraten, die mit intrinsischen (<i>) a-SiO_x:H Schichten passiviert wurden, führte n-typ dotiertes (<n>) nc-SiO_x:H als Frontemitterschicht zu einer Erhöhung des $J_{\rm sc}$ der Solarzellen mit steigendem Anteil an a-SiO_x:H in den nc-SiO_x:H Schichten. Allerdings wurde der Füllfaktor (FF)von Solarzellen mit hochtransparente nc-SiO_v:H Schichten erheblich durch letztere limitiert. Eine deutliche Verbesserung von η wurde durch eine Substitution von <i> a-SiO_x:H durch <i> a-Si:H erreicht, welches V_{oc} um ca. 20 mV erhöhte. Dies war Folge einer besseren Oberflächenpassivierung des c-Si durch die wärmebehandelten a-Si:H Schichten. Weiterhin wurde eine verbesserte Nukleation von nc-Si auf a-Si:H in nc-SiO_x:H Schichten im Vergleich zu mikrokristallinen Si (µc-Si:H) Schichten durch das Aufbringen von nc-SiO_x:H als "front surface field" (FSF) Schichten auf a-Si:H passivierten Solarzellen beobachtet. Simulationen mit Hilfe einer frei verfügbaren Software zur Simulation der Vorderseite von Solarzellen (OPAL 2) deuteten darauf hin, dass dünne nc-SiO_x:H Schichten, wie sie in Solarzellen angewandt werden, eine höhere Transparenz aufweisen als die optischen Eigenschaften deutlich dickerer Schichten es vermuten ließen.

Zur Steigerung der Wirkung von nc-SiO_x:H als FSF Schicht mit hoher optischer Bandlücke (E_{04}) wurde die Reflexion (R) der flachen Solarzellen durch die Aufbringung einer Anti-Reflexionsschicht (AR) verringert. Hierbei wurde die Nanoimprint Lithographie (NIL) genutzt, um eine SiO₂-ähnliche AR Schicht mit einer unregelmäßigen Si Pyramidentextur herzustellen, die die Lichteinkopplung in erheblichem Maße verbesserte und zu einer Zunahme im $J_{\rm Sc}$ führte. Insgesamt wurde eine flache SHJ Solarzelle hergestellt, die sich durch einen auf die aktive Fläche bezogenen Wirkungsgrad der Solarenergiewandlung $(\eta_{\rm act})$ von 20.4% und ein $J_{\rm Sc}$ von $37.7\,{\rm mA\,cm^{-2}}$ auszeichnete.

Eine Kombination aus einer Erhöhung der Lichteinkopplung und des Lichteinfangs wurde durch Substrate mit unregelmäßiger Si Pyramidentextur erreicht. Für diese wurde gezeigt, dass die Oberflächenpassivierung des Absorbers durch das <i> a-Si:H vergleichbar zu einem flachen Absorber ist, sofern die Erhöhung der Oberfläche durch die Textur und die Änderung der Absorberdicke berücksichtigt werden. Allerdings schädigten die bei VHF entwickelten nc-SiO_x:H Schichten die a-Si:H Passivierschichten durch Ätzen als Folge der hohen Dichte an atomarem H im Zuge der Deposition. Eine erfolgreiche Implementierung von nc-SiO_x:H Schichten konnte jedoch bei RF und einem verminderten H₂ Fluss erreicht werden, was in geringeren Mengen an atomarem H resultierte. Insgesamt wurde ein $\eta_{\rm act}$ von 21.4%mit $V_{\rm oc} = 721 \,\mathrm{mV}$, FF = 75.4% und $J_{\rm sc} = 39.4 \,\mathrm{mA \, cm^{-2}}$ erreicht. Weiterhin zeigten Simulationen mit OPAL 2 eine potentielle Erhöhung von $J_{\rm sc}$ um ca. $0.3\,{\rm mA\,cm^{-2}}$ auf, sofern eine Textur aus invertierten Pyramiden mit einem charakteristischem Winkel von 70° anstelle der unregelmäßigen Si Pyramidentextur realisiert wird. Schließlich wurde eine SHJ Solarzelle mit einer nc-SiO_x:H FSF Schicht und einer nc-SiO_x:H Emitterschicht einem Stabilitätstest unterzogen. Sie degradierte sowohl bei mehrmonatiger Lagerung unter Luft als auch unter dauerhafter Lichteinwirkung, was allerdings teilweise reversibel war.

1. Introduction

An ever increasing global demand of energy and a concurrent catastrophic impact on the environment dictate a transition to energy generation being chiefly supplied by renewable energy sources. A crucial and strongly increasing contribution to this energy generation is provided by photovoltaic (PV) systems. This was reflected in an increase of the globally installed PV capacity from 177GW in 2014 to about 227GW in 2015, making it the fastest growing renewable energy source worldwide [1]. Accordingly, electricity generated via PV systems is already available at a price comparable to the electricity obtained from the grid in several countries [1–3]. This development corresponds to the potential of PV systems as solar energy alone could already provide a multiple of the current annual global energy demand [4]. Nevertheless, the costs associated with PV electricity generation still need to decrease to finally supersede fossil fuel based energy production and lower the energy pay-back time associated with solar cell production [5].

A straightforward approach to decrease the overall costs of a PV system is to enhance the solar energy conversion efficiency (η) of the solar cells and modules and, thereby, enhance their energy yield. The most common terrestrial PV systems are based on Si solar cells. In particular, crystalline silicon (c-Si) based solar cells currently hold the main share in the PV market (93%) due the abundance of Si and ample experience with the fabrication and maintenance of the associated systems [6,7].

A highly promising technology among the c-Si based solar cells are the silicon heterojunction (SHJ) solar cells. This technology is based on the combination of the high quality Si absorber from common diffused Si solar cells and the various thin layers employed in Si thin-film solar cell fabrication. This combination offers a high η , while including the cost benefits of thin-film solar cells due to a low processing

1. Introduction

temperature and a simple fabrication sequence. The archetypical design of SHJ solar cells is based on thin doped and intrinsic hydrogenated amorphous silicon (a-Si:H) layers, which have resulted in an η up to 25.6% in 2014 [8]. While the intrinsic a-Si:H passivation layers have been attributed to the highest ever reported open circuit voltage $(V_{\rm oc})$ of 750 mV for a c-Si solar cell [9], the use of doped a-Si:H is debatable as it is accompanied by significant optical losses due to parasitic absorptance $(A_{\rm paras})$ of light in these layers. Therefore, appropriate substitutes have to be found for the doped a-Si:H layers to overcome this limitation and increase the short circuit current density $(J_{\rm sc})$ and, finally, η of SHJ solar cells. A promising candidate for this purpose is hydrogenated nanocrystalline silicon oxide (nc-SiO_x:H). This material combines the electrical conductivity of c-Si with the high optical transparency of silicon dioxide (SiO₂) through a phase mixture at the nanoscale. Thereby, these layers provide a similar conductivity as a-Si:H, while being more transparent.

The aim of this thesis is to advance the development of SHJ solar cells in combination with layers of doped nc-SiO_x:H to reduce the parasitic absorptance (A_{paras}) in the cells and increase η . Therefore, in a first part a detailed investigation is performed on the interplay between the deposition conditions during the plasma enhanced chemical vapor deposition (PECVD) of nc-SiO_x:H films and the microstructure of the films. In detail, the deposition of nc-SiO_x:H at very high frequency (VHF) is selected to improve the optoelectronic properties and optimize the trade-off between the conductivity and the transparency of the films. In a second part the newly developed nc-SiO_x:H layers with their improved material properties are applied in various functions in SHJ solar cells to explore the effects of these layers on the optical as well as the electrical performance of the solar cells. Furthermore, the effect of intrinsic ($\langle i \rangle$) hydrogenated amorphous silicon oxide (a-SiO_x:H) passivation layers is examined and the development of $\langle i \rangle$ a-Si:H passivation layers is briefly outlined. Additionally, both, the material development and the solar cell results, are critically reviewed with respect to literature data.

The following chapter, chapter 2, discusses recent results in the development and application of $nc\text{-}SiO_x$:H and presents the current research topics on SHJ solar cells. In Sec. 2.1 $nc\text{-}SiO_x$:H is introduced via a short historical summary. Next, the schematic microstructure of $nc\text{-}SiO_x$:H is presented and recent investigations

to reveal its true nature are discussed. Additionally, a short comparison to other commonly used thin film materials highlights the main advantages of $\operatorname{nc-SiO}_x$:H layers. Then, the numerous applications of $\operatorname{nc-SiO}_x$:H layers in Si thin-film (TF) and SHJ solar cells are discussed. In Sec. 2.2 the basics of SHJ solar cells are presented. Here, special focus is directed to the archetypical SHJ solar cell, based on a-Si:H layers. Section 2.2.1 focuses on the material research for SHJ solar cells with a special emphasis on the implementation of $\operatorname{nc-SiO}_x$:H. This section is followed by Sec. 2.2.2 presenting current developments in general design aspects of SHJ solar cells.

An introduction to the experimental methods employed in this thesis is given in **chapter 3**. This chapter is divided in a section on the material and the solar cell fabrication, a section on the characterization techniques of the material, and a section devoted to the experimental techniques used for solar cell characterization.

The experimental results of this work are presented in **chapter 4**, **chapter 5** and **chapter 6**. First, the development of $\operatorname{nc-SiO}_x$:H at VHF is discussed in **chapter 4**. This includes a variation of the deposition parameters during the PECVD and their effect on the properties and the structure of the $\operatorname{nc-SiO}_x$:H films (Sec. 4.1). The examined parameters encompass the deposition pressure (p), the deposition power (P), the PH₃ gas flow fraction (f_{PH_3}) , the B(CH₃)₃ gas flow fraction $(f_{B(CH_3)_3})$, the H₂ gas flow fraction (f_{H_2}) , and the CO₂ gas flow fraction (f_{CO_2}) . Next, a microstructure model for the classification of $\operatorname{nc-SiO}_x$:H films is introduced in Sec. 4.2 to facilitate the development of $\operatorname{nc-SiO}_x$:H films with an optimal phase composition. Explicitly, four distinct types of $\operatorname{nc-SiO}_x$:H films are described. Additionally, this section includes a detailed investigation of the microstructure of $\operatorname{n-type}$ doped $(<\operatorname{n-})$ and $\operatorname{p-type}$ doped $(<\operatorname{p-})$ $\operatorname{nc-SiO}_x$:H via atom probe tomography (APT). Lastly, in Sec. 4.3 a concluding overview of the deposited $\operatorname{nc-SiO}_x$:H films is presented and the properties of VHF $\operatorname{nc-SiO}_x$:H films are compared to $\operatorname{nc-SiO}_x$:H developed at radio frequency (RF).

Chapter 5 then covers the implementation of the newly developed nc-SiO_x:H layers in planar SHJ solar cells. This chapter is divided into 3 sections. First, Sec. 5.1 comprises investigations on a-SiO_x:H passivated SHJ solar cells including the effect of variations in the $\langle i \rangle$ a-SiO_x:H layer thickness on the solar cell performance. In

1. Introduction

a next step, the effect of varying $\operatorname{nc-SiO}_x$:H emitter layers is explored. The second section (Sec. 5.2) describes the development of <i> a-Si:H passivation layers in combination with annealing treatments, followed by their application in rear-emitter SHJ solar cells with a varying $\operatorname{nc-SiO}_x$:H front surface field (FSF) layer. Additionally, simulation results obtained from a freeware program for the optical analysis of the front surface of a solar cell (OPAL 2) are presented and compared to experimental results of SHJ solar cells using $\operatorname{nc-SiO}_x$:H layers. The third section discusses the use of nano-imprint lithography (NIL) generated anti-reflection (AR) coatings with a Si random pyramid texture for planar SHJ solar cells in combination with a varying $\operatorname{nc-SiO}_x$:H FSF layer (Sec. 5.3).

Textured a-Si:H passivated SHJ solar cells are discussed in **chapter 6**. In particular, the passivation of Si random pyramid textured Si wafers is examined in Sec. 6.1 and related to the results obtained on planar substrates. Section 6.2 focuses on the combination of nc-SiO_x:H layers with a-Si:H passivated textured SHJ solar cells. This includes a detailed comparison of the best-performing cell with similar SHJ solar cells reported in literature. Furthermore, the prospective implementation of an inverted pyramid texture is explored via OPAL 2 simulations. Then, the stability of the developed cells during storage and under extended light exposure (LE) is briefly examined in the last section of chapter 6 (Sec. 6.3).

The final **chapter 7** summarizes the main results obtained in this work and, in addition, presents multiple suggestions for future investigations on nc-SiO_x:H films and the possibilities of enhancing η of the SHJ solar cells employing advanced nc-SiO_x:H layers.

In this chapter a literature review is presented on recent investigations on hydrogenated nanocrystalline silicon oxide (nc-SiO $_{\rm x}$:H) and current research topics in the field of high efficiency silicon heterojunction (SHJ) solar cells. This includes the development of the associated materials as well as the exploration of novel device designs.

2.1. Nanocrystalline silicon oxide

Initial development Reports on a polycrystalline alloy of Si, N, and O were already published in 1976 [10]. These semi-insulating polycrystalline silicon (SIPOS) layers were introduced as a passivation layer in transistors and were produced via chemical vapor deposition (CVD). The structure of SIPOS layers was found to be mainly amorphous in the as-deposited state with very few regions of nanocrystalline silicon (nc-Si) of $1-2\,\mathrm{nm}$ in size [11]. Upon annealing at temperatures of up to $1200\,^{\circ}\mathrm{C}$ larger crystallites of nc-Si were found in an amorphous matrix and a phase separation into Si and silicon dioxide (SiO₂) was suggested. Later on, plasma enhanced chemical vapor deposition (PECVD) was used to prepare doped hydrogenated amorphous silicon oxide (a-SiO_x:H) films [12–15].

In 1993, for the first time a combination of a-SiO_x:H and hydrogenated microcrystalline silicon (μ c-Si:H) films was deposited via PECVD by adding carbon dioxide (CO₂) during the deposition of μ c-Si:H films [16]. Accordingly, these as-deposited films were termed hydrogenated microcrystalline silicon oxide (μ c-SiO_x:H) and provided an enhanced electrical conductivity (σ) with respect to a-SiO_x:H films due to the crystalline Si phase as compared to the hydrogenated amorphous silicon (a-Si:H) phase in the previously explored a-SiO_x:H films. A simplified representation of the

microstructure of μ c-SiO_x:H films is presented in Fig. 2.1 a). Usually, the microstructure of μ c-SiO_x:H films is illustrated as a highly conductive crystalline silicon (c-Si) phase being embedded in a matrix of an O-rich a-SiO_x:H phase with bonding arrangements resembling SiO₂ [17,18]. This phase separation into c-Si and an O-rich phase is thermodynamically driven and kinetically facilitated by the H₂-plasma even at a low substrate temperature ($T_{\rm sub}$) [18] in contrast to the thermally activated phase separation in the SIPOS films.

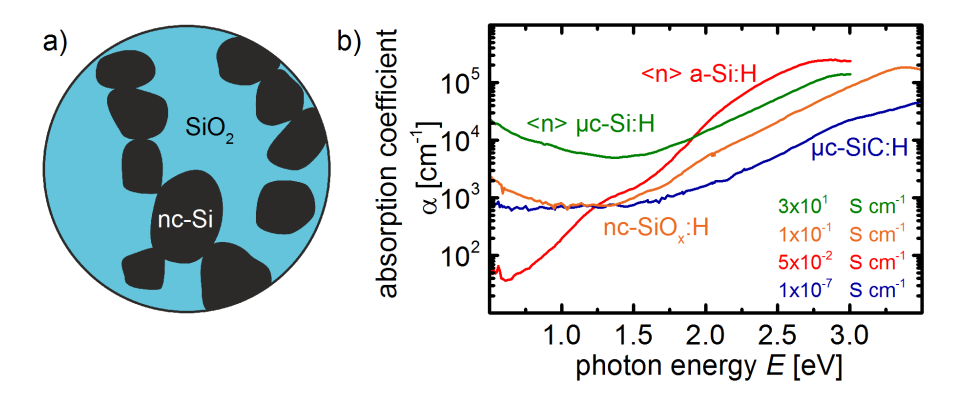


Figure 2.1.: a) Sketch of the microstructure of nc-SiO_x:H films consisting of a nc-Si phase and a SiO₂-like phase. b) Absorption spectra of n-type doped films deposited on glass substrates. The spectra were obtained via photothermal deflection spectroscopy (PDS) and the electrical dark conductivity (σ_D) of each layer is indicated in the bottom right. The spectra of the a-Si:H and μc -Si:H were taken from [19] and the μc -SiC:H spectrum from [20].

Microstructure Investigations on the microstructure of μ c-SiO_x:H suggested the existence of several tens of nm sized Si crystallites within the films [21]. More recently, more detailed investigations have been performed on μ c-SiO_x:H films with advanced characterization techniques. Here, chains of Si crystallites were found to grow anisotropically during the PECVD, with percolating chains of crystalline Si being oriented in the direction of film growth [17, 18, 22]. Conveniently, the orientation of these filaments coincides with the main direction of the electrical transport in solar cells. Additionally, the size of individual crystallites was found

to be less than 10 nm in most of the studies. Ever since then several investigations have found similar crystallite sizes for the crystalline Si phase [17, 22–24]. That is why, an increasing number of researchers have adopted the term of hydrogenated nanocrystalline silicon oxide (nc-SiO_x:H) for these films [22, 23, 25–27], although, generally both names can be used interchangeably.

The existence of additional phases in the microstructure of nc-SiO_x:H films is still under debate. Even in a configuration of Si clusters embedded in a-SiO $_{\rm x}$:H there would exist a low oxygen content (c_0) a-SiO_x:H "transition phase" due to the gradual shift of bonding arrangements from Si-Si to O-Si-O [28]. Therefore, the volume fraction of these low $c_{\rm O}$ regions is directly linked to the size and the number of the Si crystallites in the SiO₂-like phase. At a constant nc-Si volume fraction smaller crystallites would result in an increasing volume fraction of the "transition phase". However, this predicted relation has not been examined yet, especially as the nc-Si as well as the SiO₂ phase are difficult to identify unambiguously. Commonly, high resolution transmission electron microscopy (HRTEM) imaging is used to identify the nc-Si via the lattice fringes of the c-Si, while the O-rich a-SiO_x:H is distinguished by the O distribution determined via energy filtered transmission electron microscopy (EFTEM) images [17, 18, 22, 24]. However, these methods cannot examine the intermediate regions, which might consist of low c_{Ω} a-SiO_x:H or even show a thin a-Si:H shell around the nc-Si phase following the structure of a-SiO_x:H films. Additional characterization techniques are required to investigate the microstructure of nc-SiO_x:H films in more detail at the nm scale and complement the currently employed techniques

The amount of the nc-Si and the a-SiO_x:H phase can be controlled by adjusting the deposition parameters during the PECVD. Generally, an increase in the O-precursor gas leads to an increase in the a-SiO_x:H phase over the nc-Si phase, thereby increasing the optical band gap (E_{04}) and decreasing σ_D [17, 22, 29]. Contrary, a high H₂-dilution can facilitate the O incorporation as well as enhance the crystalline growth [30–32]. Furthermore, an increasing amount of H₂ in relation to the other gases has been reported to enhance the phase separation between the nc-Si and the a-SiO_x:H [22], but has also been related to a decrease of σ_D for very high H₂-dilutions [32]. The effect of a variation of the deposition pressure (p) and the

deposition power (P) was investigated by Gabriel et al. [33]. These authors found two different deposition regimes for n-type doped (< n>) nc-SiO_x:H films depending on the P/p ratio and achieved a simultaneous increase in $c_{\rm O}$ and the Raman crystallinity $(I_{\rm c})$ at a low P/p. This area of optimum properties was also related to a moderate availability of atomic H [33]. Beyond this optimum amount of atomic H, $I_{\rm c}$ decreased in combination with an increasing $c_{\rm O}$, while for very low amounts of atomic H a low $I_{\rm c}$ as well as a low $c_{\rm O}$ were reported.

Similarly to the SIPOS films, an alternative approach to produce nc-Si in combination with a SiO_2 matrix is to deposit a film of sub-stoichiometric silicon oxide (SiO_x) and achieve the phase separation via high temperature annealing [34–38]. These systems are often studied to investigate the relation between the size of the crystallites and the properties of the films. Furthermore, they are used as model systems for ab-initio modeling [38,39]. However, these structures do not show the pronounced anisotropy of the nc-Si growth reported for nc-SiO_x:H, which is a significant advantage for the application of nc-SiO_x:H in thin-film (TF) and SHJ solar cells.

In Si TF or SHJ solar cells nc-SiO_x :H layers mostly compete with layers of a-Si:H, $\mu \text{c-Si:H}$, or $\mu \text{c-SiC:H}$. A comparison of their optical and electrical properties is presented in Fig. 2.1 b). The presented a-Si:H and $\mu \text{c-Si:H}$ films have been successfully applied in TF solar cells [40], while the nc-SiO_x :H and the $\mu \text{c-SiC:H}$ films have been used in SHJ solar cells [20,41]. In comparison to the a-Si:H and $\mu \text{c-Si:H}$ films, nc-SiO_x :H exhibits a lower absorption coefficient (α) across the presented spectrum due to the a-SiO_x:H phase, while σ_D is still comparable owing to the nc-Si network. In contrast, the $\mu \text{c-SiC:H}$ film exhibits an even lower α than the nc-SiO_x :H due to the highly transparent SiC crystallites. However, σ_D of these layers is relatively low and still poses a considerable challenge in the implementation of $\mu \text{c-SiC:H}$ layers in high efficiency solar cells due to process compatibility issues [20]. Accordingly, doped layers of nc-SiO_x :H are a very promising material to substitute a-Si:H layers in SHJ solar cells in order to enhance the short circuit current density (J_{sc}), especially when considering that nc-SiO_x :H is also produced via PECVD and has been successfully applied by the Si TF solar cell industry.

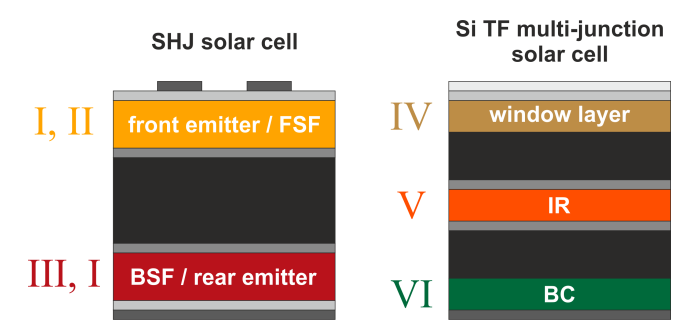


Figure 2.2.: Common positions of doped nc-SiO_x:H layers in various functions in silicon heterojunction (SHJ) and Si thin-film (TF) solar cells: I) front or rear emitter layer, II) front surface field (FSF), III) back surface field (BSF), IV) window layer, V) intermediate reflector (IR), and VI) back contact (BC) layer.

Applications Doped layers of nc-SiO_x:H have been applied in Si TF and SHJ solar cells with multiple functions [42, 43]. For TF solar cells they have been employed at the industrial scale due to the process compatibility (PECVD). The positions of these layers within the solar cells are sketched in Fig. 2.2. In a-Si:H and µc-Si:H single-junction TF solar cells <n> and p-type doped () nc-SiO_x:H layers can serve as transparent window layers reducing the parasitic absorptance (A_{paras}) and the reflectance (R) of the solar cells (IV in Fig. 2.2) [44]. For μ c-Si:H TF solar cells these window layers also serve as a nucleation layer for the c-Si phase within the intrinsic (<i>>) μc-Si:H absorber [44]. On the rear side of TF solar cells doped nc-SiO_x:H layers have been employed as back contact (BC) layers in a-Si:H single-junction [19, 45] and a-Si:H/ μ c-Si:H multi-junction TF solar cells (VI in Fig. 2.2) [29,46]. Here, they enhanced the external quantum efficiency (EQE) of these cells towards the infrared part of the light spectrum and reduced the parasitic absorptance (A_{paras}) in the metallic rear contact. Another application of nc-SiO_x:H for multi-junction TF Si solar cells was realized in intermediate reflectors (IR) (V in Fig. 2.2). These allow for an effective current matching between the individual sub-cells by adjusting the internal R within the multi-junction solar cell and can be used to reduce the thickness of sub-cells [32, 47].

Similarly to the Si TF solar cells, nc-SiO $_x$:H layers have found various applications in SHJ solar cells. The most common implementation is as the emitter layer at

the front of the solar cell (I in Fig. 2.2). <n> as well as nc-SiO_x:H layers have been developed for this purpose and were shown to significantly enhance the internal quantum efficiency (IQE) of these solar cells in the short wavelength (λ) region of the solar spectrum [25, 48, 49]. A similar function can be fulfilled by nc-SiO_x:H FSF layers in rear-emitter SHJ solar cells (II in Fig. 2.2). Rattanapan et al. [50] also investigated nc-SiO_x:H as a BSF (III in Fig. 2.2) layer and achieved an open circuit voltage (V_{oc}) of 659 mV and a fill factor (FF) of 80.9% without any additional passivation layer or even an transparent conductive oxide (TCO) on the rear of the solar cell.

Recently, novel applications of nc-SiO_x:H in c-Si solar cells have been suggested and explored. A passivating scheme for c-Si solar cells has been developed by Stuckelberger et al. [27]. Here, <n> nc-SiO_x:H were deposited on SiO₂ passivated Si substrates and capped with a thin layer of μ c-Si:H. Consecutively, a thermal annealing at temperatures up to 950 °C was applied to the symmetrically passivated samples. With this approach an implied open circuit voltage (iV_{0c}) up to 723 mV was achieved and an indiffusion of P was found from the nc-SiO_x:H into the Si absorber. The annealing step also affected the microstructure of the nc-SiO_x:H film by increasing I_c and the crystallite size of the nc-Si phase [27]. Nevertheless, the anisotropy of the nc-Si network was preserved. Even though the initial results are promising, the effectiveness of this approach is still to be demonstrated in a c-Si solar cell. Another application has been proposed by Chen et al. [51]. They employed a combination of <i> a-SiO_x:H and <n> nc-SiO_x:H as passivating layers during the anodic bonding of 1 µm thick c-Si absorbers. These layers were found to withstand the harsh processing conditions (250 °C, 1000 V) and effectively passivate the surface of this ultrathin absorber, in contrast to a conventional passivating scheme based on a-Si:H layers.

2.2. Silicon heterojunction solar cells

The basis of a heterostructure or heterojunction is the combination of two different materials with different electron affinities and band gaps. The difference in the electron affinity and band gap could arise from different chemical compositions or different states of matter and result in band offsets between the conduction band edge $(E_{\rm C})$ and the valence band edge $(E_{\rm V})$ at the interface between the materials (see also Fig. 2.3 b)).

The properties of the first heterostructure between a-Si:H and c-Si were reported in 1974 by Fuhs et al. [52], followed by the first a-Si:H-based SHJ solar cell produced by Hamakawa et al. in 1983 [53]. The most prominent developer of a-Si:H based SHJ solar cells in the following decades was the company Sanyo, Japan. This group also developed the concept of using a thin <i> a-Si:H layer to reduce the defect density at the surface of the c-Si wafer [54]. They named the concept "heterojunction with intrinsic thin layer" (HIT®) and the related patent was filed in 1993 [55]. The basic layout of the most common SHJ solar cell concept with <i> and doped a-Si:H layers is presented in Fig. 2.3 a). In principle, as well as <n> absorbers can be used, although commonly a higher solar energy conversion efficiency (η) has been achieved on $\langle n \rangle$ Si wafers [56] (see also Sec. 5.1.3). After a careful cleaning procedure the surface of the c-Si absorber is passivated by a thin <i> a-Si:H layer on both sides. Thereby, the defect density at the interface between the a-Si:H and the c-Si is reduced, resulting in a low recombination at this interface and ultimately a high $V_{\rm oc}$. Doped a-Si:H layers are used at the front and the rear side of the cells to create the p/n-junction or reduce recombination even further by selectively repelling charge carriers from the interface (field effect passivation). Furthermore, highly doped TCO layers are needed to provide a lateral collection of the generated charge carriers and reduce optical losses [2, 57]. Lastly, the charge carriers are collected by the metal grid and transported to the contacts.

The corresponding band diagram is sketched in Fig. 2.3 b). Please note that the valence band offset ($\Delta E_{\rm V}$) is larger than the conduction band offset ($\Delta E_{\rm C}$) for the a-Si:H/c-Si interface, especially for an increasing hydrogen content ($c_{\rm H}$) of the a-Si:H layer, e.g. $\Delta E_{\rm V}$ increases from about 0.4eV to 0.6 eV for an increase of $c_{\rm H}$ from 12 to 25 at.% as compared to a nearly constant $\Delta E_{\rm C}$ of about 0.3 eV [58,59].

In an operating device, electron/hole pairs generated within the c-Si absorber diffuse through the bulk until the holes are collected at the <p> a-Si:H side and the electrons at the <n> a-Si:H side of the solar cell. At the interface between the c-Si and the <i> a-Si:H band offsets affect the transport and recombination

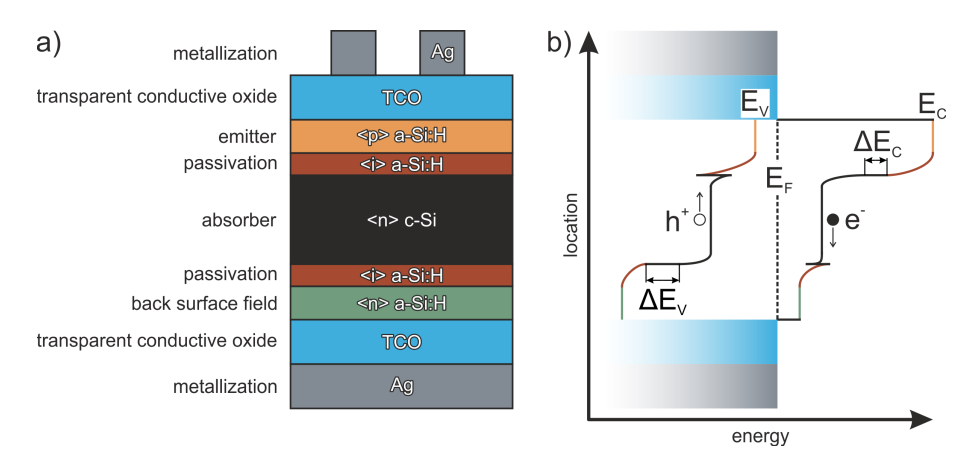


Figure 2.3.: a) Sketch of a typical silicon heterojunction (SHJ) solar cell. The individual layer thicknesses are not drawn to scale. b) Sketch of the corresponding band diagram, following Descoeudres et al. [56]. Here, E_C and E_V denote the conduction band edge and the valence band edge, respectively, while ΔE_C and ΔE_V represent the band offsets. E_F is the Fermi level and the directions of the electron and the hole collection are indicated as well. For simplicity, the band bending within the doped a-Si:H layers was not included and the TCO was approximated as a metallic layer.

of the charge carriers. In fact, numerical simulations by Fuhs et al. [59] suggested that an increasing $\Delta E_{\rm V}$ increases η of SHJ solar cells on <n> wafers due to the repelling effect of this band offset on the minority charge carriers (holes) from the defect rich a-Si:H/c-Si interface. They also pointed out that this might constitute an inherent advantage of <math><n> absorbers over <math><p> absorbers for SHJ solar cells employing a-Si:H layers [59]. The transport of charge carriers through the barriers imposed by the band offsets has been related to thermionic emission, direct or trap assisted tunneling [56,60–62]. A limitation of the charge carrier transport has especially been reported for passivation layers of <i>> a-SiO_x:H, which show an even larger $\Delta E_{\rm V}$ than a-Si:H layers [61]. At higher operating temperatures, however, this increased $\Delta E_{\rm V}$ can be overcome by enhanced thermionic emission of charge carriers and FF of corresponding devices is enhanced [63,64]. Furthermore, the electrical transport through the interface between the indium tin oxide (ITO) and the a-Si:H layers has been reported to strongly affect FF of SHJ solar cells, especially at the

 $ITO/\langle p \rangle$ a-Si:H interface [56, 60, 62].

In general, the presented SHJ solar cell concept has several advantages over classical c-Si solar cells with diffused junctions. First, the processing temperature of the SHJ solar cells is limited to about 200-220°C due to the a-Si:H layers, resulting in a lower energy consumption during the production. Second, the fabrication is simpler with less processing steps [5, 57]. Third, SHJ solar cells show a better performance than classical c-Si solar cells at elevated temperatures which increases their energy yield under realistic operating conditions. Fourth, the application of thin films allows for a high degree of freedom in the SHJ solar cell design. So, that alternative doped materials (see Sec. 2.1) and cell designs, like interdigitated back contact (IBC) [8] and bifacial [65] solar cell layouts, can be readily explored. Lastly, the photovoltaic (PV) industry is constantly striving to reduce the absorber thickness in c-Si solar cells to reduce the associated material costs per cell. Here, SHJ solar cells particularly benefit from a reduction of the absorber thickness due to the excellent surface passivation because the recombination of charge carriers at the surface of the absorber is dominating the overall recombination towards thinner absorbers. Therefore, SHJ solar cells could prove to be the relevant technology to approach the solar energy conversion efficiency limit of c-Si solar cells (29.4%), which has been predicted at a thickness of about 110 µm [66], while an absorber thickness of 180 µm is being used for most of the current c-Si solar cells [5,7].

Even today, the low surface recombination achieved by the well passivated absorber surface is the main feature of SHJ solar cells. Accordingly, the highest ever achieved $V_{\rm oc}$ of 750 mV for a c-Si solar cell [7] was reported by Taguchi et al. in 2013 [9] and an impressive world record η of 26.6% for c-Si solar cells was achieved by an IBC SHJ solar cell in 2017 [67,68]. Accordingly, these extraordinary results led to an increasing interest in the research of SHJ solar cell. The current research topics on the material and the cell level can be broadly devided into two groups. The first focuses on detailed investigation of the common materials and the development of new materials for SHJ solar cells, while the second group comprises research on the solar cell design and includes novel light management concepts and alternative contacting schemes.

2.2.1. Material research

a-Si:H passivation layers A major part of the material research for SHJ solar cells is dedicated to its most prominent aspect, the <i> a-Si:H passivation layer. The passivation mechanism of these layers is attributed to a termination of Si dangling bonds by atomic H [69].

Typically, a-Si:H passivation layers are deposited via PECVD from silane (SiH₄) and H₂ at a temperature around 200°C and at a pressure between 10 and 100Pa [57]. Controlling the deposition conditions is crucial to achieve a high passivation quality on c-Si with <i> a-Si:H. In fact, high effective carrier lifetime ($\tau_{\rm eff}$) have been reported for a-Si:H films deposited with SiH₄ depleted plasmas [70]. A high SiH₄ depletion can either be achieved by increasing the H₂ dilution of the SiH₄ or in pure SiH₄ plasmas by an appropriate adjustment of the deposition parameters [70]. Generally, a high SiH₄ depletion can be related to a deposition regime close to the amorphous/crystalline transition region [71] and has been reported to result in a high $\tau_{\rm eff}$ in the as-deposited state of the <i> a-Si:H [70, 72]. Furthermore, an atomically sharp interface between the a-Si:H and the c-Si is essential for a high $\tau_{\rm eff}$, while epitaxial growth of Si during the a-Si:H deposition deteriorates the passivation quality [73, 74], which can be revealed macroscopically by a decrease of $\tau_{\rm eff}$ upon annealing [75].

 $\rm H_{2}$ -plasma treatments have been reported to increase $\tau_{\rm eff}$ for a-Si:H passivated wafers. These treatments affect the microstructure of the deposited a-Si:H films. Firstly, $c_{\rm H}$ is increased. Secondly, the disorder within the a-Si:H layer is increased by a transition towards more H being bonded to Si at internal voids or interfaces in a mono-, di-, or trihydride configuration instead of a compact monohydride state [76,77]. Similarly, the disorder in a-Si:H films has been reported to increase towards the amorphous/crystalline transition region for μc -Si:H films [78]. So, $\rm H_{2}$ -plasma treatments can transform the microstructure of the a-Si:H films towards a void-rich structure, similarly to a-Si:H films deposited in SiH₄ depleted plasmas.

In contrast to the H₂-plasma treatment, thermal annealing of the a-Si:H at a constant annealing temperature (T_a) leads to a more compact structure within the a-Si:H as compared to the as-deposited state [73]. The accompanied increase of τ_{eff} is observed for fully amorphous a-Si:H passivation layers, even at annealing

temperatures below the deposition temperature [69]. Furthermore, thermal annealing has been reported to result in a relaxation of the amorphous network at the a-Si:H/c-Si interface towards the structure of the a-Si:H bulk [79]. Therefore, the (bulk) microstructure of the a-Si:H layers deposited close to the amorphous/crystalline transition region seems to be fundamentally different from the microstructure of annealed a-Si:H layers, even though excellent $\tau_{\rm eff}$ of several ms have been achieved with both approaches.

a-SiO_x:H passivation layers An alternative to a-Si:H passivation layers has been explored in <i> a-SiO_x:H. These layers were reported to yield good passivation of <n> and Si wafers [80,81] and have been successfully applied in SHJ solar cells with a $V_{\rm oc}$ of 716 mV for an $\langle n \rangle$ absorber [64]. The main benefit of $\langle i \rangle$ a-SiO_x:H lies in a higher E_{04} as compared to a-Si:H which results in a lower A_{paras} in the short λ range of light [49, 64, 82]. Additionally, a-SiO_x:H has been reported to be less prone to epitaxial growth of Si [83]. Correspondingly, a recent publication described the use of a thin a-SiO_x:H layer at the c-Si surface to prevent epitaxial growth during the following <i> a-Si:H deposition [84]. Moreover, <i> a-SiO_x:H passivation layers were reported to exhibit a higher temperature stability than a-Si:H layers [85]. Furthermore, <i> a-SiO_x:H layers were demonstrated to reduce the temperature coefficient of η in comparison to $\langle i \rangle$ a-Si:H due to an increasing FF with increasing temperatures [64]. This is in turn due to the high $\Delta E_{\rm V}$ between the c-Si and the a-SiO_x:H layers, which impedes the hole transport at these interfaces at room temperature [61,64]. Accordingly, FF of solar cells with a-SiO_x:H passivation layers was reduced with respect to the reference SHJ solar cells employing <i> a-Si:H [64]. Despite the numerous differences to the a-Si:H passivation layers, the main mechanism of surface passivation for $\langle i \rangle$ a-SiO_x:H layers is also attributed to chemical passivation of the dangling bonds via H [85]. Even though, the (positive) fixed charge carrier density has been reported to be higher in a-SiO_x:H films with respect to a-Si:H and could, therefore, result in a superior passivation quality on $\langle p \rangle$ wafers [81].

Doped layers Alternative materials to substitute the doped a-Si:H layers are being extensively explored as well. The main goal is to reduce the substantial A_{paras} of

the a-Si:H. A simple way to reduce A_{paras} is by depositing a thinner highly doped a-Si:H layer. However, V_{oc} and FF of the solar cell can be affected by a radical reduction in thickness and a lower limit of 3 nm was found for $\langle p \rangle$ a-Si:H [86].

Therefore, alternative materials are being explored as well, most of which have been mentioned in Sec. 2.1. However, a special emphasis should be directed towards the implementation and development of nc-SiO_x:H layers in SHJ solar cells. Early on, the application of <n> and <p> nc-SiO_x:H as emitter and BSF layers in SHJ solar cells was performed by the Tokyo Institute of Technology between 2008 and 2011 [50, 87, 88]. By the optimization of the nc-SiO_x:H layers an η of 18.5% was achieved by this group on a planar Si wafer. Later, Ding et al. [89] from Forschungszentrum Jülich GmbH (FZJ) demonstrated the effectiveness of a combined approach of a-SiO_x:H passivation layers and a nc-SiO_x:H emitter and BSF layer resulting in $\eta = 19\,\%$. Here, an optimal nc-SiO_x:H emitter thickness of 20 nm was found similarly to the results of Sritharathikhun et al. [88]. The optimized <n> nc-SiO_x:H emitter layer was characterized by $E_{04} = 2.2\,\text{eV}$, $\sigma_{D} = 10^{-3}\,\text{S}\,\text{cm}^{-1}$, $I_{c} = 36\,\%$, and $c_{O} = 24\,\text{at.}\%$.

More recently, $\langle p \rangle$ nc-SiO_x:H emitters were used by the Helmholtz-Zentrum Berlin für Materialien und Energie (HZB) to maximize $J_{\rm sc}$ of SHJ solar cells and a aperture area $J_{\rm sc}$ of 40.4mAcm⁻² and $\eta = 20.3\%$ was achieved by the application of a $\langle p \rangle$ nc-SiO_x:H emitter layer with $E_{04} = 2.2\,\mathrm{eV}$ in combination with an optical optimization of the front layer stack on textured wafers. However, the applied nc-SiO_x:H layer severely limited FF of the solar cell to 73% due to a $\sigma_{\rm D}$ of $10^{-7}\,\mathrm{S\,cm^{-1}}$, even though a μ c-Si:H contact layer was used towards the ITO interface [25]. Therefore, this study highlighted the possible gains in $J_{\rm sc}$ achievable by nc-SiO_x:H layers and, simultaneously, described the challenges in implementing highly transparent, especially $\langle p \rangle$, nc-SiO_x:H layers.

In a next step, several approaches were explored to improve FF of the solar cells by investigating the current transport at the $ITO/ nc-SiO_x$:H interface [60] and enhancing the nucleation of the nc-Si phase via a CO_2 -plasma treatment of the a-Si:H passivation layer [90]. Furthermore, the effect of a nc-Si deposition on an underlying <i> a-Si:H layer was investigated [91]. A high H_2 dilution was found to deteriorate the passivation quality of a-Si:H layers as soon as any epitaxial Si

was present in the passivation layers. Therefore, a chemical annealing effect was attributed to the H-rich deposition conditions, similarly to $\rm H_2$ -plasma treatments. These results could also prove to be crucial for $\rm nc\textsc{-}SiO_x$:H layer depositions due to the excellent optoelectronic properties achieved at high H₂ dilution [40]. The highest η of 21% was achieved for a SHJ solar cell with a \rm nc-Si emitter, deposited after a CO₂-plasma treatment of the $\rm < i>$ a-Si:H layer to enhance the nucleation of the nc-Si [91].

A third approach to reduce $A_{\rm paras}$ in SHJ solar cells has been presented in a recent study. Here, fully dopant-free heterocontact layers with high band gaps were demonstrated in high efficiency SHJ solar cells. In particular the effectiveness of molybdenum oxide (${\rm MoO_x}$) and lithium fluoride (${\rm LiF_x}$) were demonstrated as a hole-and an electron-selective contact layer, respectively [92]. Here, the carrier selectivity was purely achieved by an appropriate energy band alignment at the heterointerfaces due to the differences in the work functions of the materials. Another candidate for an undoped hole-selective layer is tungsten oxide (${\rm WO_x}$). However, a challenge still lies in accurately controlling the amount of O-vacancies to achieve a suitable work function and conductivity of the ${\rm WO_x}$ [93].

Transparent conductive oxides Another major challenge lies in the development of the TCO layers. On the one hand, studies focus on optimizing the electrical and optical properties of the most prominent TCO material for SHJ solar cells, ITO [94–97]. Here, a trade-off between a low A_{paras} for a low electron density (n_{e}) and a high σ for a high n_{e} has usually to be considered, especially at the front of the solar cell where lateral carrier transport within the ITO is crucial [96]. Contrary, optical considerations are more important for a TCO that is part of a fully metallized rear contact [97]. It is often argued that the use of In might limit the cost competitiveness of the SHJ solar cell technology. However, a recent study attributed the In costs to be only about 30% of the overall costs of the ITO deposition [5].

On the other hand, alternative TCOs with a higher Hall electron mobility (μ_e) are being investigated in SHJ solar cells to achieve a lower n_e while keeping σ at the same level. Potential candidates are Al- or B-doped zinc oxide [57] or hydrogen doped indium oxide (IOH) [98]. Especially IOH has shown μ_e up to $120 \, \mathrm{cm}^2 \, (\mathrm{V \, s})^{-1}$

and a significant reduction of $A_{\rm paras}$ in SHJ solar cells in comparison to ITO. However, Barraud et al. [98] found that a thin contacting layer of ITO is needed towards the screen printed Ag grid to achieve a good contact between the IOH and the Ag grid. Another potential substitute for ITO without this disadvantage is indium zinc oxide (IZO). Recently this amorphous material has been reported to yield μ_e up to $60\,\mathrm{cm}^2\,\mathrm{(Vs)}^{-1}$ even in the as-deposited state and has been demonstrated to enhance J_{sc} and FF of SHJ solar cells in comparison to reference cells using ITO [99].

Metallization The a-Si:H films of SHJ solar cells limit their processing temperatures to around 200 °C. Accordingly, high curing temperatures to achieve a highly conductive metal grid after screen printing are not feasible. Nevertheless, a FF of 83.2% was achieved in a SHJ solar cell by a screen-printed low temperature Ag paste by Panasonic, even though they admitted that the conductivity of their contacting scheme was still inferior to a conventional metal grid used for diffused c-Si solar cells [9]. To mitigate the resistance losses due to the low conductivity of the metal grid additional busbars can be used [57]. More conductive metal grids for SHJ solar cells can also be achieved via different metallization techniques like stencil printing, electroplating or thin metallic wires [57]. For instance, an electroplated grid was used for the high efficiency SHJ solar cell of Panasonic ($\eta = 25.6\%$) [8].

Another important aspect of the metallization are the high costs associated with the Ag grid. A possible substitute is Cu. According to Louwen et al. [5], replacing the Ag by a Cu paste could decrease the module costs of SHJ solar cells by about 5%. Furthermore, the presented alternative metallization techniques might result in an additional cost advantage by eliminating the need for the expensive low temperature metallic pastes altogether [5].

2.2.2. Device design

Apart from the development of the applied materials, considerable effort has been directed towards exploring novel design concepts of SHJ solar cells.

Light management Effective light incoupling and light trapping are essential prerequisites for high efficiency Si solar cells. This is especially important for thin absorber materials due to the low absorption of light by Si. An extremely effective approach to minimize the reflection losses and, thereby, maximize the light incoupling is the so-called black silicon (b-Si). b-Si is the collective term for a nanostructured surface texture of Si with nanocones, nanorods or nanoscale pores [100]. This nanotexture reduces R of the Si close to zero across the full sun spectrum without the need for an additional anti-reflection (AR) coating. At the same time, the surface area of the textured surface is greatly enlarged which results in an enhanced recombination of generated charge carriers at the surface and a reduced $V_{\rm oc}$ of the solar cell [101]. Recently, however, an effective passivation of a b-Si texture was achieved by Al₂O₃-passivation via atomic layer deposition in a diffused c-Si solar cell, yielding an η of 22.1% and a $V_{\rm oc}$ of 665 mV [100].

To increase the light trapping in Si solar cells, nanophotonic light trapping contacts could yield a significant enhancement of $J_{\rm sc}$ for absorber thicknesses below 100 μ m without increasing the surface area of the absorber and, thereby, maintaining the high $V_{\rm oc}$ of SHJ solar cells. Prototype SHJ solar cells were successfully demonstrated by Smeets et al. [102].

Alternative design concepts A straightforward method to increase $J_{\rm sc}$ of a solar cell is to eliminate the shadowing losses of the metal grid at the front of the cell. Accordingly, the concept of interdigitated back contact (IBC) solar cells was developed by Lammert and Schwartz in 1977 [103]. Initially developed for concentrator solar cells, this design concept has recently gained renewed attention due to the impressive results achieved by Panasonic ($\eta = 25.6\%$) [8] and Kaneka ($\eta = 26.3\%$) [68,104] for IBC SHJ solar cells.

A significant reduction in shadowing losses can also be achieved by the metal wrap through (MWT) cell design. It is based on metal filled holes ("vias") being created in the cell and providing a way to contact the front grid at the rear side of the solar cell. This leads to a reduced current in the busbars at the front of the solar cell and, therefore, the option to use thinner busbars. Additionally, this concept benefits from a lower cell to module loss in η due to the elimination of cell interconnecting

tabs at the front. The successful implementation of the MWT concept in SHJ solar cells has been demonstrated by Coletti et al. ($\eta = 23.1\%$) [105].

Another radical change in solar cell design is offered by the previously mentioned dopant-free heterocontacts. These layers, e.g. ${\rm MoO_x}$ and ${\rm LiF_x}$, allow for simpler deposition of the selective contact layers and could overcome the limitations imposed by the doped a-Si:H layers, e.g. $\Delta E_{\rm V}$ [92,106]. Furthermore, they eliminate the recombination active defects introduced via doping [2]. Especially in combination with the excellent passivating properties of <i>a-Si:H layers, promising results were achieved with ${\rm MoO_x}$ and ${\rm LiF_x}$ layers in a concept referred to as the dopant-free asymmetric heterocontacts (DASH) [92]. Therefore, the use of dopant-free heterocontacts could potentially help to approach the theoretical limiting efficiency of 29.4% for a 110 μ m thick Si solar cell [66].

3. Experimental methods

In this chapter the experimental methods to produce and characterize the materials and the solar cells will be introduced and described. The first section deals with the deposition systems which were used to fabricate the material samples and the various components of the solar cells. In the second section a brief overview is given on the material characterization techniques, their basic principles and measurement parameters. Then, the third section gives a description of the measurement techniques used for the characterization of solar cells in this work.

3.1. Material and solar cell fabrication

Plasma enhanced chemical vapor deposition (PECVD) PECVD belongs to the group of chemical vapor deposition (CVD) techniques. These have in common that the precursor is supplied in a gaseous state and is decomposed by an external energy supply to reform chemical bonds on a given substrate. For PECVD the energy to decompose the gases is supplied by an alternating current (AC) discharge between two electrodes creating a plasma.

In this study, PECVD was used to produce hydrogenated amorphous silicon oxide (a-SiO_x:H), hydrogenated nanocrystalline silicon oxide (nc-SiO_x:H), and hydrogenated amorphous silicon (a-Si:H) films. The former two materials were deposited in a multi-chamber deposition system manufactured by MRG Inc. The same PECVD chamber was used for n-type doped (<n>) and p-type doped (<p>) films with a chamber volume of about $27 \, \text{dm}^3$. The substrate electrode distance was set to 16 mm with an electrode area of about $150 \, \text{cm}^2$ and the gas was injected in cross-flow configuration. Furthermore, the films were deposited at a heater temperature ($T_{\rm H}$) of $235^{\circ}{\rm C}$, corresponding to a substrate temperature ($T_{\rm sub}$) of $200^{\circ}{\rm C}$. A

base pressure of at least 10^{-6} Pa was targeted within the chamber prior to deposition. The process gases for intrinsic (<i>) layers were silane (SiH₄), hydrogen (H₂), and carbon dioxide (CO₂). In addition, phosphine (PH₃), diluted to 5% in SiH₄, and trimethylborane (B(CH₃)₃), diluted to 2.54% in He, were supplied for <n> and <p> doping, respectively. The a-Si:H passivation layers were deposited in a PECVD chamber of a multi-chamber system manufactured by FAP GmbH and Von Ardenne GmbH. This chamber (16 dm³) was equipped with a 210 cm² shower head electrode, through which the gas precursors were injected, and was solely used for the deposition of <i> a-Si:H layers. The electrode spacing (d_{el}) was set to 23 mm and the depositions were performed at a density of the deposition power of about $18\,\mathrm{mWcm^{-2}}$ and a deposition pressure (p) of $100\,\mathrm{Pa}$. Here, only SiH₄ and H₂ were used as precursor gases.

Magnetron sputtering Sputtering belongs to the class of physical vapor deposition (PVD) techniques. These encompass all deposition conditions where physical processes are used to eject particles from a solid target to be transferred to a substrate. Typically, no chemical reactions are taking place during these depositions. Similarly to PECVD, an electrical discharge is used to provide energy to a gas, which is mostly inert, thereby creating a plasma. However, a direct current (DC) is used in combination with a high bias voltage (V_{bias}) to accelerate ions from the gas towards the target. Due to the collisions of these plasma particles with the solid target material, some particles of the target material are ejected towards the substrate and recondense on the surface of the substrate. In addition to the electrical field, in magnetron sputtering, a magnetic field is applied around the target. This magnetic field mainly controls the trajectory of the electrons within the plasma and results in an increased electron density along these paths. With this technique the ionization of the inert gas is enhanced, which leads to a higher sputtering rate and allows for lower deposition pressures, which in turn yield less porous films.

In the course of this work, magnetron sputtering was used to deposit indium tin oxide (ITO) as a transparent conductive oxide (TCO) on the silicon heterojunction (SHJ) solar cells. Hereby, the ITO was sputtered after 10 min of presputtering either at room temperature (RT) or at a $T_{\rm H}$ of 125°C after 1h of preheating. An ITO target with 5 wt. % tin dioxide (SnO₂) was used in an atmosphere of Ar (27 sccm) and 1%

oxygen (O_2) in Ar (3 sccm) at a p of 50 mPa. The deposition power (P) was set to 100 W and V_{bias} to 120 V. Additionally, the substrate was rotated at 5 rpm to provide a more homogeneous film deposition.

Thermal evaporation Another technique belonging to the group of PVD is thermal evaporation. Here, the energy required to transfer material to the substrate is provided by heating. For this, the target material was placed in a W boat in a vacuum chamber. At a pressure below 3×10^{-3} Pa a high electrical current was driven through the boat, heating it beyond the evaporation temperature of the target material. From the gas phase the material is then deposited evenly on the interior of the chamber including the substrate. A piezoelectrical crystal was placed close to the substrate and used to monitor the deposition rate of the target material by a change in the vibration frequency of the crystal due to the added mass.

In this work, evaporation was used to deposit silver contacts on the material samples and the solar cells by using stainless steel shadow masks. For material characterization two rectangular coplanar contacts of $5x3.5\,\mathrm{mm}^2$ were evaporated in a distance of $0.5\,\mathrm{mm}$ and with a thickness of $700\,\mathrm{nm}$. The evaporated Ag grid of the solar cells is described in detail in Sec. 5.1.1.

Cell fabrication An overview of the processing steps of a front-emitter SHJ solar cell is shown in Fig. 3.1. The first step is surface cleaning of the substrate. For double side polished float-zone (FZ) wafers this comprises of a 10 min oxidation of surface contaminants by a mixture of hydrogen peroxide and sulfuric acid followed by a removal of the oxide layer by 1% diluted hydrofluoric acid (HF) for 2 min. For the Si pyramid textured Czochralski (CZ) wafers the cleaning was reduced to the HF treatment, while extending the cleaning time to 5 min. Within the next 15 min the wafer was loaded into the PECVD system to prevent re-oxidation. Then the front passivation layer was deposited, after preheating the wafer for at least 1h in vacuum for a <i>> a-SiO_x:H passivation or a 5 min preheat in a H₂ atmosphere for a <i>> a-Si:H passivated cell. Subsequently, the wafer was quickly rotated in the hot state in ambient air, followed by another preheat step and the deposition of the back passivation layer. The <n>> nc-SiO_x:H layer was deposited next and the wafer

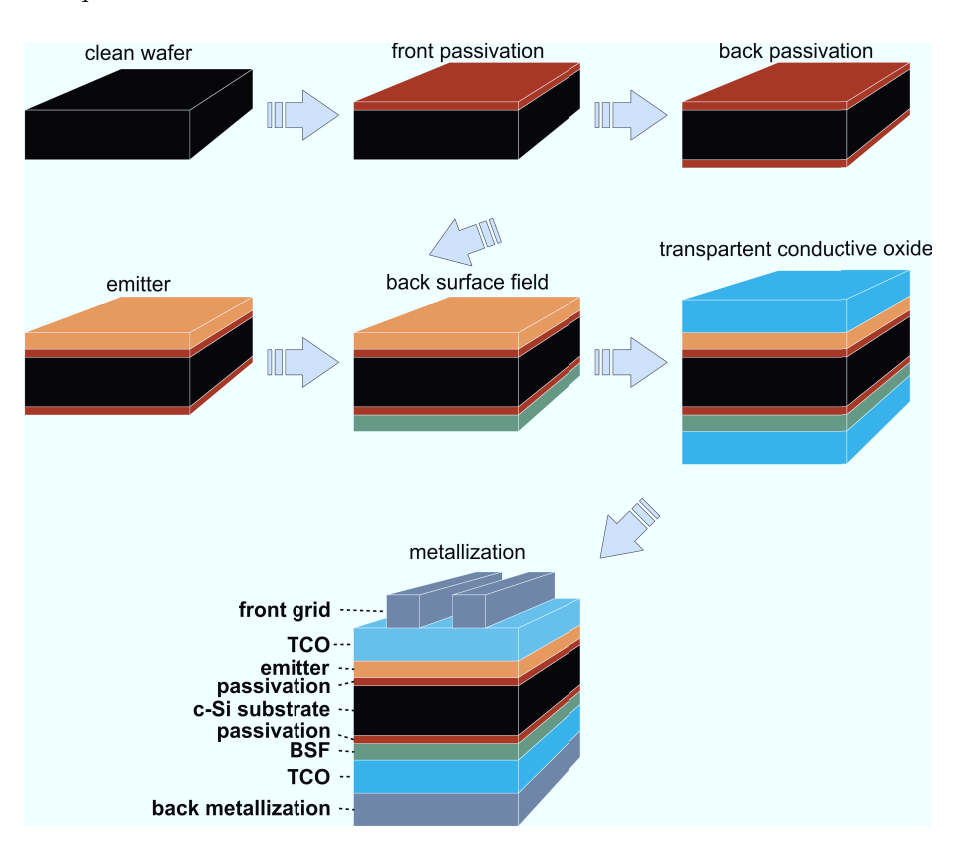


Figure 3.1.: Flow chart of the production of a front-emitter silicon heterojunction (SHJ) solar cell. It includes the following steps: 1) Surface cleaning of the wafer substrate. 2) Plasma enhanced chemical vapor deposition (PECVD) of the front passivation layer. 3) PECVD of the back passivation layer after a hot turn. 4) PECVD of the nc-SiO_x:H emitter layer. 5) Second hot turning and subsequent PECVD of the back surface field (BSF) layer. 6) Sputtering of the indium tin oxide (ITO). 7) Evaporation of the Ag contacts.

was rotated without a cooling step once more to deposit the nc-SiO_x:H layer after another preheating step. After the nc-SiO_x:H layer deposition the wafer was left in vacuum for at least 1h to cool down before being unloaded from the PECVD system. The PECVD was followed by sputtering ITO layers on both sides of the solar cell precursor. Then, an Ag grid was evaporated on the front side of the solar cell, while a full area Ag contact was applied to the back side. In a final

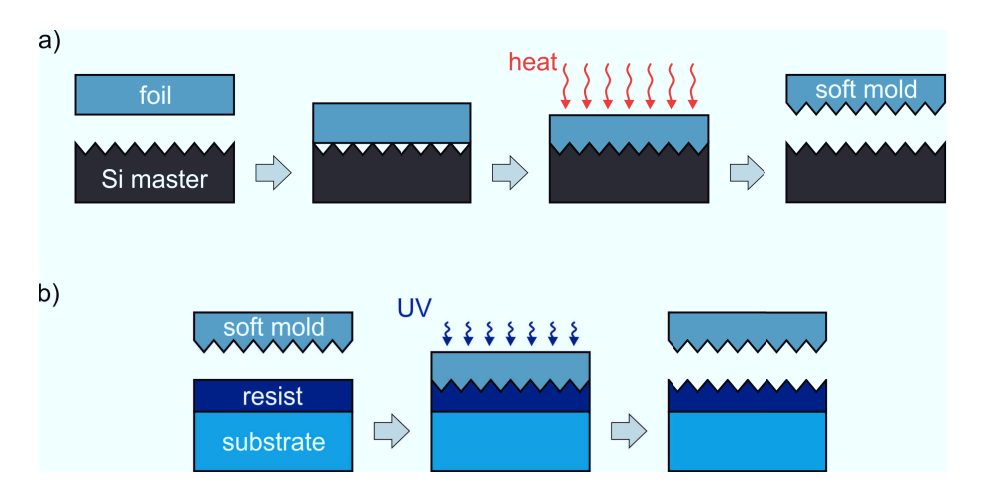


Figure 3.2.: Basic processing steps of nano-imprint lithography (NIL). a) Creating a soft mold from a master structure by hot embossing. b) Transfer of the soft mold texture on the spin coated resist and ultraviolet (UV) radiation hardening of the resist on the substrate.

step, the solar cell was annealed for 2h at 220°C in ambient air to facilitate contact formation.

Nano-imprint lithography (NIL) Nearly arbitrary structures can be replicated at the nanoscale to a silicon dioxide (SiO₂)-like material by using NIL. To achieve this, a soft mold is created from a master structure in a first step as depicted in Fig. 3.2 a). In detail, a polyolefin plastomer foil was pressed onto the master texture, followed by a hot-embossing step at 90°C and 0.4 MPa. Then the soft mold was carefully separated from the master with the surface of the soft mold representing a mirror image of the original master structure. In a second step a UV resist was spin coated onto the substrate at 3000 rpm and the soft mold was pressed into the resist (Fig. 3.2 b)). Next, the resist was hardened by UV radiation, transforming it to a rigid SiO₂-like material with the same surface structure as the master. More details about the process can be found in Ref. [107].

3.2. Material characterization

Thickness The thickness (d) of the material samples was determined using a step profiling system (Vecco DEKTAK 6M Stylus Profiler), which mechanically scans the surface of the sample with a fine probing tip. To create a step profile between the substrate surface and the film surface, three dots were placed at well defined positions on each glass and Si substrate with a permanent marker prior to deposition. After deposition these dots were then removed by careful scratching and dissolving the hydrophobic paint in an isopropyl alcohol (IPA) soaked lab tissue. Knowing d of these films was essential to determine several deposition and material parameters like the deposition rate $(r_{\rm dep})$, the electrical dark conductivity $(\sigma_{\rm D})$, the optical band gap (E_{04}) , or the oxygen content $(c_{\rm O})$.

Conductivity A coplanar measurement setup was employed to determine the lateral electrical dark conductivity (σ_D) of the deposited films. The geometry of the Ag contact layers was described in Sec. 3.1. The measurements were all performed in the dark, at room temperature, and in ambient air. In a first step the samples, deposited on glass substrates, were probed in steps of 10 V in a voltage range between -100 and +100 V. Afterwards, the voltage was set in a way that the resulting current did not exceed the upper limit of the source measurement unit (SMU) (1 mA). Finally, using the thickness of the sample and the geometry of the contacts, the measurement software calculated σ_D of the sample according to Eq. 3.1.

$$\sigma_{\rm D} = \frac{I}{V} \frac{w}{dl}.\tag{3.1}$$

Here, w represents the distance between the Ag contacts and l their length. It is worth noting here that the lateral electrical conductivity (σ) can vary significantly from the transversal σ of the nc-SiO_x:H films due to anisotropic current pathways in its microstructure [108,109]. However, it is not trivial to determine the transversal σ as it can be dominated by the contact resistance between the Ag and the nc-SiO_x:H film. In contrast, for the lateral conductivity the contribution of the contact resistance is negligible due to the large contact area between the Ag and the nc-SiO_x:H (lw) as compared to the cross section (dw) that the current is passing within the

film due to $l \gg d$.

Spectrophotometry Spectrophotometry is used to determine the wavelength (λ) dependent interaction of a sample with photons. In this study a UV-vis-NIR spectrophotometer (Perkin Elmer LAMBDA 950) was used. It enables the fast measurement of the diffuse and total spectral reflectance (R) and transmittance (T) of a sample in a spectral range of 250-3300 nm. The total T and R of the material samples on glass substrates and the solar cells were typically characterized in a spectral range of 300-1500 nm, in which the optical response of the solar cell is important. The front/film side of the samples was always facing the probing light and a shadow mask was used during T measurements to ensure a similar probing spot size as for R measurement. Using d of the films, the absorption coefficient (α) was determined by applying the Hishikawa method [110]

$$e^{\alpha d} \approx \frac{T}{1 - R}.\tag{3.2}$$

This relation eliminated the interference patterns observed in the T and R spectra for most of the samples and allowed to determine E_{04} of the material. Another, more complex, relation for the interference free determination of α was suggested by Ritter and Weiser [111]

$$e^{\alpha d} \approx \frac{(1-R)^2}{2T} + \sqrt{R + \frac{(1-R)^4}{4T^2}}.$$
 (3.3)

A comparison of the α spectra obtained by these methods for a nc-SiO_x:H film is given in Fig. 3.3 a) with a photothermal deflection spectroscopy (PDS) spectrum for reference. Overall, similar spectra are produced by both evaluation methods and they compare well to the PDS spectrum. Nevertheless, for most samples Eq. 3.2 resulted in the α spectra with less interference fringes, as can also be seen in Fig. 3.3 a). In Fig. 3.3 b) E_{04} determined by the method of Hishikawa is generally closer to the results obtained by PDS. Therefore, this method was used for all the nc-SiO_x:H samples investigated in this work, especially as it produced similar results compared to the more time consuming and more sophisticated PDS measurements for the investigated nc-SiO_x:H films.

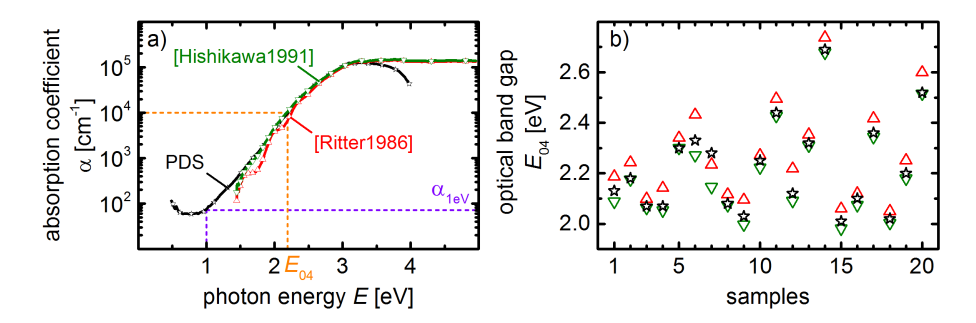


Figure 3.3.: a) Optical absorption spectra of a nc-SiO_x:H sample determined by photothermal deflection spectroscopy (PDS) and with a UV-vis-NIR spectrophotometer. Two different methods were used to determine absorption coefficient (α) from the transmittance (T) and the reflectance (R) spectra according to Eq. 3.2 [110] and Eq. 3.3 [111]. The optical band gap (E₀₄) and the sub-band gap absorption at a photon energy of 1 eV (α _{1eV}) are indicated in the spectra as well. b) E₀₄ values as determined by the three methods for 20 nc-SiO_x:H samples (stars - PDS, upward triangles - Ritter, downward triangles - Hishikawa).

Photothermal deflection spectroscopy (PDS) PDS is a highly sensitive method to determine the absorptance (A) of a given sample over several orders of magnitude. This is realized by submerging the material sample in a deflection medium (typically CCl_4) for which the temperature dependent change in the real part of the refractive index (n) is well known. Then a pump beam of monochromatic light is directed towards the sample and the absorbed light causes heat to be generated within the sample and consecutively to be transferred to the surrounding deflection medium. A probing laser beam $(632\,\mathrm{nm})$ is placed in parallel to the sample surface and gets deflected by the local change in n of the deflection medium due to its change in temperature. This deflection of the probing beam can be related to the light absorbed in the sample and is used to determine α . Furthermore, the pump beam is frequency modulated to make use of the lock-in technology and significantly increase the signal to noise ratio.

In this work, PDS was used for a few selected samples to evaluate the accuracy of determining E_{04} by the faster but less sensitive spectrophotometer measurements. For these samples PDS was also used to determine the sub-band gap absorption at

a photon energy of 1 eV ($\alpha_{1\text{eV}}$) (Fig. 3.3 a)) as an estimate for the amount of active dopants within the nc-SiO_x:H films.

Fourier transform infrared spectroscopy (FTIR) FTIR is a standard technique for the investigation of chemical bonds in compounds. The basic principle is preferential absorption of photons at a specific λ due to the interaction of the photons with electric dipoles. This also implies that only molecular vibrations that cause a change in the dipole moment of the bonded atoms are detectable via FTIR. Several vibrational modes can exist for an identical chemical bond depending on the type of motion that is being performed by the atoms. Additionally, the electronegativity of the bonded atoms, their immediate chemical environments (induction/ligand effects), the bond angle, and the overall surrounding medium affect the energetic state of the bond.

In this work a Nicolet 5700 FTIR spectrometer was used. A reference wafer, taken from the same wafer as the substrate, was used to calibrate the device prior to a measurement. All measurements were performed in a range of 400 to $4000 \,\mathrm{cm}^{-1}$ in $4 \,\mathrm{cm}^{-1}$ steps. To eliminate interference effects, the background of the spectrum was defined manually in a post-processing step by fitting the baseline to the peak free regions of 1400 to $1900 \,\mathrm{cm}^{-1}$ and $2400 \,\mathrm{to} \,4000 \,\mathrm{cm}^{-1}$ and a valley around $600 \,\mathrm{cm}^{-1}$. Next, d of the films was used to calculate α from the measured absorbance spectra [112]. Additionally, a thickness correction factor was applied to α as described in Ref. [113]. In Fig. 3.4 a) and b) the typical bending ((b)) and stretching ((s)) modes present in nc-SiO_x:H films are shown. Starting at low wavenumber (ν) these are:

- 1. Si-H and Si-O (b) modes in the range from 600 to $700\,\mathrm{cm}^{-1}$ [114,115].
- 2. A Si-O (b) mode around $800\,\mathrm{cm^{-1}}$ [114]. It has also been attributed to a coupled mode between Si-H and Si-O-Si in Ref. [116].
- 3. Si-H (b) modes at 840 and 880 cm⁻¹.

 These belong to two and three backbonded O atoms to the Si [114]. However, these modes were also attributed to Si-H₂ groups in Ref. [116].
- 4. An (O_2) Si- H_2 (b) mode around $930 \,\mathrm{cm}^{-1}$ [115].

- 5. A (Si₃)Si-O (s) mode at 970 cm⁻¹ [114]. It also contains a contribution from the (O₂)Si-H₂ (b) peak [115].
- 6. Two peaks in the region from 1000 to 1200 cm⁻¹. Both peaks are related to Si-O-Si (s) modes. The first peak is generally attributed to Si-O (s) vibrations in different chemical environments. Namely, as the chemical environment is turning from a few isolated Si-O bonds towards a SiO₂-like environment, this mode is shifting from 980 to 1080 cm⁻¹ [12, 114]. Additionally, in SiO₂-like environments the second peak can be clearly distinguished around 1150 cm⁻¹. It is attributed to an out of phase vibration of neighboring O, in contrast to the in phase (s) vibration of adjacent O for the first peak [117]. These peaks have also been assigned to O in a terminal position for the lower ν peak and to a bridging position for the peak around 1150 cm⁻¹ [118].
- 7. Two (Si₃)Si-H (s) modes around 2000 and 2100 cm⁻¹.
 These are attributed to Si-H (s) vibrations in dense a-Si:H networks and on inner surfaces, respectively [119].
- 8. An extended Si-H (s) band with three more O related modes. They represent (s) vibrations with an increasing number of O bonded to the Si-H group. These modes were reported at around 2120, 2190, and 2260 cm⁻¹ [114, 115, 120].

The FTIR spectra were also used to determine $c_{\rm O}$ of the individual nc-SiO_x:H films. In Fig. 3.4 c) different methods to determine $c_{\rm O}$ are sketched. Each of these correlates either the peak height or a defined area of the Si-O- (s) peak(s) to $c_{\rm O}$ by using an empirical correlation factor. The oxygen content determined via these methods are displayed in Fig. 3.4 for six nc-SiO_x:H samples deposited at different CO₂ gas flow fractions ($f_{\rm CO_2}$). All the methods produce similar trends for $c_{\rm O}$, while the absolute values differ greatly. For reference, a $c_{\rm O}$ of 67 at.% would imply a perfectly stochiometric film of SiO₂, while 50 at.% would be found in SiO. Overall, $c_{\rm O}$ obtained by the method of Lucovsky et al. [121] correlated well with $c_{\rm O}$ obtained by Rutherford backscattering spectrometry (RBS) for similar nc-SiO_x:H films [89]. Consequently, the method of Lucovsky et al. [121] was used to determine $c_{\rm O}$ in this work while restricting the peak area to 950-1300 cm⁻¹ as indicated in Fig. 3.4 c).

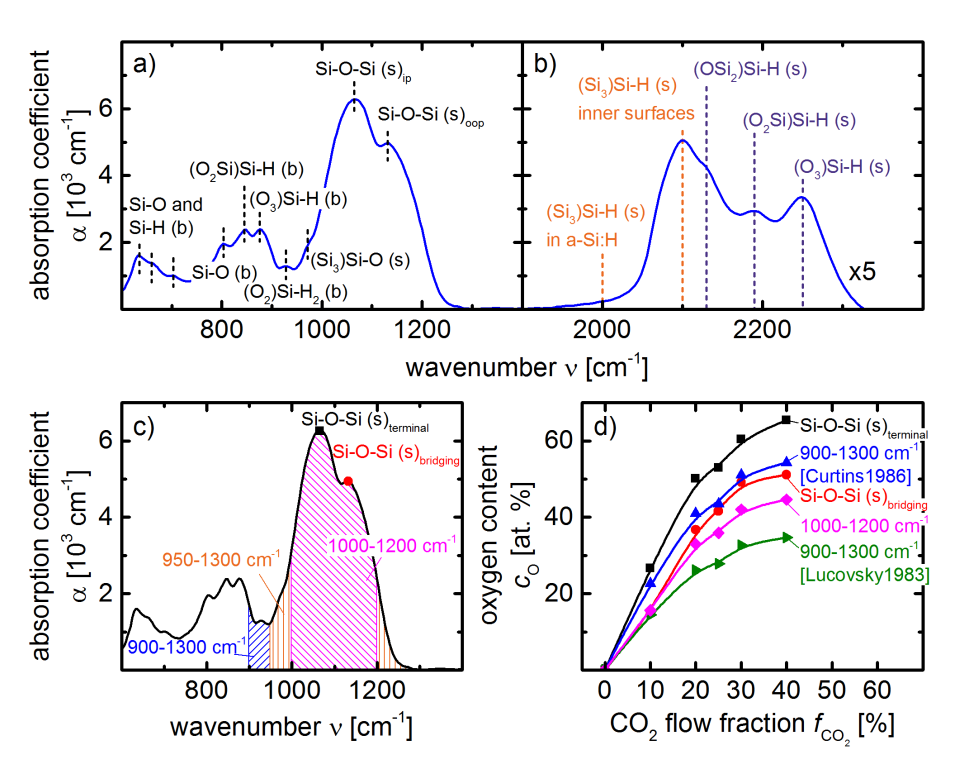


Figure 3.4.: a) Typical Fourier transform infrared spectroscopy (FTIR) spectrum of a nc-SiO_x:H film in the spectral range of 600-1400 cm⁻¹. The most prominent stretching ((s)) and bending ((b)) modes and their positions within the spectrum are indicated. The positions were taken from Refs. [114,115,117-119]. b) FTIR spectrum of the same sample in the Si-H (s) band region of 1900-2200 cm⁻¹. Please note that α has been rescaled in this region to be able to resolve the features in this band. c) The same spectrum as in a) displaying the different regions around the Si-O-Si (s) peak used for determining c_O in a-SiO_x:H and nc-SiO_x:H films by Refs. [118, 121, 122]. d) c_O of several nc-SiO_x:H films deposited at various CO_2 gas flow fractions. c_O was determined by using different regions around the Si-O-Si (s) peak and different proportionality factors. Arranging the methods from top to bottom as indicated in the figure, the first method correlates the Si-O-Si (s) terminal peak height with c_O [118]. The second method evaluates the integral of α from 900 to 1300 cm⁻¹ [118]. The third method relates the height of the Si-O-Si (s) bridging peak to c_O [118]. The fourth method uses the integral of α from 1000 to 1200 cm⁻¹ [122]. Finally, the fifth method is again based on the area from 900 to $1300\,\mathrm{cm}^{-1}$, but is using a different proportionality factor [121].

Raman spectroscopy In Raman spectroscopy the sample is probed with a laser and the injected photons interact with optical phonons within the material. A small part of the photons is scattered inelastically and collected in the spectrometer. Depending on whether the scattered photon has gained or lost energy in the process, the spectral shift is termed a Stokes shift or an Anti-Stokes shift, respectively. A prerequisite for the inelastic scattering of photons is a change of the polarizability of the bond. This makes Raman spectroscopy a complementary technique to FTIR for the investigation of bond states in compounds [123]. For the research of hydrogenated microcrystalline silicon (μc-Si:H) and nc-SiO_x:H films, Raman spectroscopy is commonly used to evaluate the ratio of Si-Si bonds within the a-Si:H or the a-SiO_x:H phase and the nanocrystalline silicon (nc-Si) phase, which can be used as a first approximation of the nc-Si volume fraction [32]. Due to the different Si-Si bond angles and the small differences in bond lengths within the amorphous phases, the transverse optical mode of the Si-Si vibration is shifted from a sharp peak at 520 cm⁻¹ in crystalline Si to a broad peak around 480 cm⁻¹ [124, 125].

A Renishaw in Via Raman Microscope was used to investigate the nc-SiO_x: H films. It was equipped with a 532nm laser, with its power set to 1.2 mW. Raman spectroscopy was used to determine the Raman crystallinity $(I_{\rm c})$ of the nc-SiO_x: H films as described in Ref. [32, 40]. The probing depth of the laser can extend to a few hundred nm. Therefore, care has to be taken when evaluating either very thin or highly transparent films because the glass substrate might contribute to the measured signal and lead to an overestimation of the amorphous peak.

Atom probe tomography (APT) APT is a destructive, sub-nm imaging technique that has been gaining attention due to its expanding applicability and steadily improving accuracy. It is based on the effects of field evaporation and field ionization. In brief, a sharp needle of the investigated material with a tip radius of around 50nm is subjected to a high electric field by a local electrode. This field is set up to be slightly below the field evaporation limit of the atoms within the material. Then, an additional voltage pulse or a laser pulse is added to cause surface atoms to ionize and evaporate from the tip of the needle. By using a time-of-flight spectrometer and a position-sensitive single atom detector, the mass to charge ratio of the evaporated ion can be determined and its initial position within the specimen reconstructed.

However, a considerable fraction of the evaporated ions can not be detected due to intrinsic design limitations of the microchannel plates, typically limiting the detection efficiency to about 60% [126]. Furthermore, some ions may de-ionize before reaching the detector [127]. A more detailed introduction to APT can be found in Ref. [128, 129].

The APT results presented in this study were acquired by Keita Nomoto at the Australian Centre for Microscopy and Microanalysis of the University of Sydney [34]. The measurements were performed using a CAMECA LEAP 4000XSi with a 355 nm laser at a pulse energy of 50 pJ and a pulse rate of 250 kHz. The specimens were prepared by using a Zeiss Auriga focused ion beam scanning electron microscope. During measurements, the chamber pressure was kept below 10⁻⁹Pa and the specimen holder was cooled to about 40 K. The detector efficiency was about 57%.

Scanning electron microscopy (SEM) SEM is a widely established imaging technique using electrons to go beyond the limitations in resolution imposed by λ of visible light. It is often used to visualize the surface topography of textured Si wafers. Briefly, an electron beam is focused on the sample surface and the injected electrons interact with the atoms in the material within an activation volume of several μ m. For topography imaging mostly the secondary electrons are used. They represent electrons that are ejected from atoms within a few nm of the sample surface and due to their low emission depth, they are well suited for topography imaging [130]. The SEM images for this work were recorded on a Hitachi SU800, which also allowed to tilt the investigated sample with respect to the electron beam.

3.3. Solar cell characterization

Photoconductance lifetime testing (PLT) PLT was applied to measure the effective carrier lifetime ($\tau_{\rm eff}$) of solar cell precursors. $\tau_{\rm eff}$ is a combined measure of the surface and the bulk recombination lifetime in a given semiconductor. $\tau_{\rm eff}$ at an excess charge carrier density of $10^{15}\,{\rm cm}^{-3}$ is usually taken as a reference point for comparing different samples. PLT is based on the time dependent decay of the excess charge carrier density in a Si wafer. For this, the cell precursor is illuminated

by a decaying light pulse. The generated excess charge carriers within the sample cause a change in its σ , which is measured by an induction coil. The resistivity (ρ) , the dopant type, and the thickness of the sample are used as input parameters to convert σ to an excess minority charge carrier density. Additionally, the intensity of the light pulse is monitored by a reference cell. This intensity can then be converted to a carrier generation rate. Two modes of operation are distinguished for this setup. First, during a quasi steady-state photo conductance (QSSPC) measurement the light pulse is slowly decaying and σ is measured simultaneously to the decay. In this case the decay rate of the light pulse is long enough, so that the generation and the recombination of charge carriers are balanced within the sample. Then, $\tau_{\rm eff}$ can be calculated from the ratio of the excess charge carrier density to the generation rate at each point during the light pulse decay. This mode is applicable to low $\tau_{\rm eff}$ samples, typically below 200 ms. Second, a transient photo conductance (TPC) measurement is used for high $\tau_{\rm eff}$, commonly beyond 100 ms. Here, the decay rate of σ is recorded in the dark after exposing the sample to a quickly decaying light pulse. $\tau_{\rm eff}$ is then calculated from the ratio of the excess charge carrier density to its (negative) decay rate. Depending on the mode of operation slightly different values for $\tau_{\rm eff}$ can be obtained. Especially for samples with high surface recombination, the transient measurement will result in a shift of $\tau_{\rm eff}$ towards the bulk lifetime as excess charge carriers close to surface recombine quickly and, unlike for the quasi-steady state, are not replenished timely [131].

A Sinton WCT-120 Lifetime Tester was used in this study. Lifetime measurements were typically done on the solar cell precursor after depositing the doped layers and before the TCO depositions. d and ρ of the investigated Si wafers were used as reported by the supplier. These were, $d=280\,\mu\mathrm{m}$ and $\rho=1\text{-}5\Omega\,\mathrm{cm}$ for the polished FZ wafers and $d=170\,\mu\mathrm{m}$ and $\rho\approx3\Omega\,\mathrm{cm}$ for the textured CZ wafers. In addition to $\tau_{\rm eff}$ at an excess charge carrier density of $10^{15}\,\mathrm{cm}^{-3}$, the implied fill factor (iFF) and implied open circuit voltage $(iV_{\rm oc})$ are valuable parameters obtained by PLT. They represent a series resistance $(R_{\rm s})$ free upper limit for the fill factor (FF) and an upper limit of the open circuit voltage $(V_{\rm oc})$ of the solar cell, respectively.

Solar simulator A WACOM-WXS-140S-Super double source class A solar simulator was used to characterize the solar cell performance by current-voltage (I-V) measurements. The measurements were performed under standard test conditions (AM1.5G, 1kW m⁻², 25°C). The solar cell characteristics obtained by the illuminated measurements are the open circuit voltage $(V_{\rm oc})$, fill factor (FF), and the short circuit current density $(J_{\rm sc})$. The solar energy conversion efficiency (η) was calculated by multiplying $V_{\rm oc}$, FF, and $J_{\rm sc}$. To exclude edge effects, the illuminated area of $1x1\,\mathrm{cm}^2$ cells was restricted to $0.9x0.9\,\mathrm{cm}^2$ by applying a shadow mask and the area of $2x2\,\mathrm{cm}^2$ cells to $1.9x1.9\,\mathrm{cm}^2$, if not stated otherwise. Additionally, the solar simulator setup allowed to determine the dark I-V curve of a solar cell and to adjust the cell temperature from 15 to 75°C.

In general, there are four distinct methods to report $J_{\rm sc}$ and thereby also η . First, the active area $J_{\rm sc}$, for which only the illuminated and current generating parts of a solar cell are considered to calculate $J_{\rm sc}$ from the measured current. The contacting grid and the surroundings of the cell are excluded. Second, the designated area $J_{\rm sc}$, which includes some parts of the grid, but has a significant amount of non-illuminated area, especially the contacting components. Third, the aperture area $J_{\rm sc}$, which includes all of the essential parts of the solar cell, including the busbars, fingers, and interconnects. And Forth, the total area $J_{\rm sc}$, for which the total cell area including the surrounding substrate is illuminated and considered [132]. All of the efficiencies and currents reported in this study are active area based, as long as not stated otherwise.

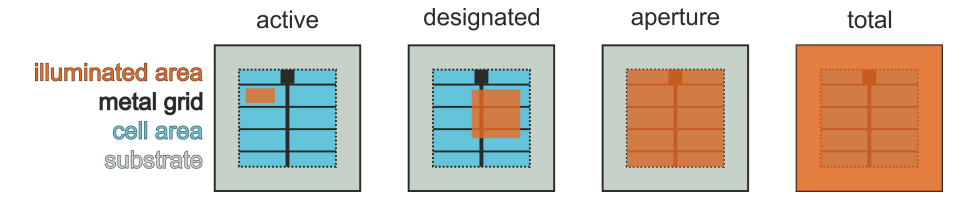


Figure 3.5.: Area classifications for reporting the short circuit current density (J_{sc}) and the solar energy conversion efficiency (η) of a solar cell, following Green et al. [132]. From left to right these are: active area (act), designated area (da), aperture area (ap), and total area (ta).

Suns-Voc measurements A Suns-Voc measurement with a Sinton Suns-Voc stage is useful to estimate the effect of $R_{\rm s}$ on the I-V curve. It is based on the principle of determining $V_{\rm oc}$ and $J_{\rm sc}$ of a solar cell at different illumination intensities. In detail, the solar cell is contacted by a copper plate on the back and a contacting needle on the front. Then a short light pulse is illuminating the solar cell. Meanwhile, $V_{\rm oc}$ of the probed solar cell is being measured. At the same time, a reference cell, which is located next to the measured solar cell, records the intensity of the decaying light pulse. The voltage of this reference cell is used to estimate $J_{\rm sc}$ of the probed cell by supplying the real $J_{\rm sc}$ at 1 sun to the measurement software. By combining these $J_{\rm sc}$ - $V_{\rm oc}$ pairs, an $R_{\rm s}$ free I-V curve can be obtained. Comparing this curve to the J-V curve from the solar simulator reveals the effect of $R_{\rm s}$ on the solar cell performance. Furthermore, the pseudo fill factor (pFF) can be obtained from the Suns-Voc measurement, which represents an upper limit for FF of a $R_{\rm s}$ free solar cell.

Differential spectral response (DSR) The DSR measurement is a key tool to evaluate the optical and (to some degree) the electrical response of a solar cell. It provides access to the spectrally resolved external quantum efficiency (EQE), which is defined as the ratio of collected electron/hole pairs to the photons impinging on the sample surface. By combining the EQE and R of the solar cell, the internal quantum efficiency (IQE) was calculated. It is defined as $IQE = EQE(1-R)^{-1}$ and represents the ratio of the collected electron/hole pairs to the absorbed photons. Therefore, it eliminates the reflection losses, which are included in EQE spectra. A particular feature of the employed DSR setup is the ability to investigate the angular dependence of the EQE by rotating the sample stage. Furthermore, an additional W lamp was available as a white bias light source up to a lamp power of 250 W (approx. 0.1 sun). All DSR measurements were performed in a λ range of $\lambda = 320\text{-}1150\,\mathrm{nm}$ in steps of $10 \,\mathrm{nm}$. The measured EQE spectra were convoluted with the AM1.5G spectrum to calculate the integrated short circuit current density from the EQE spectrum $(J_{\text{sc,DSR}})$. Three different areas of illumination were used during the DSR measurements by varying the probing spot size. Most of the measurements were performed with an optical lens installed immediately in front of the sample. By using this lens the illuminated area was reduced to about 2 mm², which is sufficiently small

to fit between the Ag grid fingers. Thereby, the active area EQE of the solar cells could be determined. For a designated cell without front metallization, a circular spot of about 7 mm in diameter could be used by removing the focusing lens. The same cell was used to determine R representatively for all the solar cells on the wafer. Furthermore, the spot size could be enlarged to about 50 mm in diameter, allowing to investigate the aperture area EQE by applying a shadow mask similarly to the I-V measurements.

OPAL 2 This freeware program for the optical analysis of the front surface of a solar cell (OPAL 2) provides means to simulate the parasitic absorptance (A_{paras}) of arbitrary front layer stacks and their effect on R of a solar cell. The main advantage of this software is a rapid simulation due to a statistical approach to simulate the interaction of light rays with a given surface texture. In fact, there are only a limited number of paths that an incident ray of light will take when intersecting a given surface plane. As a first step these unique ray paths are determined via simplified classical ray tracing of 10⁵ rays for a given angle of light incidence and a given surface texture. Then, R, A, and T are determined by solving the Fresnel equations for each of these ray paths and they are combined according to their statistical probability to obtain the total R, A, and T [133, 134]. A limitation of the software is the simulation of light-trapping within the solar cells, as only the front side is simulated. So, after passing the front layer stack the light is considered transmitted and any further interactions within the substrate or at the back side of the solar cell are not included. Accordingly, the simulation results were only considered valid up to $\lambda \approx 900\,\mathrm{nm}$, where almost all light passing the front layer stack is absorbed within the Si wafer of $d \ge 170 \,\mu\text{m}$, as they were applied in this study.

Nevertheless, the simulations in this study were performed in a λ range of 300-1150 nm, in steps of 10 nm, to be able to resolve trends in $A_{\rm paras}$ in the long λ range by changes in the front layer stack. For the initial ray tracing 10^5 rays were used and the number of bounces was capped at 10. The unpolarized light was approximated by combining light of seven different polarization angles. The angle of incidence was set to 8°. The Si random pyramid texture was defined according to the ideal case with a characteristic angle of 54.7° and no planar areas [134]. Moreover, the spectrally resolved n and imaginary part of the refractive index (k) of

the $\operatorname{nc-SiO}_x$:H layers and their respective thicknesses were essential input parameters for the simulations. The values for n and k were acquired by fitting the measured R and T spectra in a software for the simulation and analysis of optical spectra (SCOUT) by "W. Theiss Hard- and Software".

The development of hydrogenated nanocrystalline silicon oxide (nc-SiO_x:H) deposited via plasma enhanced chemical vapor deposition (PECVD) at very high frequency (VHF) is described in detail in the following chapter. The goal of this development is an improvement of the optoelectronic properties of nc-SiO_x:H films due to an enhanced selective etching and therefore increased crystallinity of higher frequency depositions as compared to the more commonly used radio frequency (RF) depositions [135, 136]. The first section covers the influence of the deposition power (P), the deposition pressure (p), the B(CH₃)₃ gas flow fraction ($f_{\text{B(CH}_3)_3}$), and the CO₂ gas flow fraction (f_{CO_2}) on the properties of p-type doped (<p>) nc-SiO_x:H films. In the second section a classification of nc-SiO_x:H films according to their structural and optoelectronic properties is introduced and exemplified by discussing the variation of the gas flows fractions for n-type doped (<n>) nc-SiO_x:H films. Lastly, the third section encompasses an overview of the deposited nc-SiO_x:H films and compares them to literature data as well as previously obtained results using RF depositions at the same deposition system.

4.1. Development of $\langle p \rangle$ nc-SiO_x:H at very high frequency

The starting point for the development of the $nc-SiO_x$:H films in this study was the work of Ding et al. [49, 89]. It provided the electrode spacing (d_{el}) , the substrate temperature (T_{sub}) , and the initial p, P, and gas flow fractions (see also Sec. 3.1). All $nc-SiO_x$:H films described in the following were deposited in the deposition system introduced in Sec. 3.1. The depositions were performed at very high

frequency (VHF), denoting a specific deposition frequency of $81.4 \,\mathrm{MHz}$ in this work. The development in this section will be focused on the <p> > nc-SiO $_x$:H films as the expected effect of the VHF depositions is an enhancement of the crystallinity, which has previously been reported for hydrogenated microcrystalline silicon (μ c-Si:H) thin films [135]. In contrast to <n> nc-SiO $_x$:H, a high crystallinity is difficult to achieve in <p> nc-SiO $_x$:H due to the crystallinity inhibiting effect of trimethylborane (B(CH $_3$) $_3$) [137,138].

To be beneficial in silicon heterojunction (SHJ) solar cells, certain requirements need to be fulfilled by the nc-SiO_x:H films. On the one hand, a sufficient electrical conductivity (σ) is required to ensure a low series resistance (R_s) and an ohmic contact towards the transparent conductive oxide (TCO) and, thereby, a high fill factor (FF) for the device. On the other hand, the films need to be as transparent as possible to provide a low parasitic absorption of light. Furthermore, the deposition conditions have to be compatible to the passivation layer deposition and not affect its passivation properties. A high homogeneity and a constant deposition rate over the substrate area and throughout the deposition are favorable as well.

4.1.1. Effect of deposition power and deposition pressure

As a first step in the development of $\operatorname{nc-SiO}_x$:H at VHF, the influence of varying P and p on the properties of $\operatorname{nc-SiO}_x$:H were investigated. The p-type doped material was chosen as a starting point because achieving a high crystallinity in $\operatorname{nc-SiO}_x$:H is especially challenging due to the nanocrystalline silicon (nc-Si) inhibiting effect of B(CH₃)₃ [137–139]. The results of the P and p variation are summarized in Fig. 4.1.

The deposition power was varied in a range from 20 to 80 W at deposition pressures of 50, 200, and 400 Pa. Starting at the highest p, the Raman crystallinity (I_c) and c_O were increasing towards higher P (Fig. 4.1 a) and c)). The increase in c_O with increasing P is due to an enhanced dissociation of carbon dioxide (CO₂) [140,141]. An increase of I_c with P has also been reported in [33,136] and attributed to an increased amount of atomic H promoting the growth of the crystalline phase. The electrical dark conductivity (σ_D) and the optical band gap (E_{04}) of the films

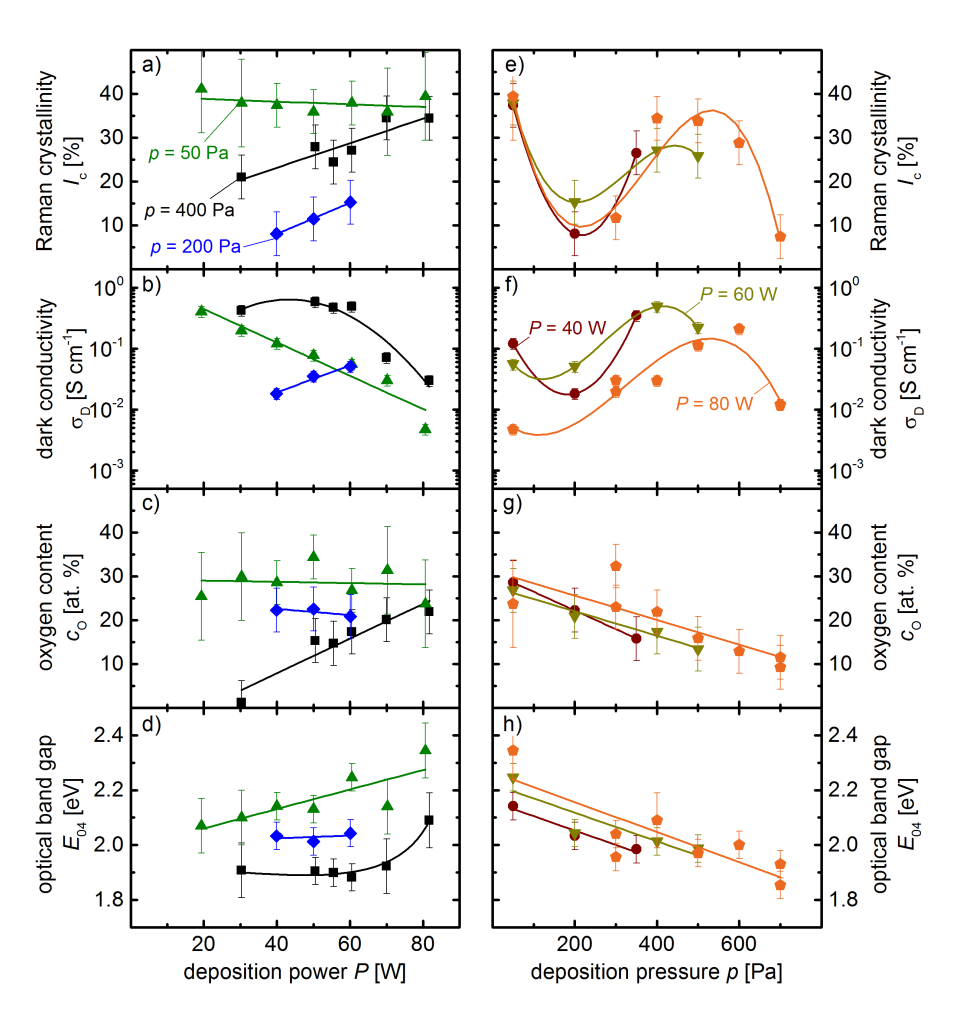


Figure 4.1.: a)-d) Effect of the deposition power on a) the Raman crystallinity (I_c) , b) the electrical dark conductivity (σ_D) , c) the oxygen content (c_O) , and d) the optical band gap (E_{04}) of p-type doped () nc-SiO_x:H films deposited at different deposition pressures (p) using very high frequency (VHF). e)-h) Variation of the deposition pressure from 50 to 700 Pa and its effect on e) I_c , f) σ_D , g) c_O , and h) E_{04} . The $B(CH_3)_3$ gas flow fraction $(f_{B(CH_3)_3})$, H_2 gas flow fraction (f_{H_2}) , and CO_2 gas flow fraction (f_{CO_2}) for all depositions were kept constant at 1.9%, 99.6%, and 20%, respectively. The added lines serve as a quide to the eye.

were hardly affected by these changes up to $P=60\,\mathrm{W}$ (Fig. 4.1 b) and d)). Only from a c_O of about 20 at.% a marked increase in E_04 and a decrease in σ_D was observed. Apparently, c_O within the hydrogenated amorphous silicon oxide (a-SiO_x:H) matrix phase was sufficiently low not to affect the conductivity through the nc-Si phase up to this point. However, as the amount of nc-Si increased, c_O within the matrix phase increased steadily as well for a constant c_O . This O-enrichment of the a-SiO_x:H matrix was further enhanced by an overall increasing c_O .

Gabriel et al. [33] proposed two distinct deposition regimes for the deposition of <n> nc-SiO_x:H for varying p and P. The first deposition region (A) is characterized by a dependence of all properties on p as well as P and it was observed at a high ratio of P/p, so either low p or high P. In their publication the ratio of P to p was taken as a measure of the energy available per plasma particle during deposition and could also be related to the availability of atomic H during the deposition [33]. In region A a decrease in the real part of the refractive index (n), corresponding to an increasing $c_{\rm O}$, was accompanied by a decrease in $I_{\rm c}$ with a low dependence of the deposition rate $(r_{\rm dep})$ on P. The second deposition region (B) was characterized by a stronger dependence of $r_{\rm dep}$ and n on P, while the dependence on p was weaker as compared to region A. This region was found at at a low ratio of P/p. The transition between the two regions was reported to lie at a P/p ratio of about $0.3 \, {\rm WPa}^{-1}$ and displayed a weak dependence of $I_{\rm c}$ on P as well as p [33].

For the presented results, the depositions at $p=400\,\mathrm{Pa}$ can be assigned to the deposition region B (low amount of atomic H) due to a strong dependence of $I_{\rm c}$ and $c_{\rm O}$ on P and the simultaneous increase of $I_{\rm c}$ and $c_{\rm O}$. Furthermore, $r_{\rm dep}$ strongly increased from about 3 to $8\,\mathrm{nm\,min^{-1}}$ with increasing P, confirming the observations in [33] for the region B. At a lower p of 200 Pa, $c_{\rm O}$ and $E_{\rm 04}$ of the nc-SiO_x:H films were not affected by a change in P. Only a small increase in $\sigma_{\rm D}$ due to an enhanced $I_{\rm c}$ was evident. In comparison to the depositions at $p=400\,\mathrm{Pa}$, the lower p led to an increase of the P/p ratio and therefore a higher amount of atomic H in the plasma, which characterizes the transition to the deposition region A [33]. Finally, the material properties were notably different at $p=50\,\mathrm{Pa}$. Here, P had hardly any influence on $c_{\rm O}$ or $I_{\rm c}$. Moreover, no change was evident in the microstructure of the nc-SiO_x:H films judging from the Fourier transform infrared spectroscopy (FTIR)

or the Raman spectra (not shown). Nevertheless, $\sigma_{\rm D}$ decreased towards higher P, while E_{04} increased. Due to the low p, these material presumably had the highest amount of atomic H in the plasma during the deposition [33]. At 50 Pa the high P/p ratio may lead to enhanced H etching, which would lead to a decrease in the crystallite size [24]. In [24] it was also reported that at lower p the crystallite density slightly decreased as determined by energy filtered transmission electron microscopy (EFTEM), even though no change in I_c was evident from the Raman spectra. Therefore, the enhanced E_{04} could be a consequence of a reduced volume fraction of nc-Si or enhanced quantum confinement due to the smaller crystallite size [18,38]. Another possible explanation for the decline in $\sigma_{\rm D}$ and increasing E_{04} is a reduced amount of the hydrogenated amorphous silicon (a-Si:H) phase [22,142] at the interface between the nc-Si and the a-SiO_x:H due to the high energy of incident particles and their enhanced capability to break the weak Si-Si bonds in a-Si:H. This reduction in a-Si:H would lead to an increase in the defect density at the nc-Si/a-SiO_x:H interface, reducing σ , and an increase in E_{04} due to the substitution of a-Si:H by a-SiO_x:H or nc-Si.

Increasing the deposition pressure at a constant deposition power led to a continuous decrease in O-incorporation in the nc-SiO_x:H films (Fig. 4.1 g)), independently of the applied P. E_{04} decreased accordingly (Fig. 4.1 h)). This can be attributed to a lower availability of O precursors during film growth at higher p due to an increased number of gas phase collisions [24, 140]. A minimum in I_c (Fig. 4.1 e)) was observed around 200-300 Pa, which correlated with a minimum in $\sigma_{\rm D}$. In the FTIR spectra the Si-O-Si stretching ((s)) mode significantly decreased at $1130\,\mathrm{cm}^{-1}$ by changing p from $50\,\mathrm{Pa}$ to $200\,\mathrm{Pa}$ and the overall peak maximum shifted from $1090\,\mathrm{cm^{-1}}$ to $1060\,\mathrm{cm^{-1}}$ (not shown). This indicates less of silicon dioxide (SiO₂)-like bonding environments in accordance with the overall decreasing $c_{\rm O}$ Additionally, the Si-H (s) peak at $2000\,\mathrm{cm}^{-1}$ increased for the low $I_{\rm c}$ samples when p was increased to 200 Pa, indicating a rise in the amount of a-Si:H phase. In total, this points at a decrease of SiO_2 in favor of a-Si:H for films with a low I_c . Increasing p beyond 300 Pa resulted in an increase in I_c and σ_D . Here, the low incorporation of O resulted in an enhanced I_c up to a p of 600 Pa. Beyond 600 Pa. I_c decreased again. This was also reported by Kondo et al. [136] for µc-Si:H films and explained by an increase of the annihilation reaction between H and silane (SiH₄), leading to

a decrease of the atomic H flux to the substrate surface and, thereby, impeding the crystalline growth, which is facilitated by atomic H at low temperatures. Another suggestion was that a decrease of the electron temperature with increasing p leads to less dissociation of H₂ [140] and, therefore, less atomic H at the film surface.

Overall, the deposition power and deposition pressure variation indicated two different deposition regimes for the nc-SiO_x:H films, similarly to the reports in [33]. First, a high p and low P regime with a low $c_{\rm O}$ and a high $I_{\rm c}$ in the films. This regime can be related to a low amount of atomic H in the plasma during the deposition. Second, a high $I_{\rm c}$ region at low p with a more SiO₂-like matrix and similar $I_{\rm c}$ independently of the applied P. This region is associated with an increased amount of atomic H for nc-SiO_x:H depositions at RF [33]. For the VHF nc-SiO_x:H films, the density of atomic H is enhanced even further [135, 136] and additionally they benefit from a reduced ion energy [135, 143, 144]. Therefore, the best optoelectronic trade-off was achieved for <p> nc-SiO_x:H films deposited in this regime (p = 50Pa). As P could be used to tune the trade-off between E_{04} and $\sigma_{\rm D}$ in this deposition regime, depositions at P = 30 W and at P = 70 W were considered for the following gas flow optimization.

4.1.2. Optimization of the gas flows

In the next step of <p> <nc-SiO_x:H optimization at VHF, the gas flows were adjusted with respect to each other. Only the H₂ gas flow was kept constant at its maximum value of 500 sccm. With the gas flows represented by their molecular formula framed by square brackets ([]), the gas flow fractions were defined as:

$$f_{\text{CO}_2} = \frac{[\text{CO}_2]}{[\text{SiH}_4] + [\text{CO}_2]} 100 \%,$$
 (4.1)

$$f_{\rm H_2} = \frac{[{\rm H_2}]}{[{\rm SiH_4}] + [{\rm H_2}]} \, 100 \,\%,$$
 (4.2)

$$f_{\rm PH_3} = \frac{[{\rm PH_3}]}{[{\rm SiH_4}] + [{\rm PH_3}]} \, 100\%,$$
 (4.3)

4.1. Development of $\langle p \rangle$ nc-SiO_x:H at very high frequency

$$f_{\text{B(CH}_3)_3} = \frac{[\text{B(CH}_3)_3]}{[\text{SiH}_4] + [\text{B(CH}_3)_3]} 100\%.$$
 (4.4)

The results of varying the $B(CH_3)_3$ gas flow fraction $(f_{B(CH_2)_2})$ for the deposition regime, discussed in the previous paragraph, are summarized in Fig. 4.2. The nc-SiO_x:H films with $f_{B(CH_2)_2} = 2\%$ were used as a starting point. By adding more $B(CH_3)_3$ to the gas mixture I_c of the nc-SiO_x:H films strongly decreased up to the amorphous state for $f_{\rm B(CH_2)_2} = 7\%$ (Fig. 4.2 a)). This amorphization of nc-Si by B has already been reported by several authors [46, 137, 138] and presents an important factor in the development of highly conductive $\langle p \rangle$ nc-SiO_x:H films. The increased incorporation of B was accompanied by a small B-O (s) band appearing in the FTIR spectra (Fig. 4.3) around 1350 cm⁻¹ and an increase of the Si-H (s) peak at 2000 cm⁻¹, in accordance with [137]. Additionally, a small peak at 1270 cm⁻¹ was evident that can be attributed to the Si-CH₃ (s) mode, which was accompanied by Si-H (s) modes at 2330 and 2360 cm⁻¹ [145]. This indicates a small amount of C being incorporated as methyl groups in the nc-SiO_x:H films as a consequence of using trimethylborane as the B-source. This incorporation of C reduces the crystallinity in addition to B [139]. The fully amorphous state was reached at a higher $f_{\rm B(CH_0)_0}$ for the higher P depositions and can be related to the crystallinity enhancing effect of depositions with an increased P. $\sigma_{\rm D}$ followed the trend of $I_{\rm c}$ and a drop of $\sigma_{\rm D}$ by five orders of magnitude was distinguishing the nc-SiO_x:H from the a-SiO_x:H films. At lower $f_{B(CH_2)_2}$, however, B-doping led to an enhancement of σ_D , even though I_c was decreasing. Here, σ_D was dominated by an increasing amount of free charge carriers due to more active B-dopants being incorporated in the nc-Si phase. Overall, a slightly higher σ_D could be reached for the depositions at P = 30 W.

Surprisingly, $c_{\rm O}$ also steadily decreased for an increasing $f_{\rm B(CH_3)_3}$ (Fig. 4.2 b)). The decrease in $c_{\rm O}$ mainly affected O-rich environments as evident from the strong decrease of the (O₃)Si-H (s) mode at 2260 cm⁻¹ (Fig. 4.3 b)). It might be related to an increased amount of the incorporated oxygen being bonded to B or C from the B(CH₃)₃ instead of Si. In fact, $c_{\rm O}$ determined here is solely based on the Si-O (s) band. So, the actual oxygen content within the films is expected to be higher with some of the O being bonded to B or C. Nevertheless, E_{04} decreased nearly linearly for higher $f_{\rm B(CH_3)_3}$, matching the reduction in $c_{\rm O}$. The overall $c_{\rm O}$ and E_{04} were slightly higher for the depositions at 70W due to the enhanced dissociation of

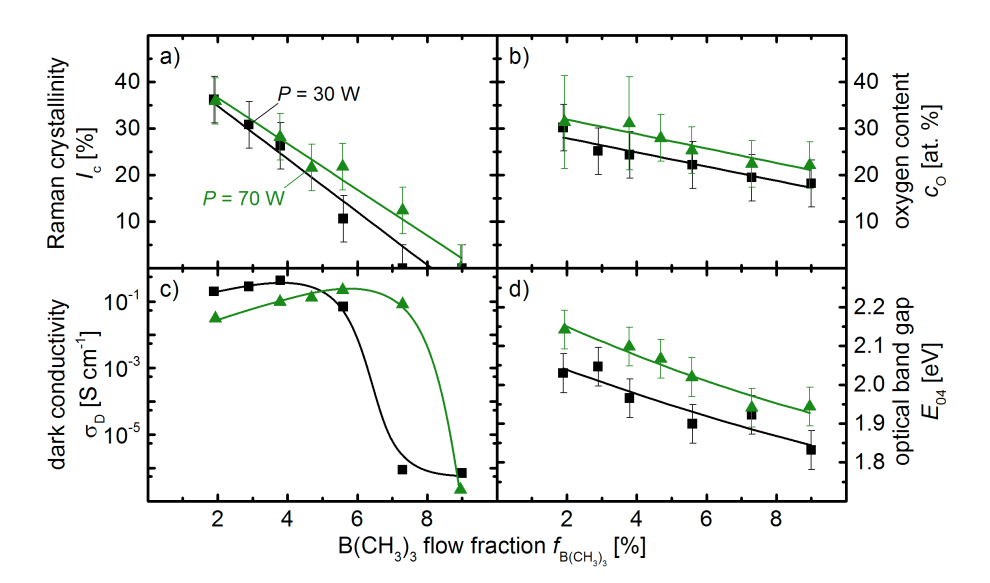


Figure 4.2.: Effect of changing the $B(CH_3)_3$ gas flow fraction $(f_{B(CH_3)_3})$ on the structural (a), b)) and optoelectronic (c), d)) properties of $nc-SiO_x:H$ films deposited at $50\,\mathrm{Pa}$ for a deposition power (P) of $30\,\mathrm{W}$ and $70\,\mathrm{W}$. The CO_2 gas flow fraction (f_{CO_2}) was kept constant at 20% for all depositions. Lines were added as a guide to the eye.

CO₂ as discussed in Sec. 4.1.1. In total, the nc-SiO_x:H films deposited at $P = 30 \,\mathrm{W}$ with $f_{\mathrm{B(CH_3)_3}} = 3.8 \,\%$ and at $P = 70 \,\mathrm{W}$ with $f_{\mathrm{B(CH_3)_3}} = 5.6 \,\%$ exhibited the highest σ_{D} and were taken as a basis for the variation of $f_{\mathrm{CO_2}}$.

The effect of various $f_{\rm CO_2}$ on the properties of nc-SiO_x:H films is summarized in Fig. 4.4. The main objective of the $f_{\rm CO_2}$ variation is to control $c_{\rm O}$ within the films by adjusting the amount of CO₂ available as an O-precursor. An almost linear dependence of $c_{\rm O}$ on $f_{\rm CO_2}$ was observed for the deposited nc-SiO_x:H films (Fig. 4.4 b)) in accordance with reports from literature [17, 85, 89]. Furthermore, both investigated deposition regimes showed a similar $c_{\rm O}$ dependence. The same was observed for $E_{\rm O4}$ and it correlated well with the change in $c_{\rm O}$. This indicates that the O incorporation was occurring in a similar way for both deposition regimes. Indeed, a decrease of a-Si:H related and an increase of SiO₂ related peaks was observed in the FTIR spectra for the films from both deposition regimes (not shown).

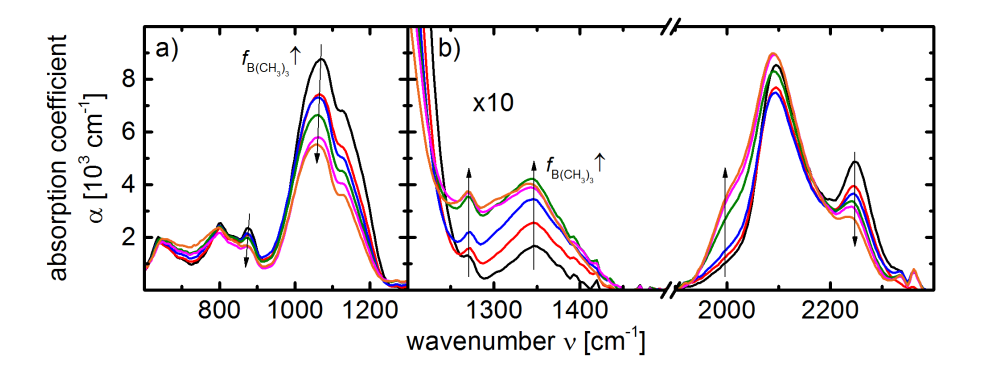


Figure 4.3.: FTIR spectra of $\langle p \rangle$ nc-SiO_x:H films deposited at 30W and varying $B(CH_3)_3$ gas flow fraction $(f_{B(CH_3)_3})$ (see also Fig. 4.2). The arrows indicate changes in the spectra due to an increasing $f_{B(CH_3)_3}$. a) FTIR spectra in the range of 600 to $1300\,\mathrm{cm}^{-1}$. b) The same spectra in the range from 1200 to $1500\,\mathrm{cm}^{-1}$ and 1900 to $2400\,\mathrm{cm}^{-1}$. There were no peaks detected in the intermediate range. Please note that α has been rescaled in b) to show the lower intensity modes.

 $I_{\rm c}$ strongly dropped from 60-70% to 20-30% when just a small amount of CO₂ was added to the gas mixture (Fig. 4.4 a)). This is due to the incorporation of O and thereby addition of a-SiO_x:H to the films, which replaced the a-Si:H and nc-Si phases. For higher $f_{\rm CO_2}$ the decrease was less pronounced, but still significant. In contrast to the $f_{\rm B(CH_3)_3}$ variation, a higher $I_{\rm c}$ was achieved for all $f_{\rm CO_2}$ for the depositions at $P=30\,{\rm W}$. This was due to the combination with a lower $f_{\rm B(CH_3)_3}$ of 3.8%, which led to a higher crystallinity. $\sigma_{\rm D}$ of the films was affected by the decrease in $I_{\rm c}$ beyond $f_{\rm CO_2}=20\,{\rm \%}$, which also marked the transition towards $c_{\rm O}\geq 25\,{\rm at.\%}$ and $I_{\rm c}\leq 20\,{\rm at.\%}$.

Overall, the increase in E_{04} and decrease of $\sigma_{\rm D}$ was a consequence of the gradual substitution of nc-Si by a-SiO_x:H with increasing $f_{\rm CO_2}$. As a main result from this optimization of nc-SiO_x:H, the VHF deposition regime at $p=50\,{\rm Pa}$, $P=30\,{\rm W}$, and $f_{\rm B(CH_3)_3}=3.8\%$ was identified to be well suited to produce material with improved optoelectronic properties and a tunable $\sigma_{\rm D}$ and E_{04} by $f_{\rm CO_2}$ variation.

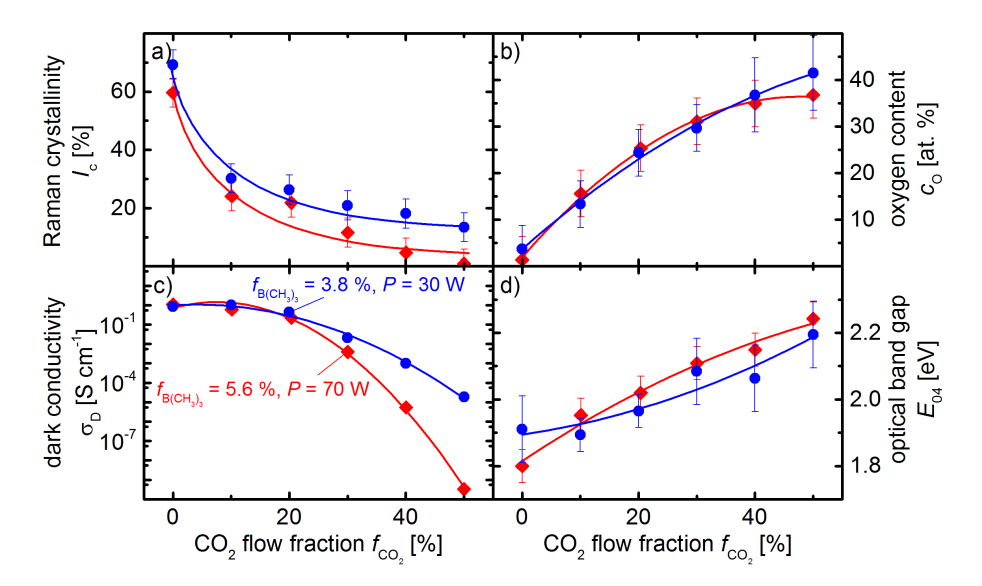


Figure 4.4.: a) Raman crystallinity (I_c) , b) oxygen content (c_O) , c) electrical dark conductivity (σ_D) , and d) optical band gap (E_{04}) of nc-SiO_x:H films deposited at various CO_2 gas flow fractions (f_{CO_2}) . Two deposition regimes were investigated, one at a $B(CH_3)_3$ gas flow fraction $(f_{B(CH_3)_3})$ of 5.6% and a deposition power (P) of 70 W and the other at a $f_{B(CH_3)_3}$ of 3.8% and a P of 30 W. All depositions were performed at a deposition pressure (p) of 50 Pa. The lines are a guide to the eye.

4.2. Classification of nc-SiO_x:H films

As might already be evident from the results discussed in the previous section, similar optoelectronic properties for nc-SiO_x:H can be achieved for different deposition regimes (see also Sec. 4.3). Therefore, a microstructure model was developed in this work to classify various nc-SiO_x:H films according to their optoelectronic and their structural properties. It is meant to provide guidelines for the development of nc-SiO_x:H films by identifying the microstructure of the film and to aid in developing steps for further optimization. This model will be introduced in the following on the basis of the results obtained on two series of nc-SiO_x:H samples and then its applicability will be demonstrated for a $f_{\rm CO_2}$ and two PH₃ gas flow fraction ($f_{\rm PH_3}$) series.

4.2.1. The deposition regions

The model for the microstructure is based on four different classes of nc-SiO_x:H films. These classes or regions of nc-SiO_x:H deposition are, sorted as region I-IV: the "fully amorphous region", the "onset of nc-Si formation", the "O and nc-Si enrichment", and the "nc-Si deterioration region". In Fig. 4.5 a complete introduction to all four classes is given by considering $f_{\rm H_2}$ variations for <n> nc-SiO_x:H filmsin a wide range. The schematic microstructure of a-SiO_x:H films (Fig. 4.5 i)) was initially proposed by Haga and Watanabe [142] and by Hohl et al. [146]. They described the films as consisting of a-Si:H and an O-rich a-SiO_x:H with a thin intermediate O-deficient a-SiO_x:H region in between, which is a consequence of the gradual interface between the O-free and the O-rich regions. This intermediate region was omitted for clarity in the sketches shown here, though it was evident from the FTIR spectra. The thermodynamically favored phase separation to a-Si:H and a-SiO_x:H is facilitated by the high amount of H present during the low temperature PECVD depositions [18]. H mediates the relaxation of strained bonds and increases the diffusion length of film precursors by surface heating and H coverage of the film surface [18, 147]. Another approach to achieve this phase separation is post-deposition annealing of homogeneous a-SiO_x:H films [27, 34].

Region I Figure 4.5 a)-d) show the changes in the film properties for varying $f_{\rm H_2}$. Starting at low $f_{\rm H_2}$, the first region was denoted as the "fully amorphous region", which includes a-Si:H films as well. The films were characterized by having no detectable nc-Si in them, as evident by $I_{\rm c}=0$. The E_{04} and $\sigma_{\rm D}$ showed typical values for doped a-SiO_x:H films with $0 \le x \le 2$ [148]. In region I the atomic H density was insufficient to facilitate nc-Si formation [136] or affect the O-incorporation [140]. $f_{\rm CO_2}=40\,\%$ resulted in a higher E_{04} and a lower $\sigma_{\rm D}$ as compared to films deposited at $f_{\rm CO_2}=20\,\%$. This can be explained by a change in the ratio of a-Si:H to a-SiO_x:H. Two typical FTIR spectra of those films are shown in Fig. 4.5 e) and a sketch of the microstructure is provided in Fig. 4.5 i). The FTIR spectra clearly showed an a-Si:H related Si-H (s) peak around $2000\,{\rm cm}^{-1}$ and also exhibited several Si-H (s) peaks for bonding environments related to a-SiO_x:H. The a-Si:H related peak decreased for the films grown at $f_{\rm CO_2}=40\,\%$, while the peak around $2250\,{\rm cm}^{-1}$

strongly increased, indicating more oxygen rich a-SiO_x:H. Contrary to the depositions of <p> nc-SiO_x:H, no C-related peaks were observed in the FTIR spectra of <n> nc-SiO_x:H, even though CO₂ was used as the O-source. Indeed, the incorporation of O from CO₂ is unlikely due to the high dissociation energy of the CO molecule [140]. For the <p> nc-SiO_x:H films, however, the methyl groups of the trimethylborane (B(CH₃)₃) served as a major source of C.

Region II For a $f_{\rm H_2}$ beyond about 98.2%, the films belong to the "onset of nc-Si formation" region, which also includes μ c-Si:H films for depositions without CO₂. Here, some nc-Si was incorporated into the films and $I_{\rm c}$ increased. The amount of nc-Si is controlled by the availability of atomic H [18,147]. Therefore, $I_{\rm c}$ increased towards higher $f_{\rm H_2}$ [136]. $\sigma_{\rm D}$ was enhanced due to the substitution of a-Si:H by nc-Si and the much higher doping efficiency within the later. $c_{\rm O}$ in the nc-SiO_x:H films did not change in this region and $E_{\rm 04}$ was reduced. This reduction in $E_{\rm 04}$ most likely stemmed from a substitution of a-Si:H by nc-Si, which exhibits a higher α at $\lambda > 700\,\mathrm{nm}$ [40]. In contrast, α in the wavelength (λ) range of light below 700 nm steadily decreased for higher $f_{\rm H_2}$ as expected by this substitution (not shown). The decreasing amount of a-Si:H was also indicated by a decrease of the peak around $2000\,\mathrm{cm}^{-1}$ in Fig. 4.5 f). The amount of a-SiO_x:H did not change significantly as compared to the fully amorphous films according to the FTIR spectra, which is also in accordance with the overall decreasing $E_{\rm 04}$ due to the substitution of a-Si:H by nc-Si.

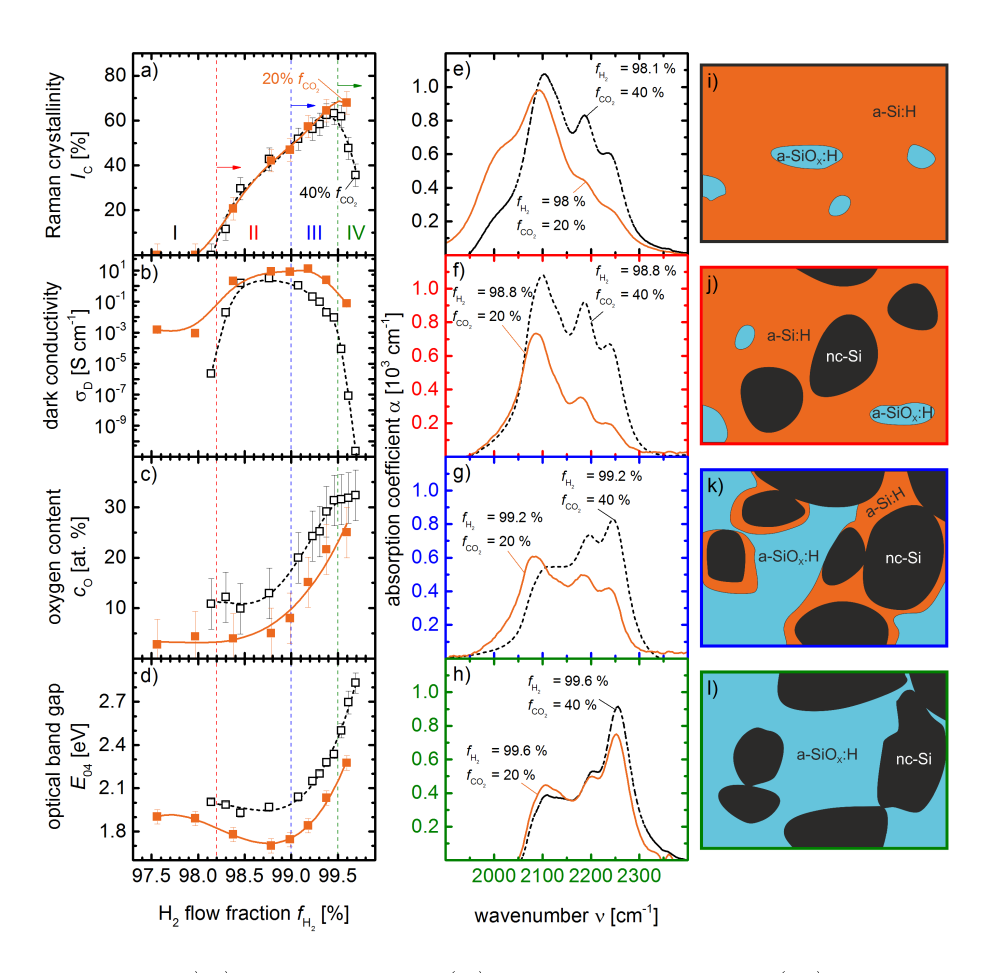


Figure 4.5.: a)-d) Raman crystallinity (I_c), electrical dark conductivity (σ_D), oxygen content (c_O), and optical band gap (E_{04}) of < n > nc-SiO_x:H films deposited at two different CO_2 gas flow fractions (f_{CO_2}) with a varying H_2 gas flow fraction (f_{H_2}). The deposition pressure (p) and deposition power (P) were fixed at 350 Pa and 50 W, respectively, with $f_{PH_3} = 5\%$. The dashed vertical lines roughly separate different regions of nc-SiO_x:H deposition. Starting at low f_{H_2} , these are the "fully amorphous region" (I), the "onset of nc-Si formation" (II), the "O and nc-Si enrichment" (III), and the "nc-Si deterioration" (IV). The lines serve as a guide to the eye. e)-h) FTIR spectra in the Si-H (s) range (1900-2400 cm⁻¹) of selected nc-SiO_x:H films exemplifying the corresponding deposition regions. i)-l) Sketches of the microstructure of nc-SiO_x:H films for the four different deposition regions. The following three phases are distinguished: hydrogenated amorphous silicon (s_i -Si-H), nanocrystalline silicon (s_i -Si), and O-rich hydrogenated amorphous silicon oxide (s_i -SiO_x:H).

Region III For the $f_{\rm H_2}$ series the third region was observed from $f_{\rm H_2}\approx 99\,\%$ on. It was named the "O and nc-Si enrichment" region and is distinguished by an increase in $c_{\rm O}$ and $I_{\rm c}$ (Fig. 4.5 c), d)). The increasing $c_{\rm O}$ was accompanied by an increase in $E_{\rm 04}$. Depending on the overall $c_{\rm O}$ even $\sigma_{\rm D}$ (Fig. 4.5 b)) may be affected by the high amount of the electrically resistive a-SiO_x:H. The increasing amount of O-rich a-SiO_x:H was evident from the increasing peak around $2250\,{\rm cm}^{-1}$ in Fig. 4.5 g), while the peak around $2100\,{\rm cm}^{-1}$ decreased. Similarly to the <p> nc-SiO_x:H in Sec. 4.1, $\sigma_{\rm D}$ was reduced for $c_{\rm O}$ beyond 20 at.% independently of $f_{\rm CO_2}$. This would correspond to a volume fraction of about 55% of nc-Si, assuming a simple mixture of Si and SiO₂ with their respective mass densities and molar masses. This estimate correlates well with the measured $I_{\rm c}$ for the onsets of the $\sigma_{\rm D}$ decline. Here, a high and still increasing amount of nc-Si is accompanied by a distinctive increase in the amount of O-rich a-SiO_x:H (Fig. 4.5 g)).

Region IV Lastly at $f_{\rm H_2} > 99.5\%$, the region of "nc-Si deterioration" was reached. This region is characterized by a high $c_{\rm O}$ and a decreasing $I_{\rm c}$ due to a large amount of O-rich a-SiO_x:H. Accordingly, the E_{04} of the films increased and $\sigma_{\rm D}$ was reduced. The FTIR spectra showed no a-Si:H related peak in the Si-H region any more (Fig. 4.5 h)) and a shift of the peak around 2100 cm⁻¹ towards the (OSi₂)Si-H (s) peak around 2130 cm⁻¹. Overall, this indicated that the a-Si:H phase had been fully substituted by nc-Si and a-SiO_x:H (Fig. 4.5 l)). The high amount of H at these $f_{\rm H_2}$, especially in combination with the VHF deposition, probably resulted in a strong etching of weak bonds during the deposition. The Si-Si bond has a lower bond energy within a-Si:H than nc-Si and is overall lower than the bond energy of the Si-O bond [149]. Therefore, the etching by H probably affected the a-Si:H more than the nc-Si or the a-SiO_x:H. However, an enhanced dissociation of CO₂ by H₂ may also be responsible for the favorable formation of a-SiO_x:H instead of a-Si:H or nc-Si at high $f_{\rm H_2}$ [140]. The sharp decline in $\sigma_{\rm D}$ can be attributed to the increase of O-rich a-SiO_x:H and a disruption of the nc-Si percolation paths by it. However, another possible explanation is a poor defect and grain boundary passivation of the nc-Si [32], which might result from the decline of a-Si:H in the films. Overall, the film properties were highly sensitive to small changes in $f_{\rm H_2}$ in this deposition region and, therefore, $f_{\rm H_2}$ had to be adjusted carefully.

In total, a wide range of optoelectronic properties has been achieved by the $f_{\rm H_2}$ variation for the <n> nc-SiO_x:H films and all four regions of nc-SiO_x:H deposition could be covered. This suggests the variation of $f_{\rm H_2}$ in combination with $f_{\rm CO_2}$ as an effective way to tune the microstructure and the optoelectronic properties of nc-SiO_x :H films. A variation of f_{H_2} has also been used for <p $> \text{nc-SiO}_x$:H films by Lambertz et al. [150], to obtain a high E_{04} in combination with a high $\sigma_{\rm D}$. In fact, the deposition pressure and deposition power optimization in Sec. 4.1.1 on nc-SiO_x:H films can also be related to changes in the amount of atomic H. Accordingly, the two deposition regimes that were found for the nc-SiO_x:H films correspond to the "O and nc-Si enrichment" and the "nc-Si deterioration" region (region III and IV) introduced here. In general, a phase mixture of conductive nc-Si percolation paths and transparent O-rich a-SiO_x:H is desired to achieve nc-SiO_x:H films with excellent optoelectronic properties. Therefore, the best trade-off between E_{04} and $\sigma_{\rm D}$ is expected for nc-SiO_x:H films close to the transition between the "O and nc-Si enrichment" (III) and the "nc-Si deterioration" (IV) region. Albeit, the doping within the nc-SiO_x:H and the distribution of the phases have a major impact on the resulting properties and need to be considered and adjusted as well.

4.2.2. Microstructure of the nc-SiO_x:H films

The microstructure of nc-SiO_x:H at the nanoscale is accessible by atom probe to-mography (APT). Consequently, this method allows to check the validity of the microstructure model directly. For this purpose, a <p> and a <n> nc-SiO_x:H film from the region of "O and nc-Si enrichment" (region III) were investigated by APT. The <n> nc-SiO_x:H film showed an E_{04} of 2.3eV and $\sigma_D \approx 0.1 \, \mathrm{S \, cm^{-1}}$ and the <p> film $E_{04} \approx 2 \, \mathrm{eV}$ and $\sigma_D \approx 0.2 \, \mathrm{S \, cm^{-1}}$. c_O , as determined by FTIR, was approximately 25 at.% and 21 at.%, respectively. These layers were chosen because they proved to be well suited for SHJ solar cells (see also chapter 5 and 6).

The APT results are presented in Fig. 4.6, 4.7 and 4.8 for both films. The iso density surfaces in Fig. 4.6 a) and c) were used to identify the nc-Si phase in a first approximation. These iso density surfaces were created by estimating the density of Si atoms within predefined volume portions of the reconstruction while taking into account the detector efficiency of the APT setup [128] (see also Sec. 3.2).

Here, the density of nc-Si was assumed to be $49.9\,\mathrm{nm}^{-3}$. The individual regions are clearly aligned along the direction of film growth and the lateral size of the columns is mostly limited to a few nm. Additionally, the positions of P and B within the microstructure are indicated by red and green dots in Fig. 4.6.

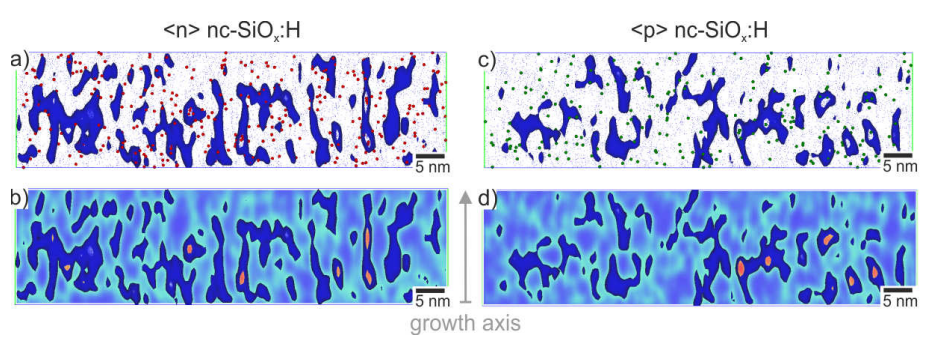


Figure 4.6.: a) Atom map of a slice of $20x75\,\mathrm{nm}^2$ and $2\,\mathrm{nm}$ thickness taken from the reconstruction of a $< n > nc\text{-}SiO_x$:H atom probe tomography (APT) tip. The blue dots indicate positions of Si atoms and the red dots represent the positions of P atoms. The blue areas show iso density surfaces of nc-Si. b) Combination of the nc-Si iso density surfaces with a Si density map of the same sample slice. The color indicates the Si density in the $2\,\mathrm{nm}$ slice, with blue denoting the lowest and red the highest density of Si. c), d) APT images of a $20x75x2\,\mathrm{nm}^3$ slice of a $nc\text{-}SiO_x$:H APT tip.

Figure 4.6 b) and d) show the density of Si ions detected within the nc-SiO_x:H slices. With decreasing Si density the areas could be related to the nc-Si, the a-Si:H, or the a-SiO_x:H phase. Overall, the density maps correlate well with the iso density surfaces from Fig.4.6 a) and c). A more detailed view on the distribution of nc-Si is given in Fig. 4.7. It shows strongly interconnected networks of individual nc-Si crystallites with dimensions of a few nm. Comparing the <n> and the <p> nc-SiO_x:H film, the total amount of nc-Si seemed to be less in the <p> nc-SiO_x:H, which may be related to the lower amount of nc-Si.

A proxigram (proximity histogram) analysis of each film is presented in Fig. 4.8 b) and d). Here, the iso density surface is taken as a reference point and the distance of each detected ion to this surface is determined [128], with "negative distances" resembling positions inside the Si nanocrystals. Thereby, an averaged

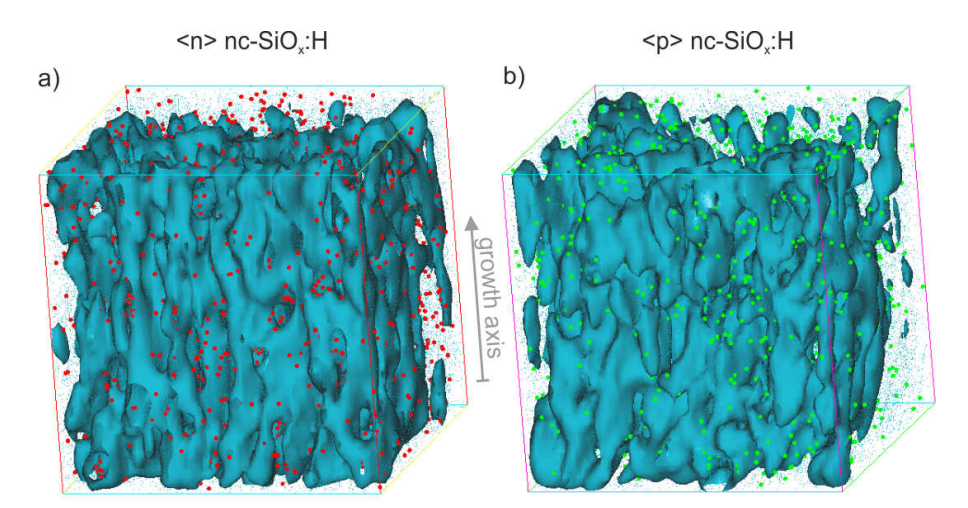


Figure 4.7.: Three-dimensional Si iso density surfaces of a < n > nc-SiO_x:H film (a)) and a nc-SiO_x:H film (b)) from the "O and nc-Si enrichment" region (region III). The total volume is 30x30x30 nm³. Turquoise dots indicate the positions of individual Si atoms, while red spheres indicate the positions of P atoms and green spheres resemble B. The axis of film growth is also included to illustrate the direction of the anisotropy of nc-Si growth.

concentration profile around the nc-Si surfaces was produced. This analysis showed similar concentrations of B and P towards the matrix as well as towards the inner nc-Si within a distance of 3nm in each direction. Furthermore, the proxigrams in Fig. 4.8 a) and c) show significant amounts of O and H within the nc-Si phase as defined by the iso density surfaces, even though a distinct decrease in O as well as H was observed at the nc-Si surface. Furthermore, the proxigrams displayed a peak in $c_{\rm O}$ about 1nm from the nc-Si surface for both types of nc-SiO_x:H films. Additionally, the C content was confirmed to be elevated in the <p> nc-SiO_x:H film at about 1 at.% as compared to about 0.4 at.% for the <n> film (see also Fig. 4.8 b), d)), which is in agreement with the FTIR results from Sec. 4.1.2.

The columnar structure and the dimensions of the nc-Si network as determined via APT correlate well with reports from transmission electron microscopy (TEM) investigations on nc-SiO_x:H films [17,18,22,23,33]. However, the anisotropy of nc-Si growth and the three-dimensional network distribution were more apparent from the APT representations. Accordingly, the extensive lateral interconnections can be

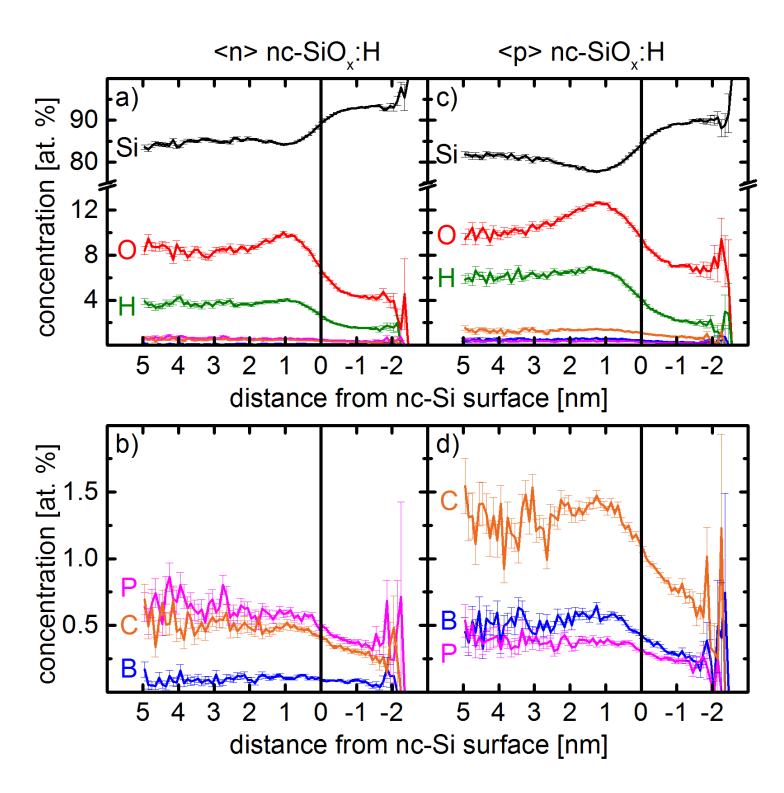


Figure 4.8.: a) Proxigram of Si, O, and H for the < n > nc-SiO_x:H film. The concentration of each element is displayed at a specific distance from the nc-Si surface as defined in Fig. 4.7 a). b) Proxigram of C, P, and B for the same film. c), d) Proxigrams for the nc-SiO_x:H film.

related to the high σ_D of the films. Nevertheless, the current flow through these layers in a SHJ solar cell is mainly transversal and therefore the crucial σ can be expected to surpass the lateral σ_D [108].

The crystalline volume fraction of nc-Si within this sample slices was estimated from the ratio of atoms within the nc-Si volume to the total number of atoms within the specimen. The, thereby determined, nc-Si volume fractions were 27 vol.% and 20 vol.% for the <n> and <p> nc-SiO_x:H films, respectively. For the <p> nc-SiO_x:H film this corresponded well to $I_c = 20\%$. However, for the <n> nc-SiO_x:H an I_c of 47% seems to overestimate the difference in the crystalline

volume fraction between these two films, even though a higher crystallinity was confirmed for the $\langle n \rangle$ film. This might be due to a thickness dependence of the crystalline volume fraction (see also Sec. 4.3) and the different sample depths being probed by the different methods, a few hundred nm towards the surface for Raman spectroscopy and the middle of the sample for APT in this particular case.

The high O and H content within the approximated nc-Si phase (Fig. 4.8 a), c)) indicate that at least some of the regions enveloped by the specified iso density surfaces probably do not contain nc-Si. Furthermore, different evaporation fields and surface curvatures for different phases can lead to so called "local magnification effects" and trajectory aberrations [126, 128]. These effects distort the origin of a given ion, and thereby affect the reliability of the determined atom densities. In total, these effects impede the unambiguous determination of the nc-Si phase by APT. The projection of O into nc-Si in APT has also been reported for Si nanocrystals embedded in a SiO₂ matrix [151].

Furthermore, an O-enriched shell is indicated around the nc-Si phase by the proxigrams in Fig. 4.8. However, this feature may be related to the microstructure of the nc-SiO_x :H films and result from an average distance between the nc-Si phase and O-rich a-SiO_x:H of about 1 nm. Accordingly, the distance between neighboring regions of nc-Si is about 2-3 nm in the Si iso density plots (Fig. 4.6).

The similar dopant concentrations within the nc-Si and the matrix phase in Fig. 4.8 b) and d) are in contrast to simulation results, which predict the preferred incorporation of dopant atoms at the interface of Si nanocrystals [39,152]. Furthermore, increased dopant concentrations were found by APT at the Si interface of thermally grown Si nanocrystals embedded in glass [34]. This indicates either that the growth conditions during the PECVD suppress a repositioning of the dopants to their thermodynamically favored sites, or that the accumulation of dopants at the interface is not energetically favored for the deposited nc-SiO_x:H films due to the large crystallite size of the nc-Si as compared to Si quantum dots, where a self-purifying effect is expected.

Surprisingly, the P and B content within the <p> > nc-SiO_x:H film was very similar, indicating a codoped film (Fig. 4.8 d)). This might be a consequence of cross contamination from the chamber walls, even though a cover layer of about 70 nm

4. Material development

was deposited prior to the film deposition. Another source of P might have been the sample carrier. This cross contamination raises the question whether active dopants of P or B were responsible for the high σ_D within the nc-SiO_x:H film. Nevertheless, this film still behaved like a p-type doped layer when applied in SHJ solar cells (see also Sec. 5). Therefore, this effect can be related to cross contamination from the named sources for this specific sample and should not be valid for <p> nc-SiO_x:H in general. However, cross contamination should be avoided by applying appropriate cover layers whenever depositions of opposite doping type are performed that use the same sample carrier or chamber.

The APT elemental density images for Si and O were combined and simplified in Fig. 4.9 to investigate the distribution of O with respect to the nc-Si and directly compare the APT images to the sketches from the microstructure model (Fig. 4.5). Please note that the voxel size is smaller than in Fig. 4.6 and Fig. 4.9. In fact, slices of 0.5 nm thickness were used instead of the previously used 2 nm. Consequently, the apparent distribution of nc-Si is different for these two figures. A density threshold was defined similarly to the Si iso density images to define areas of nc-Si, a-Si:H, and O-rich a-SiO_x:H. For a-Si an atomic density of 2% less as compared to crystalline Si was assumed [153, 154], which is even lower for a-Si:H [155]. The a-SiO_x:H phase was arbitrarily limited to areas of $c_{\rm O} > 10\%$.

For the <n> nc-SiO_x:H film in Fig. 4.9 a), the areas of high $c_{\rm O}$ and the nc-Si regions are well separated with only a few regions of $c_{\rm O} \ge 20\%$. The white intermediate regions can be related to either a-Si:H or a-SiO_x:H with a low $c_{\rm O}$. In total, the distribution and ratio of the phases is well reproduced in comparison to the sketch of the microstructure in Fig. 4.5 k), corresponding to a film within the "nc-Si and O enrichment" region (region III). However, the overall amount of O was lower than expected. A significantly underestimated $c_{\rm O}$ in SiO₂ by APT has recently been reported by Kinno et al. [127] and suggested to result from direct current (DC) evaporation of atoms or desorption of neutral O₂. Therefore, the real $c_{\rm O}$ can be expected to be higher in the nc-SiO_x:H films, as suggested by the FTIR results. The amount of a-Si:H is nearly negligible according to the defined density criteria. Similarly, only a low amount of a-Si:H was expected within both nc-SiO_x:H films from their FTIR spectra as they were deposited close to the "nc-Si deterioration"

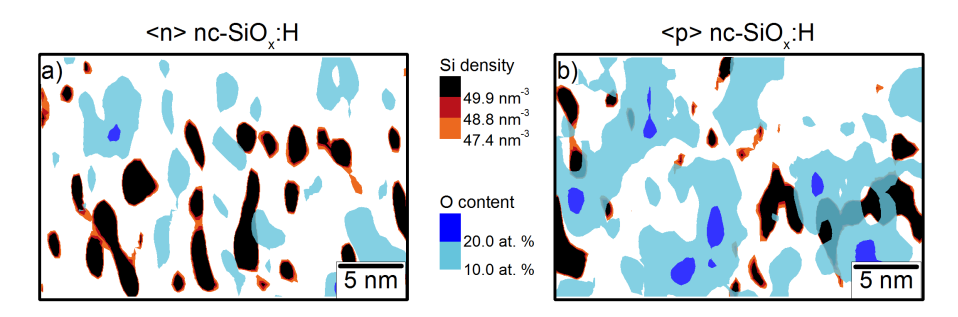


Figure 4.9.: a) Combination of a Si density map and a O concentration map for a $30x20x0.5\,\mathrm{nm}^3$ slice of $< n > nc\text{-}SiO_x$:H. The black areas were adjusted to match the density of c-Si. The red area represents non-hydrogenated a-Si, defined by a 2% lower density as compared to nc-Si [153, 154] and the orange areas represent a-Si:H with a 5% lower Si density as compared to nc-Si (at a c_H of 9 at.%) [155]. The O map shows areas of medium c_O (from 10 to 20 at.%) in cyan and O-rich areas in blue. Consequently, the white areas represent regions of a Si density below 47.4nm⁻³ and $c_O \le 10$ at.%. b) Si density map for a $30x20x0.5\,\mathrm{nm}^3$ slice of $nc\text{-}SiO_x$:H including the respective c_O map. The areas were defined according to a).

(IV) region (for example see Fig. 4.10 a)). Nevertheless, an unambiguous distinction of a-Si:H from nc-Si cannot be drawn by APT as pointed out before.

Similarly to the <n> nc-SiO_x:H, the density maps of the <math><p> nc-SiO_x:H film in Fig. 4.9 b) correspond well to the microstructure model. However, there is some overlap between the a-SiO_x:H and the nc-Si phases, which led to a significant c_O within the nc-Si phase in Fig. 4.8 a) and c). This can be attributed to the effects discussed in the previous paragraph, which distort the positions of Si and O, especially if they originated from different phases.

4.2.3. Practical use of the model

Effective doping of nc-SiO_x:H films is an essential prerequisite for high performance films. However, as already demonstrated for <p> nc-SiO_x:H in Sec. 4.1.2, the dopant gas may influence the structure of the films in addition to the doping effect. In Fig. 4.10 two <n> nc-SiO_x:H series of varying PH₃ gas flow fraction ($f_{\rm PH_3}$) are

4. Material development

shown. Two disparate deposition regimes were chosen to investigate the effect of changing $f_{\rm PH_3}$. The films of the first deposition regime were deposited at $P=50\,\rm W$, $p=350\,\rm Pa$, $f_{\rm CO_2}=30\,\%$, and $f_{\rm H_2}=99.65\,\%$. The second sample series was produced at $P=30\,\rm W$, $p=50\,\rm Pa$, $f_{\rm CO_2}=20\,\%$, and $f_{\rm H_2}=99.2\,\%$. The classification of the films was carried out according to Sec. 4.2.1 by analyzing their FTIR spectra (Fig. 4.10 a)). The first series can be assigned to the "nc-Si deterioration" region (region IV) due to a strong (O₃)Si-H (s) peak and a low intensity of the modes around 2100 cm⁻¹. The films of the second deposition regime belong to the "O and nc-Si enrichment" class (region III), characterized by a-Si:H related peaks, while displaying a high E_{04} and $\sigma_{\rm D}$. Thereby, these two deposition regimes represent highly conductive as well as highly transparent nc-SiO_x:H films, both of which might be suitable for SHJ solar cells.

Films of both regimes showed similar I_c and c_O (Fig. 4.10 b)), which did not change with varying f_{PH_3} . Likewise, the FTIR spectra of these films hardly changed with f_{PH_3} . Therefore, an increase in f_{PH_3} does not seem to affect the microstructure of the nc-SiO_x:H films, in contrast to $f_{B(CH_3)_3}$. Here, I_c should not be taken as a measure of the crystalline volume fraction, however, because for an overall c_O of 30% even a pure mixture of SiO₂ and c-Si could only have a maximum crystalline volume fraction of about 40 vol.%. Therefore, I_c is overestimating the nc-Si volume fraction for the presented films (see also Sec. 4.2.1). In contrast to I_c and c_O , σ_D increased by about one order of magnitude by raising f_{PH_3} from 2% to 5% for both deposition regimes. This indicates an increased doping of the nc-Si and eventual a-Si:H phase, which resulted in an increased density of active charge carriers [89]. E_{04} was constant for the "O and nc-Si enrichment" nc-SiO_x:H films (region III) and was slightly reduced for the films in the "nc-Si deterioration" region (region IV).

Overall, an increasing $f_{\rm PH_3}$ mainly affected the conductivity of the nc-SiO_x:H films in both deposition regions by an increase of the charge carrier density without affecting the microstructure. Similar results were reported for RF nc-SiO_x:H films by Ding et al. [89]. Consequently and in contrast to $f_{\rm B(CH_3)_3}$, $f_{\rm PH_3}$ should be maximized to obtain material with improved optoelectronic properties.

In Sec. 4.2.1 high performance nc-SiO_x:H films were postulated to lie between the "O and nc-Si enrichment" (III) and the "nc-Si deterioration" (IV) regions. Ac-

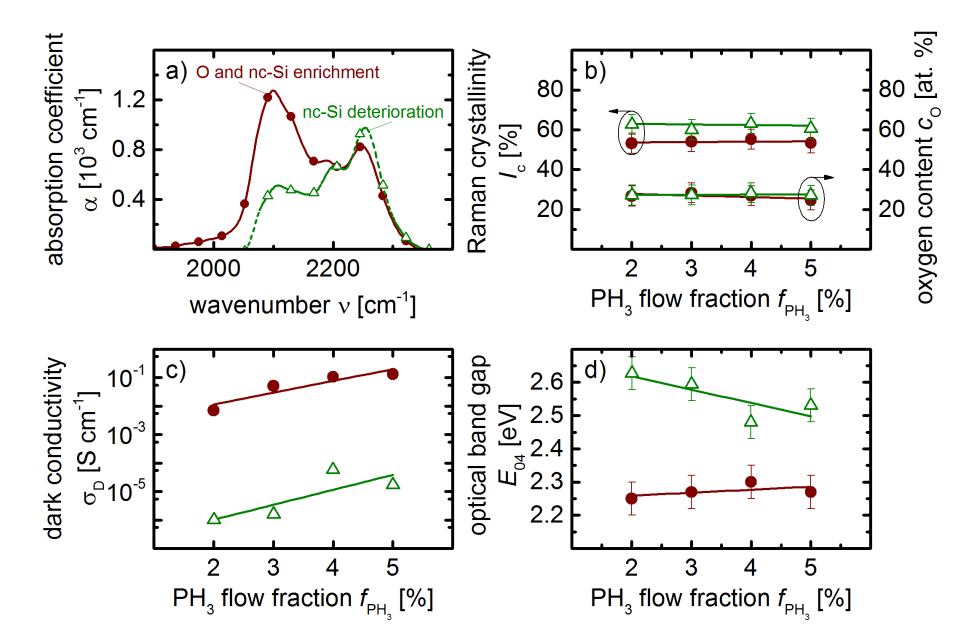


Figure 4.10.: a) FTIR spectra in the Si-H (s) band range (1900-2400 cm⁻¹) for two representative $\langle n \rangle$ nc-SiO_x:H films deposited at $f_{PH_3}=4\%$ in two different deposition regimes. The films of the "O and nc-Si enrichment" region (region III) were deposited at $P=30\,\mathrm{W}$, $p=50\,\mathrm{Pa}$, $f_{CO_2}=20\,\%$, and $f_{H_2}=99.2\,\%$ and the films of the "nc-Si deterioration" region (region IV) were deposited at $P=50\,\mathrm{W}$, $p=350\,\mathrm{Pa}$, $f_{CO_2}=30\,\%$, and $f_{H_2}=99.65\,\%$. b) Raman crystallinity (I_c) and oxygen content (c_O) of the nc-SiO_x:H films for different f_{PH_3} . c), d) Dependence of the electrical dark conductivity (σ_D) and the optical band gap (E₀₄) on f_{PH_3} for the two deposition regimes. The lines serve as a guide to the eye.

cordingly, two films were chosen from this area to optimize the optoelectronic properties of <n>nc-SiO_x:H at a maximum $f_{\rm PH_3}$ of 5%. Furthermore, $f_{\rm CO_2}$ was selected as an effective way to adjust the amount of SiO₂ in the nc-SiO_x:H films as has been demonstrated for <p>nc-SiO_x:H in Sec. 4.1.2. The films were deposited at $P=50\,{\rm W},\ p=350\,{\rm Pa},\ f_{\rm PH_3}=5\%,$ and $f_{\rm H_2}=99.4\%.$

The results of changing $f_{\rm CO_2}$ for <n> nc-SiO_x:H in this promising deposition region are summarized in Fig. 4.11. Similarly to the results in Sec. 4.1.2, increasing $f_{\rm CO_2}$ from 10 to 60% led to a marked increase in $c_{\rm O}$. $I_{\rm c}$ was not affected, however. This is because, in contrast to the $f_{\rm CO_2}$ variation for nc-SiO_x:H, $f_{\rm CO_2}$ was

4. Material development

varied at a constant $f_{\rm H_2}$ (Eq. 4.2) for this sample series. In Sec. 4.1.2, however, the increase in $f_{\rm CO_2}$ was being accompanied by a slight increase in $f_{\rm H_2}$ from 99.55% to 99.65% for the samples deposited at $P=70\,\rm W$ and from 99.5% to 99.75% for the samples deposited at $P=30\,\rm W$. The reason is that a different definition of $f_{\rm H_2}$, which included the CO₂ flow in the denominator [112], was used for these depositions as compared to Eq. 4.2. Nevertheless, due to the small change in $f_{\rm H_2}$ the main contribution to the observed changes in the film properties was assumed to lie in $f_{\rm CO_2}$ (see also Sec. 4.2.1), especially as the effect of $f_{\rm CO_2}$ on $f_{\rm CO_2}$ and $f_{\rm CO_2}$ was consistent with literature data [17,85,89]. Therefore, the slight reduction of $f_{\rm CO_2}$ for increasing $f_{\rm CO_2}$ beyond 10% in Sec. 4.1.2 is attributed to the steadily increasing $f_{\rm H_2}$.

Whereas, the nearly constant and $f_{\rm CO_2}$ independent $I_{\rm c}$ in Fig. 4.11 a) corresponds well to the observations in Sec. 4.2.1 for a constant $f_{\rm H_2}$ in the same deposition region. The increased incorporation of O resulted in a decrease of the a-Si:H phase and an increase of the O-rich a-SiO_x:H phase as indicated by a change in the respective peaks in the FTIR spectra (Fig. 4.11 c) and d)). This increasing amount of a-SiO_x:H led to a linear increase of E_{04} with increasing $f_{\rm CO_2}$ (Fig. 4.11 b)), but at the same time steadily reduced $\sigma_{\rm D}$ as the depositions gradually shifted towards the "nc-Si deterioration" region (region IV).

Altogether, these <n>nc-SiO_x:H films exhibited excellent optoelectronic properties as compared to all other nc-SiO_x:H films deposited in the course of this work and compared to literature data (see also Fig. 4.14). This was achieved by a controlled addition of O-rich a-SiO_x:H through a variation of $f_{\rm CO_2}$ in the "O and nc-Si enrichment" region (region III), thereby exemplifying the usefulness of the microstructure model for the development of high performance nc-SiO_x:H films.

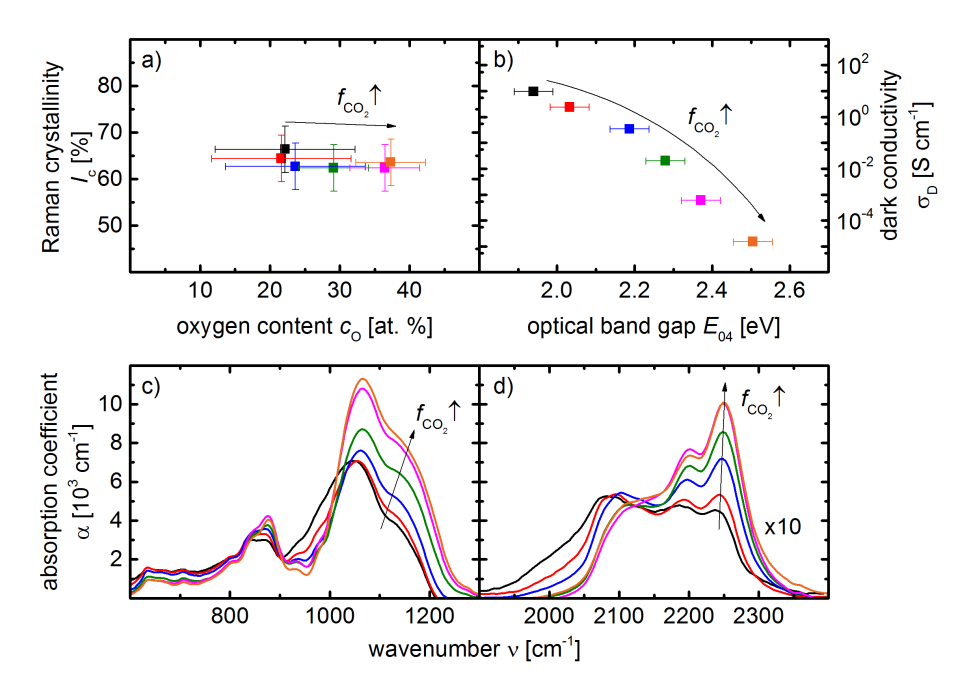


Figure 4.11.: a) Relation between the Raman crystallinity (I_c) and the oxygen content (c_O) for varying the CO_2 gas flow fraction (f_{CO_2}) from 10 to 60% in <n $> nc-SiO_x$:H films deposited at $P=50\,\mathrm{W}$, $p=350\,\mathrm{Pa}$, $f_{PH_3}=5\,\%$, and $f_{H_2}=99.4\,\%$. b) Relation between the optical band gap (E_{04}) and the electrical dark conductivity (σ_D) for $f_{CO_2}=10..60\,\%$. c), d) FTIR spectra of the nc-SiO_x:H films in the range of 600-1300 cm⁻¹ and 1900-2400 cm⁻¹ (enlarged tenfold), respectively. Arrows indicate the direction of increasing f_{CO_2} .

4.3. Comparison of n- and p-type VHF/RF nc-SiO_x:H

A wide range of and < n > nc-SiO_x:H films were deposited in the course of the material development for VHF depositions. An overview of their optical and electrical properties is given in Fig. 4.12 a) and b), respectively. At lower $c_{\rm O}$ the VHF nc-SiO_x:H showed a similar dependence of $E_{\rm 04}$ on $c_{\rm O}$ for < n > and nc-SiO_x:H films. This is typically the region of "nc-Si onset" (region II) or even "fully amorphous" (region I) films where only low amounts of a-SiO_x:H phase were present. For $c_{\rm O}$ beyond about 25 at.% $E_{\rm 04}$ of < n > nc-SiO_x:H was significantly higher than for the material for any given $c_{\rm O}$. The lower $E_{\rm 04}$ of the films can be

4. Material development

explained by the higher amount of a-Si:H in <p> nc-SiO_x:H due to the B(CH₃)₃, which leads to an increase in α for λ below about 700 nm and thereby a shift of E_{04} to lower energies. This was confirmed by comparing $\alpha(\lambda)$ for several <n> and <p> nc-SiO_x:H films of comparable $c_{\rm O}$ (not shown).

Similarly to $c_{\rm O}$ and E_{04} , $\sigma_{\rm D}$ is closely linked to $I_{\rm c}$ of a nc-SiO_x:H film. Generally, an increase in $I_{\rm c}$ leads to an increasing $\sigma_{\rm D}$ due to the correlation with the amount of the highly conductive nc-Si phase. The <p> nc-SiO_x:H films displayed an overall lower $I_{\rm c}$ compared to the <n> films due to the aforementioned crystallinity inhibiting effect of B(CH₃)₃ [137–139]. Accordingly, the maximum achieved in $\sigma_{\rm D}$ was also higher for <n> nc-SiO_x:H than for <p> nc-SiO_x:H.

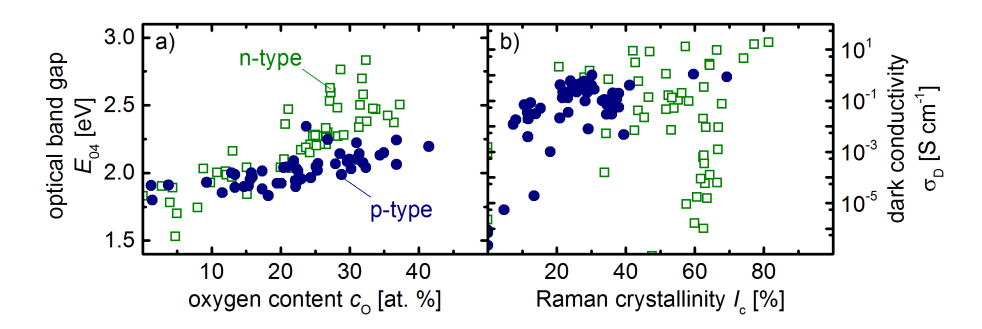


Figure 4.12.: a) Relation between the optical band gap (E_{04}) and the oxygen content (c_O) for all $\langle n \rangle$ and $\langle p \rangle$ nc-SiO_x:H films deposited at VHF in this study including μ c-Si:H films. b) Dependence of the electrical dark conductivity (σ_D) on the Raman crystallinity (I_c) for all nc-SiO_x:H films.

The thickness (d) of the nc-SiO_x:H films is an important aspect not only for their characterization, but also for the implementation of these films in SHJ solar cells. Similarly to μ c-Si:H [156–158] films, the properties of nc-SiO_x:H films were reported to depend on d due to the existence of an incubation layer towards the substrate interface [109, 159]. This incubation layer may exceed 100 nm and should be considered when analyzing films in this thickness range. In Fig. 4.13 $c_{\rm O}$ and $I_{\rm c}$ are displayed in dependence on the film thickness for all investigated nc-SiO_x:H films. Below a critical thickness of about 100 nm $c_{\rm O}$ as determined by FTIR rapidly increased, indicating predominant incorporation of O-rich a-SiO_x:H

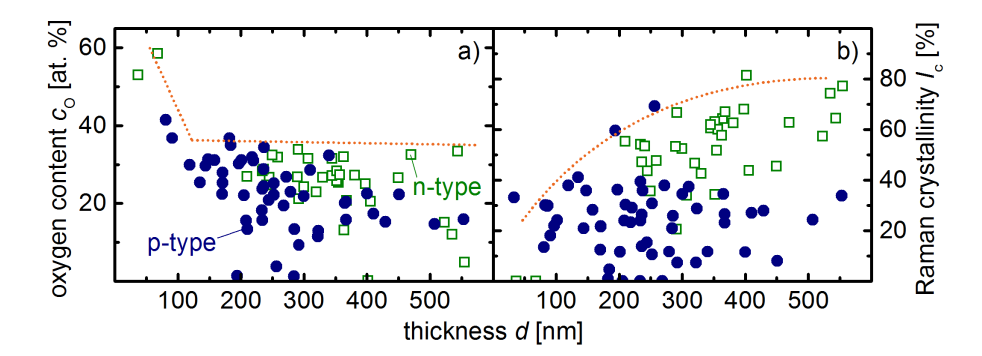


Figure 4.13.: Film thickness (d) dependence of a) the oxygen content (c_O) and b) the Raman crystallinity (I_c) for the < n > and nc-SiO_x:H films produced in this study. The dashed lines serve as a quide to the eye.

in the films (Fig. 4.13 a)). Also, I_c decreased towards a lower d. All in all, these findings imply the formation of an incubation layer with a thickness of at least several tens of nm for the investigated nc-SiO_x:H films. Similar results were found by Smirnov et al. [17, 109] by investigating the thickness dependence of I_c for <n>c-SiO_x:H films from 20 to 700 nm [109] and observed in high resolution transmission electron microscopy (HRTEM) images [17]. In comparison to μ c-Si:H films the incubation layer thickness was strongly reduced for nc-SiO_x:H [109], implying significant changes in the growth process of the nc-Si phase in the latter films. The existence of an a-SiO_x:H rich incubation layer was also indicated by simulation results obtained in Sec. 5.2.3.

The performance of the nc-SiO_x:H films, developed at VHF, is compared to current research results in Fig. 4.14 a). Here, E_{04} of each film is combined with the achieved σ and thereby provides a way to evaluate the optoelectronic performance of the material. Ideally, a nc-SiO_x:H film with a high E_{04} and a high σ_D is desirable, albeit a trade-off is observed between these two properties. Overall, nearly identical results were achieved as compared to the best nc-SiO_x:H films deposited at RF by Lambertz et al. [32]. Furthermore, an extensive range of optoelectronic properties was covered by the previously described optimization of the deposition parameters, which allows for targeted tailoring of the properties towards the specific demands

4. Material development

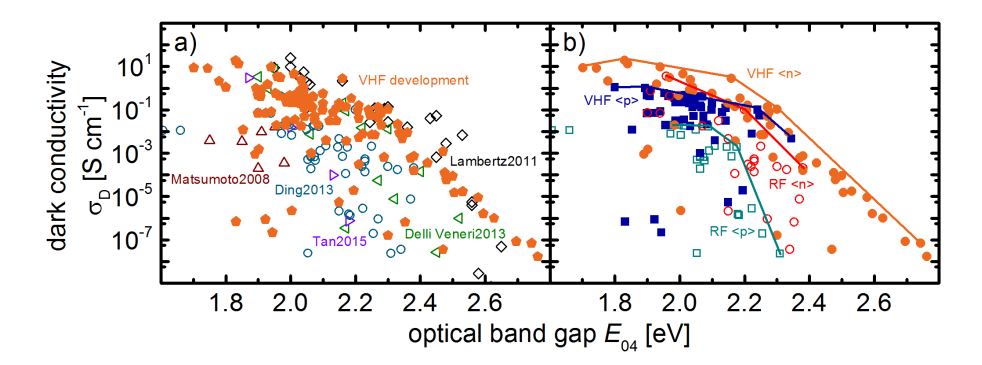


Figure 4.14.: The electrical dark conductivity (σ_D) over the optical band gap (E_{04}) as a measure of the optoelectronic performance of the <n> and <p> nc-SiO $_x$:H films deposited in the course of this work. a) Comparison to literature data of nc-SiO $_x$:H films. The data was taken from [22, 29, 32, 89, 160]. b) Comparison of the VHF <n> and <p>nc-SiO $_x$:H films to nc-SiO $_x$:H films developed at RF (13.56 MHz) at the same deposition system [49, 89]. The VHF material is represented by filled symbols, while open symbols indicate nc-SiO $_x$:H films deposited at RF. The added lines mark the approximate performance limits of the films.

of the application. A comparison to the results obtained from RF development of $nc-SiO_x$:H films at the same deposition system is presented in Fig. 4.14 b). For the $< n > nc-SiO_x$:H films only a minor improvement of σ_D could be achieved at any given E_{04} by increasing the deposition frequency to 81.4MHz. In case of $nc-SiO_x$:H, however, σ_D was significantly enhanced by the optimization at VHF as compared to the RF material, especially for the highly transparent films. This can be attributed to the crystallinity enhancing effect of the increased frequency [135, 136].

Following the material development of hydrogenated nanocrystalline silicon oxide (nc-SiO_x:H) layers, they were applied in silicon heterojunction (SHJ) solar cells to enhance the light response of these cells, especially in the short wavelength (λ) region. This chapter comprises the development of planar SHJ solar cells with nc-SiO_x:H layers serving as emitter, back surface field (BSF), and front surface field (FSF) layers. The first section discusses the application of nc-SiO_x:H layers in planar solar cells, passivated by hydrogenated amorphous silicon oxide (a-SiO_x:H). The second section covers hydrogenated amorphous silicon (a-Si:H) passivated planar SHJ solar cells with nc-SiO_x:H layers in a rear-emitter configuration. In the third section the application of nano-imprint lithography (NIL) to produce anti-reflection (AR) coatings on planar SHJ solar cells is presented.

5.1. a-SiO_x:H passivated solar cells

Similarly to the optical advantage of nc-SiO_x:H in comparison to a-Si:H, passivation layers of intrinsic (<i>) hydrogenated amorphous silicon oxide (a-SiO_x:H) exhibit a higher optical band gap (E_{04}) than <i>> a-Si:H passivation layers and, thereby, offer a way to reduce parasitic absorption in SHJ solar cells [61, 64, 85]. Furthermore, a-SiO_x:H layers show a superior performance in SHJ solar cells at elevated temperatures [64] and are less prone to epitaxial growth of Si, which can detrimentally affect the passivation quality [83]. The following <i>> a-SiO_x:H passivation layers were deposited in the same chamber as the n-type doped (<n>>) and p-type doped (<p>>) nc-SiO_x:H layers and silane (SiH₄), carbon dioxide (CO₂), and

hydrogen (H_2) were used as precursor gases. The optimization of the deposition parameters with respect to an optimum passivation quality had been carried out by Einsele [161] and Ding [112].

In the first part of this section the effect of the a-SiO_x:H thickness is investigated by exploiting the inhomogeneity in the deposition rate $(r_{\rm dep})$ during the a-SiO_x:H deposition. The second part focuses on the variation of the <n>> nc-SiO_x:H emitter layers in fully SiO_x:H based SHJ solar cells and its effects on the solar cell properties. Furthermore, the effect of two different indium tin oxide (ITO) layers on the solar cell parameters is discussed. Finally, a comparison between solar cells in a front- and a rear-emitter design is given in the third part of this section.

5.1.1. a-SiO_x:H passivation layers

The effect of the <i>a-SiO_x:H passivation layers with an oxygen content (cO) of about 5 at.% was investigated in planar SHJ solar cells with nc-SiO_x:H emitter and BSF layers. The complete stack of layers for the solar cells is presented in Fig. 5.1 a). The optimal thicknesses of the doped layers and the ITO were taken from [112]. Both doped nc-SiO_x:H layers were deposited in the "O and nc-Si enrichment" region to achieve a high optoelectronic performance as discussed in Sec. 4.2.1. The <p> nc-SiO_x:H was deposited at $P=30\,\mathrm{W}$, $p=50\,\mathrm{Pa}$, $f_{\mathrm{B(CH_3)_3}}=3.8\,\%$, $f_{\mathrm{CO_2}}=20\,\%$, and $f_{\mathrm{H_2}}=99.5\,\%$, thereby combining a high electrical dark conductivity (σ D) of 0.3S cm⁻¹ with an E_{04} of 2.0 eV. The <n> nc-SiO_x:H at the front of the solar cell was deposited at $P=30\,\mathrm{W}$, $p=50\,\mathrm{Pa}$, $f_{\mathrm{PH_3}}=5\,\%$, $f_{\mathrm{CO_2}}=20\,\%$, and $f_{\mathrm{H_2}}=99\,\%$, which resulted in an E_{04} of 2.3 eV with $\sigma_{\mathrm{D}}=0.1\,\mathrm{S\,cm^{-1}}$. The stepwise fabrication of the solar cells is described in Sec. 3.1.

The cell layout on the $10 \,\mathrm{cm}$ wafer is shown in Fig. 5.1 b) and with a photograph in Fig. 5.1 c). On each wafer eight $1\mathrm{x}1\,\mathrm{cm}^2$ cells were defined. Cell number 6 was designed to be without a contacting grid in order to determine the active area external quantum efficiency (EQE) and R of the solar cells. The Ag grid on the other solar cells included 5 fingers of 9 mm in length and 50 μ m in width. They were connected by a busbar of $0.3\mathrm{x}9\,\mathrm{mm}^2$, which was externally accessible via a $1\mathrm{x}2\,\mathrm{mm}^2$ contacting pad. Furthermore, the cell design included four $2\mathrm{x}2\,\mathrm{cm}^2$ cells

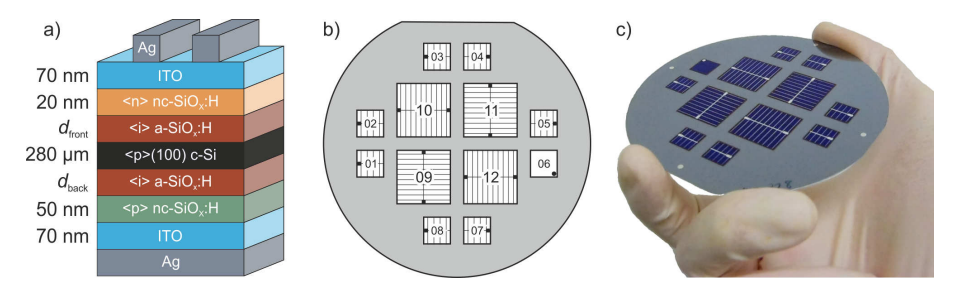


Figure 5.1.: a) Layer stack of the SHJ solar cells used for the a-SiO $_x$:H thickness variation (not to scale). A polished float-zone (FZ) Si wafer with a nominal resistivity of $1-5\,\Omega$ cm was used as the substrate. b) Layout of the cells on a polished Si wafer of 10 cm in diameter. The cells 1 to 8 are $1x1\,\mathrm{cm}^2$ and cells 9 to 12 are $2x2\,\mathrm{cm}^2$. Cell 6 is designated for differential spectral response (DSR) and reflectance (R) measurements and has no Ag grid on it. Nominally 6.5% and 4.5% of the total cell area are covered by the Ag grid for the $1x1\,\mathrm{cm}^2$ and the $2x2\,\mathrm{cm}^2$ cells, respectively. c) Picture of a complete planar silicon heterojunction (SHJ) solar cell with the cell areas defined by locally deposited ITO through a shadow mask.

on each wafer. Each of these cells had 10 grid-fingers on it and 2 contacting pads per busbar. All Ag fingers were evaporated to a thickness of $2\,\mu\text{m}$, while the busbars and full area rear Ag contact were $0.7\,\mu\text{m}$ thick. In total, the grid coverage on the front of the solar cells was about $8\,\%$ for the $1\text{x}1\,\text{cm}^2$ cells and $5\,\%$ for the $2\text{x}2\,\text{cm}^2$ if a shadow mask of $0.9\text{x}0.9\,\text{cm}^2$ and $1.9\text{x}1.9\,\text{cm}^2$ was applied, respectively. In the following, the results from the $1\text{x}1\,\text{cm}^2$ cells are presented, unless stated otherwise.

The benefits of including <i>a-SiO_x:H passivation layers in SHJ solar cells are demonstrated in Fig. 5.2. The detailed deposition conditions for the a-SiO_x:H layers can be found in [112]. Without a passivation layer, a high defect density at the Si wafer interface results in extensive recombination of charge carriers, resulting in a low effective carrier lifetime ($\tau_{\rm eff}$) of about 10 μ s at an excess charge carrier density of 10^{15} cm⁻³ and an open circuit voltage ($V_{\rm oc}$) below 600 mV for the solar cell. Applying passivation layers of <i>> a-SiO_x:H to the solar cell led to a significant increase of $V_{\rm oc}$ due to a reduced defect density at the Si wafer interface. The passivation mechanism of <i>> a-SiO_x:H is mainly attributed to chemical passivation [162]. Moreover, H was suggested as the main passivating species [85, 162], similarly to <i>> a-Si:H layers.

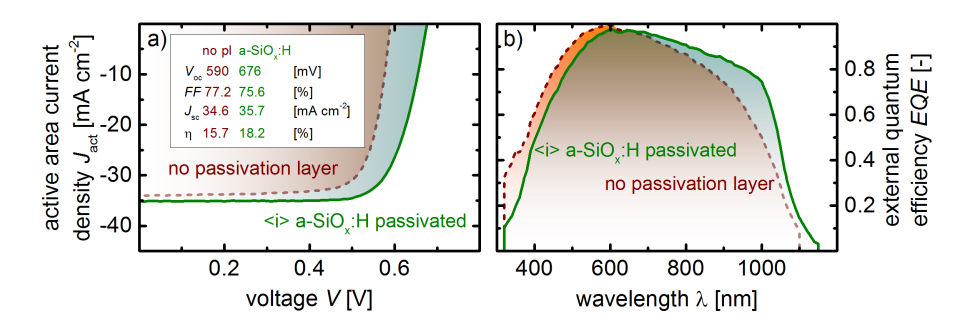


Figure 5.2.: a) Current-voltage characteristics of two SHJ solar cells. One was produced without any passivation layer (pl) and the other with a 4nm thick $\langle i \rangle$ a-SiO_x:H layer on the front and 8nm a-SiO_x:H at the rear [49]. The inset lists the solar cell parameters for each cell. b) Comparison of the active area external quantum efficiency (EQE) of the two cells.

Accompanying the increase in $V_{\rm oc}$, the fill factor (FF) of the solar cell was reduced due to an increased series resistance $(R_{\rm s})$. In fact, the highly insulating <i>> a-SiO_x:H layer introduces a barrier to the electrical transport of charge carriers, especially for holes, due to the large valence band offset of the a-SiO_x:H layer towards the Si wafer [61].

Figure 5.2 b) shows the effect of the passivation layer on the EQE of the solar cell. The gain in short circuit current density $(J_{\rm sc})$ mainly stems from an increase in the EQE for $\lambda > 700\,\mathrm{nm}$. This is a combined effect of a reduced recombination at the rear of the solar cell, where the interface between the <p> wafer and the <p> nc-SiO_x:H BSF is located, and a change in the R spectrum of the solar cell. The change in R is due to the added a-SiO_x:H layers with a low real part of the refractive index (n) which is evident from a shift of the position of the EQE maximum and it led to a reduced EQE for $\lambda < 600\,\mathrm{nm}$. Additionally, the introduction of the front passivation layer is expected to have resulted in an increase of the parasitic absorption at the front of the solar cell. In total, the gain in the long λ range overcompensated this loss.

Next, the passivation quality of the <i>a-SiO_x:H layers was investigated and compared to former results [112]. For this, B-doped (100)-oriented FZ Si wafers of

280 µm thickness were cleaned (see also Sec. 3.1) and then symmetrically passivated with <i> a-SiO_x:H layers. The deposition time ($t_{\rm dep}$) was varied with a nominal $t_{\rm dep}$ of 2.9 Å s⁻¹, resulting in an a-SiO_x:H thickness (d) from 4 to 17 nm. The results are presented in Fig. 5.3 a). $t_{\rm eff}$ was strongly affected below a $t_{\rm dep}$ of about 30 s, corresponding to an a-SiO_x:H layer thickness of 9 nm. Furthermore, $t_{\rm eff}$ up to 3 ms were achieved for the highest $t_{\rm dep}$ in this as-deposited state of the a-SiO_x:H. This demonstrates the excellent passivation quality achievable by the a-SiO_x:H layers. Additionally, the previous results were well reproduced even after chamber cleaning and after alterations to the inner chamber layout.

Typically the passivation layer thickness in a SHJ solar cell is around 5 nm, corresponding to a $t_{\rm dep}$ of about 17 s. Accordingly, controlling the passivation layer thickness is crucial to achieve well passivated surfaces without negatively affecting the electrical transport through the solar cell because of the low conductivity of the a-SiO_x:H layers ($\sigma_{\rm D}\approx 10^{-11}\,{\rm S\,cm^{-1}}$). Therefore, the locally deposited thickness of the a-SiO_x:H layers was determined by depositing an a-SiO_x:H film of nominally 550 nm on a glass substrate of $10x10\,{\rm cm^2}$ and by measuring the film thickness at 40 positions (Fig. 5.3 b)). Consequently, the thickness of the <i> a-SiO_x:H layer could be related to the properties of each individual cell. The positions of the cells with respect to the local $r_{\rm dep}$ of the <i> a-SiO_x:H at the rear side are shown in Fig. 5.3 b).

Three wafers with different $t_{\rm dep}$ of a-SiO_x:H on the front and the rear side were prepared to investigate the dependence of the solar cell properties on d of the <i> a-SiO_x:H layers. The resulting d of the individual cells are displayed in Fig. 5.4. The wafers were turned and placed according to the inhomogeneity map in Fig. 5.3 b) to achieve a similar a-SiO_x:H layer thickness on the front and the rear side of each cell. In contrast, the standard turning of the wafer led to a thicker a-SiO_x:H layer at the front of cell number 5 and 6, while having a thickness below the nominal value at the rear. For cells 1 and 2 the thicknesses were reversed as compared to 5 and 6. The effect of the a-SiO_x:H layer d on the cell performance was found to be similar to the results published by Ding et al. [49]. In brief, the optimal front layer d was found to lie between 4 and 5 nm for a high $V_{\rm oc}$ without negatively affecting $J_{\rm sc}$ or FF. Furthermore, the thickness of the rear passivation

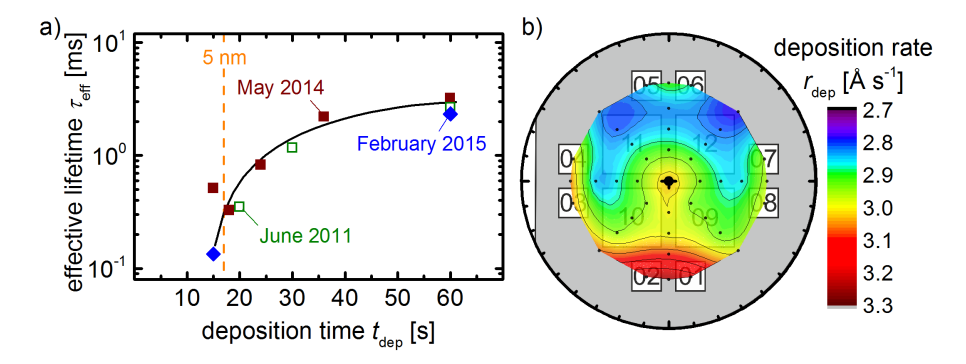


Figure 5.3.: a) The effective carrier lifetime (τ_{eff}) of (100) FZ Si wafers, which were symmetrically passivated by < i > a-SiO_x:H layers with varying deposition time (t_{dep}) . The dashed line indicates t_{dep} for a layer thickness of about 5 nm, typically used in SHJ solar cells. The depositions were performed at several points in time and the results from 2011 were taken from [112]. The line serves as a guide to the eye. b) Local deposition rate (r_{dep}) of < i > a-SiO_x:H layers with respect to the solar cell layout on the wafer, for a deposition at the rear side of the cells. The cell numbers are given in the background of the r_{dep} map. Black dots indicate the positions where the thickness of the a-SiO_x:H layer was measured on the glass substrate.

layer needed to be higher than for the front as $V_{\rm oc}$ was dominated by the rear side recombination. At the same time, the total d of the a-SiO_x:H had to be kept below 11 nm to achieve a high FF.

5.1.2. $\langle n \rangle$ nc-SiO_x:H emitter layers

Various <n> nc-SiO_x:H layers were applied as emitter layers in front-emitter SHJ solar cells. The structure of the solar cells was shown in Fig. 5.1 a) and the deposition conditions for the <math>nc-SiO_x:H layers were identical except for a variation of the CO₂ gas flow fraction (f_{CO₂}) for the emitter layer on the front of the solar cells. The impact of f_{CO₂} on the solar cell properties is presented in Fig. 5.5 and the correlation with the emitter layer properties is compiled in Fig. 5.6. FF of the solar cells was strongly affected by an increasing f_{CO₂} due to a decreasing amount of the nanocrystalline silicon (nc-Si) phase in the FSF layer. FF was reduced especially for

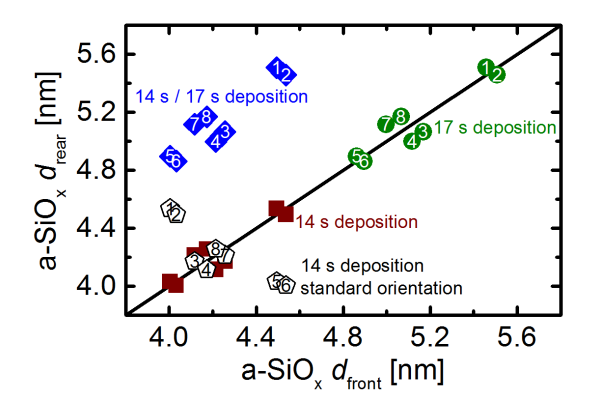


Figure 5.4.: Expected a-SiO_x:H layer thickness for different deposition times (t_{dep}) . The first number indicates the deposition time (t_{dep}) of the front layer and the second number t_{dep} of the a-SiO_x:H layer at the rear of the solar cell. The numbers inside the symbols indicate the cell number on each wafer. The wafers had to be turned in an appropriate way during the hot turning to consider the local r_{dep} of the a-SiO_x:H layers. The resulting layer thicknesses for a 14s deposition in standard orientation are included for comparison.

 $f_{\rm CO_2} > 20\%$, which marked the transition towards a Raman crystallinity $(I_{\rm c}) < 40\%$ and $\sigma_{\rm D} < 10^{-3}\,{\rm S\,cm^{-1}}$ (Fig. 5.6 a)). $V_{\rm oc}$ of the solar cells steadily decreased for increasing $f_{\rm CO_2}$ (Fig. 5.5 b)) due to a decrease of the free charge carrier density (Fig. 5.6 b)) in the emitter layer, which affected the built in voltage $(V_{\rm built})$ of the solar cells, which represents the upper limit of $V_{\rm oc}$. Accordingly, the implied open circuit voltage $(iV_{\rm oc})$ of the solar cells prior to the ITO deposition followed a similar trend. The differences between $V_{\rm oc}$ and $iV_{\rm oc}$ are probably related to the ITO deposition and the subsequent annealing of the solar cells, which might affect the properties of the nc-SiO_x:H layers as well as the a-SiO_x:H layers. The integrated short circuit current density from the EQE spectrum $(J_{\rm sc,DSR})$ of the SHJ solar cells was strongly influenced by the variation in $f_{\rm CO_2}$, which affected the amount of transparent a-SiO_x:H in the nc-SiO_x:H emitter layer. Accordingly, the initial increase can be attributed to an enhancement of E_{04} of the nc-SiO_x:H (Fig. 5.6 c)). In addition to E_{04} , n of the emitter layer changed and thereby affected the reflectance of the solar cell (Fig. 5.6 d)).

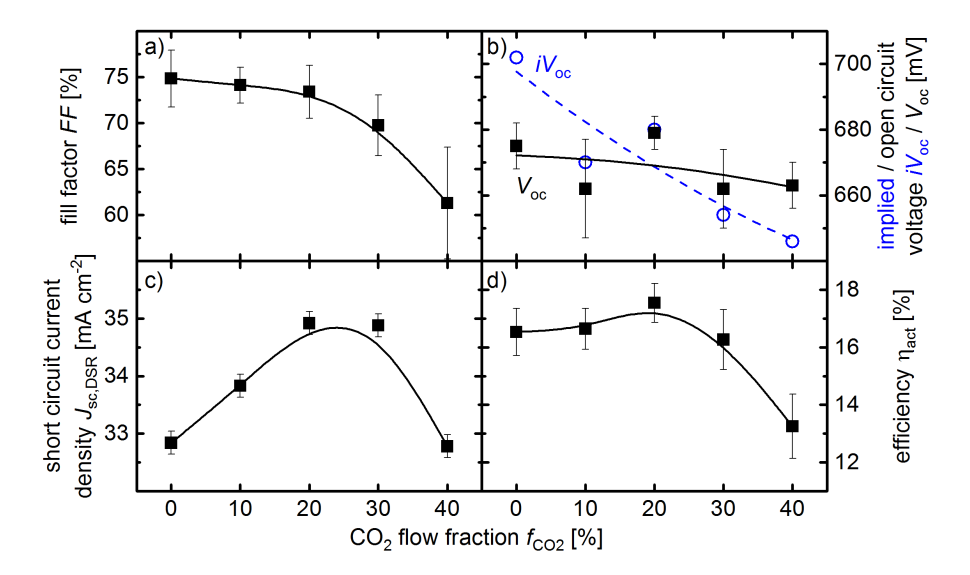


Figure 5.5.: a) Dependence of the mean fill factor (FF) on the CO_2 gas flow fraction (f_{CO_2}) of < n > nc-SiO_x:H emitter layers in a-SiO_x:H passivated SHJ solar cells on (100) Si wafers. The deposition range of the emitter layers extended from μc -Si:H to highly transparent nc-SiO_x:H with a high amount of O-rich a-SiO_x:H. b) Effect of the < n > nc-SiO_x:H layer on the implied open circuit voltage (iV_{oc}) and the mean open circuit voltage (V_{oc}). c)-d) Impact on the integrated short circuit current density from the EQE spectrum ($I_{sc,DSR}$) of cell 6 and the active area solar energy conversion efficiency (η_{act}). The added lines serve as a guide to the eye.

The detailed optical response of the solar cells is presented in Fig. 5.7. The internal quantum efficiency (IQE) was enhanced for $\lambda < 600\,\mathrm{nm}$ due to a reduced parasitic absorption with an increasing E_{04} of the <n>> nc-SiO_x:H emitter layer. At the highest E_{04} the IQE decreased in the short λ of light. This was probably due to an increased recombination at the front of the solar cell, which might be connected to a poor junction formation between the highly resistive emitter layer and the <p>> Si wafer. The lower concentration of charge carriers could have led to a larger space charge region in the nc-SiO_x:H, which had a high defect density, and an overall lower electrical field to separate generated charge carriers. For this cell, the EQE was reduced as well.

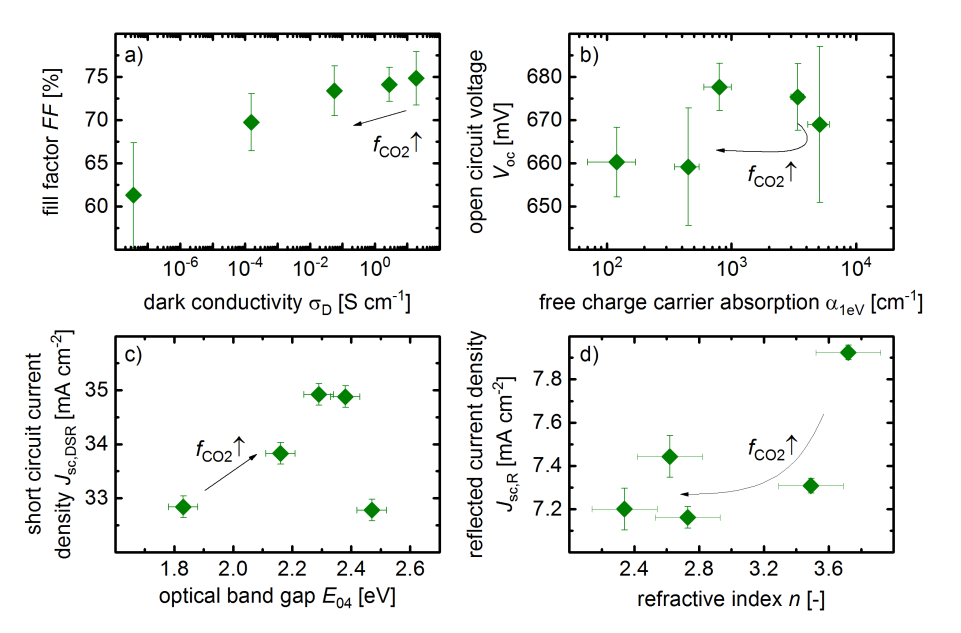


Figure 5.6.: a) Relation between the mean fill factor (FF) of the solar cells on each wafer and the electrical dark conductivity (σ_D) of the nc-SiO_x:H emitter layer. b) Effect of the sub-band gap absorption at a photon energy of 1 eV $(\alpha_{1\text{eV}})$ in the emitter layer, as a measure of the free charge carrier density, on the mean open circuit voltage (V_{oc}) of the front-emitter solar cells. c) Effect of the optical band gap (E_{04}) of the <n> nc-SiO_x:H on the integrated short circuit current density from the EQE spectrum $(J_{sc,DSR})$ of cell 6. d) The influence of n at $\lambda = 600\,\text{nm}$ of the emitter layer on J_R of the SHJ solar cells.

For the other cells, however, improvements in the IQE were not always accompanied by an increase in the $EQE/J_{\rm sc,DSR}$ because of a changing real part of the refractive index (n) of the emitter layer and the, thereby, altered R of the solar cells (Fig. 5.6 d)). Towards lower n the maximum in R was shifted to longer wavelengths of the spectrum. This was also evident in an increasing EQE of these solar cells with an increasing $f_{\rm CO_2}$ in the range of $600\,\mathrm{nm} < \lambda < 1000\,\mathrm{nm}$ (Fig. 5.7 a)). So, effectively, the short λ EQE was the product of two competing effects, the reduced parasitic absorption due to the enhanced E_{04} and an increased R due to the decreasing n with increasing $f_{\rm CO_2}$.

Overall, the highest η_{act} was achieved for the SHJ solar cells with a $\langle n \rangle$

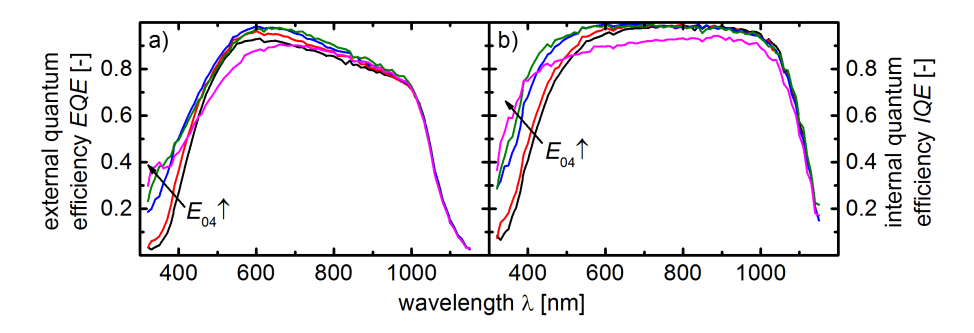


Figure 5.7.: Effect of varying the optical band gap (E_{04}) of the $\langle n \rangle$ nc-SiO_x:H emitter layer a) on the external quantum efficiency (EQE) and b) on the internal quantum efficiency (IQE) of front-emitter SHJ solar cells.

nc-SiO_x:H emitter layer deposited at $f_{\rm CO_2} = 20\%$ (Fig. 5.5 d)). This nc-SiO_x:H layer offered the best trade-off between high optical transparency and sufficient electrical conductivity with $E_{04} = 2.3\,{\rm eV}$ and $\sigma_{\rm D} = 0.1\,{\rm S\,cm^{-1}}$.

Further improvement of the solar cell performance could be achieved by increasing the heater temperature $(T_{\rm H})$ during the ITO deposition. For the application in SHJ solar cells an ideal transparent conductive oxide (TCO) exhibits a low electron density $(n_{\rm e})$ and a high charge carrier mobility (μ) to minimize the parasitic absorption of light due to free charge carriers and to provide a high electrical conductivity (σ) for a high FF, respectively [94, 96, 98]. A high μ has been reported for ITO layers deposited at a substrate temperature $(T_{\rm sub})$ of 125 °C by Hotovy et al. [163]. Therefore, ITO layers deposited at room temperature were compared to layers deposited at a $T_{\rm H}$ of 125 °C. An increased $T_{\rm H}$ during the ITO deposition resulted in a decrease of $n_{\rm e}$ by almost 50% (Fig. 5.8 a)). However, the simultaneous increase in the Hall electron mobility $(\mu_{\rm e})$ of the ITO by about 30% counteracted the decrease in $n_{\rm e}$. So, the overall σ only decreased by about 30%.

The J-V curves of the respective solar cells are presented in Fig. 5.8 a) and showed an increase in $J_{\rm sc}$ by about $0.5\,\mathrm{mA\,cm^{-2}}$ and even an increase in FF by 2% absolute. The increase in FF was surprising because the overall σ of the ITO layer decreased. However, the contact resistance towards the <p> nc-SiO_x:H layer might have been decreased due to a change in the work function of the ITO. The

reason for the increase in $J_{\rm sc}$ is evident from the EQE spectra in Fig. 5.8 b). On the one hand, the EQE slightly decreased in the short λ range below about 500 nm due to an apparent narrowing of the band gap of the ITO (Burstein-Moss effect [96]). On the other hand, the parasitic absorption of free charge carriers for $\lambda > 700$ nm decreased, as evident from the decrease of the difference between the 1-R and the EQE, which can be related to the reduced $n_{\rm e}$ [96, 98]. The difference in $V_{\rm oc}$ between the two cells, however, was not related to the ITO deposition. Instead, this difference could be attributed to small changes in the passivation quality because $iV_{\rm oc}$ of the solar cells was similar to the measured $V_{\rm oc}$ even before the ITO deposition for both cells. In total, an increased $\mu_{\rm e}$ and a reduced $n_{\rm e}$ of the ITO deposited at $T_{\rm H} = 125\,^{\circ}{\rm C}$ led to an increase of the active area solar energy conversion efficiency ($\eta_{\rm act}$) by 0.5% absolute, ultimately resulting in $V_{\rm oc} = 675\,{\rm mV}$, FF = 78.3%, and $J_{\rm sc,DSR} = 35.8\,{\rm mA\,cm}^2$ ($\eta_{\rm act} = 18.9\%$).

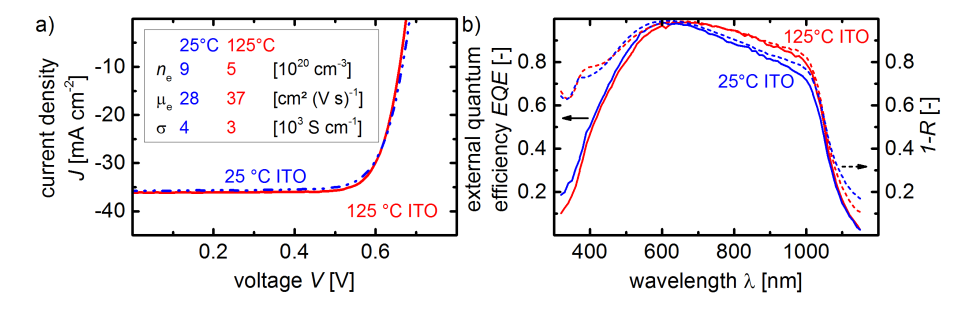


Figure 5.8.: a) J-V curves of SHJ solar cells with indium tin oxide (ITO) layers deposited at room temperature (RT) and at a heater temperature (T_H) of 125 °C. The electrical properties of the ITO layers, deposited on a glass substrate and characterized via HALL measurements, are summarized in the inset. Here, μ_e is the Hall electron mobility, n_e denotes the electron density, and σ the electrical conductivity. b) Comparison of the external quantum efficiency (EQE) and 1-reflectance (R) of the solar cells with different ITO layers.

5.1.3. Rear-emitter SHJ solar cells

In contrast to the commonly used $\langle p \rangle$ Si wafers for monocrystalline Si solar cells with diffused emitters, SHJ solar cells are often produced on $\langle n \rangle$ Si wafers. In fact, several advantages endorse the use of $\langle n \rangle$ Si wafers. First, the bulk carrier lifetime is usually higher in $\langle n \rangle$ wafers due to impurities like transition metals having a larger capture cross section for electrons than for holes, which are the minority charge carriers in $\langle n \rangle$ wafers [2]. Futhermore, under light exposure or high charge carrier injection the formation of B-O complexes leads to lower bulk carrier lifetimes, which is especially detrimental in Czochralski (CZ) $\langle p \rangle$ wafers [2]. Second, the capture cross section of defects at the wafer surface, mainly Si dangling bonds, is larger for electrons. This results in a lower implied fill factor (iFF) for $\langle p \rangle$ wafers due to an increased charge carrier recombination at low minority carrier densities [56, 57]. In total, higher $\tau_{\rm eff}$ and therefore increased $V_{\rm oc}$ and FF can be expected especially from CZ $\langle n \rangle$ Si wafers.

The use of <n> Si wafers for the solar cell design presented in Fig. 5.1 a) could easily be achieved by depositing the <p>nc-SiO_x:H on the front of the solar cell and placing the <n>nc-SiO_x:H at the rear. However, as was demonstrated in Sec. 4.3, <n>nc-SiO_x:H films usually show a better optoelectronic performance than <p>nc-SiO_x:H films. Therefore, to exploit the higher E_{04} of the <n>nc-SiO_x:H at the front and simultaneously employ <math><n>Si as the absorber, the solar cell design can be changed from a front- to a rear-emitter layout. Additionally, this layout has the advantage of transferring some of the lateral current from the TCO at the front to the Si absorber, enabling the use of a less conductive ITO at the front for an improvement in J_{sc} [164].

With respect to Fig. 5.1 a), switching to a rear-emitter layout was achieved by substituting the $\langle p \rangle$ Si wafer with an $\langle n \rangle$ wafer. In contrast to the front-emitter design, however, it was essential to define the cell area at the rear of the solar cell as well. Otherwise the full area at the rear is contributing to the dark saturation current density (J_0) of the solar cell, thereby deteriorating FF and $J_{\text{sc,DSR}}$ [56]. Therefore, the rear side of the cells was patterned by depositing the ITO and the Ag layer at the rear through the same shadow mask that was used for the ITO at the front. The solar cell parameters for SHJ solar cells with a-SiO_x:H passivation layers in a front-

and a rear-emitter design are summarized in Tab. 5.1. $V_{\rm oc}$ was slightly superior in the rear-emitter cells, probably due to the <n> absorber. At the same time, FF and $J_{\rm sc,DSR}$ were highly similar for both cell layouts. Altogether, the transition to a rear-emitter design allowed to exploit the benefits of an <n> Si wafer without sacrifices in FF or $J_{\rm sc,DSR}$ and even some additional opportunities for optimization as suggested in [164].

Table 5.1.: Solar cell parameters of a-SiO_x:H passivated SHJ solar cells in a rear- and a front-emitter design (mean values and standard deviation for 7 cells each).

emitter		absorber	FF	$V_{\rm oc}$	$J_{ m sc,DSR}$	η
$_{ m type}$	position		[%]	[mV]	$[\mathrm{mAcm^{-2}}]$	[%]
<n $>$ nc-SiO _x :H	front	(100)	73 ± 3	681 ± 4	35.8 ± 0.2	17.9 ± 1.0
$<\!\!\mathrm{p}\!\!>\mathrm{nc}\text{-}\mathrm{SiO}_{\mathrm{x}}\text{:}\mathrm{H}$	rear	<n>(111)</n>	73 ± 2	686 ± 4	35.7 ± 0.2	18.0 ± 0.7

5.2. a-Si:H passivated solar cells

Passivation layers of <i>a-Si:H are the most commonly used passivation scheme for SHJ solar cells. Their exceptional passivation quality has been demonstrated by a $V_{\rm oc}$ of 750 mV in a heterojunction with intrinsic thin layer (HIT®) solar cell on a 98 μ m <n>Si wafer by Sanyo/Panasonic [9]. There are two common approaches to maximize the passivation quality of a-Si:H passivated crystalline silicon (c-Si) interfaces. The first is by H₂ plasma treatment [76,77], also called "chemical annealing" [147]. The second method is thermal annealing, typically at temperatures around 200 °C [69,165]. The latter will be covered in the first part of this section. Explicitly, this part briefly outlines the development of <i>a-Si:H passivation layers on polished wafers. The second part of the section then covers the application of <i>a-Si:H in rear-emitter SHJ solar cells with nc-SiO_x:H FSF and emitter layers. Furthermore, the optical response of these solar cells is modeled by using OPAL 2 in the third part.

5.2.1. Passivating crystalline Si wafers with $\langle i \rangle$ a-Si:H

 $\tau_{\rm eff}$ at an excess charge carrier density of $10^{15} {\rm cm}^{-3}$ and the Fourier transform infrared spectroscopy (FTIR) spectra of <i> a-Si:H passivation layers, deposited at varying heater temperature $(T_{\rm H})$ and H_2 gas flow fraction $(f_{\rm H_2})$, are presented in Fig. 5.9. After deposition, thermal annealing at 220 °C was performed in air for annealing times (t_a) up to 100h. First of all, $f_{\rm H_2}$ was optimized at a $T_{\rm H}$ of 200°C (Fig. 5.9 a)). The bonding arrangement within the a-Si:H films in the as-deposited state was analyzed via FTIR (Fig. 5.9 b), c)). Starting at a SiH₄ plasma without additional H_2 , $\tau_{\rm eff}$ in the as-deposited state was very low and the (Si₃)Si-H bending ((b)) mode around 650 cm⁻¹ as well as the (Si₃)Si-H stretching ((s)) mode around 2000 cm⁻¹ indicated a high amount of H in the films. Furthermore, a distinct shoulder was evident at a wavenumber $\nu \approx 2090\,\mathrm{cm}^{-1}$, which points at a void rich a-Si:H film [119]. H that is contained in these voids can easily be rearranged [69,73]. Accordingly, upon annealing $\tau_{\rm eff}$ of wafers passivated with these a-Si:H layers increased from about 200 μ s beyond 1 ms. This change in $\tau_{\rm eff}$ is related to a reduction of the dangling bond density [69] by mobile H and a transfer of the (Si₃)Si-H (s) mode around $2090\,\mathrm{cm}^{-1}$ towards the (Si₃)Si-H (s) mode at $\nu = 2000\,\mathrm{cm}^{-1}$, which represents the transition to a more dense structure of the a-Si:H film [69,73]. A similar effect can be achieved in the as-deposited state by increasing $f_{\rm H_2}$ (Fig. 5.9 c)) as evident from a decreasing number of voids and a lower hydrogen content (c_H) within the films. Accordingly, $\tau_{\rm eff}$ of Si wafers with a-Si:H layers increases with increasing $f_{\rm H_2}$ (Fig. 5.9 a)) and an even higher $\tau_{\rm eff}$ could be achieved by annealing. At the highest $f_{\rm H_2}$, however, $\tau_{\rm eff}$ only slightly improved with longer $t_{\rm a}$ and even decreased from about 3 h on. This is an indication for partial epitaxial growth of Si at the a-Si:H/wafer interface [75, 165].

The overall highest $\tau_{\rm eff}$ in the annealed state was achieved with $f_{\rm H_2} = 90\,\%$, which was then used to optimize $T_{\rm H}$ (Fig. 5.9 d), e), f)). An increasing $T_{\rm H}$ had a similar effect on $\tau_{\rm eff}$ in the as-deposited state as an increase of $f_{\rm H_2}$. For low $T_{\rm H}$ a low initial $\tau_{\rm eff}$ was observed in combination with a high $\tau_{\rm eff}$ after annealing. However, for a $T_{\rm H}$ of 290 °C $\tau_{\rm eff}$ was lowered in the initial state in comparison to $T_{\rm H} = 260\,$ °C and subsequent annealing only resulted in a further decrease of $\tau_{\rm eff}$. Similarly to a high $f_{\rm H_2}$, the decrease in $\tau_{\rm eff}$ at a high $T_{\rm H}$ can be related to epitaxial growth

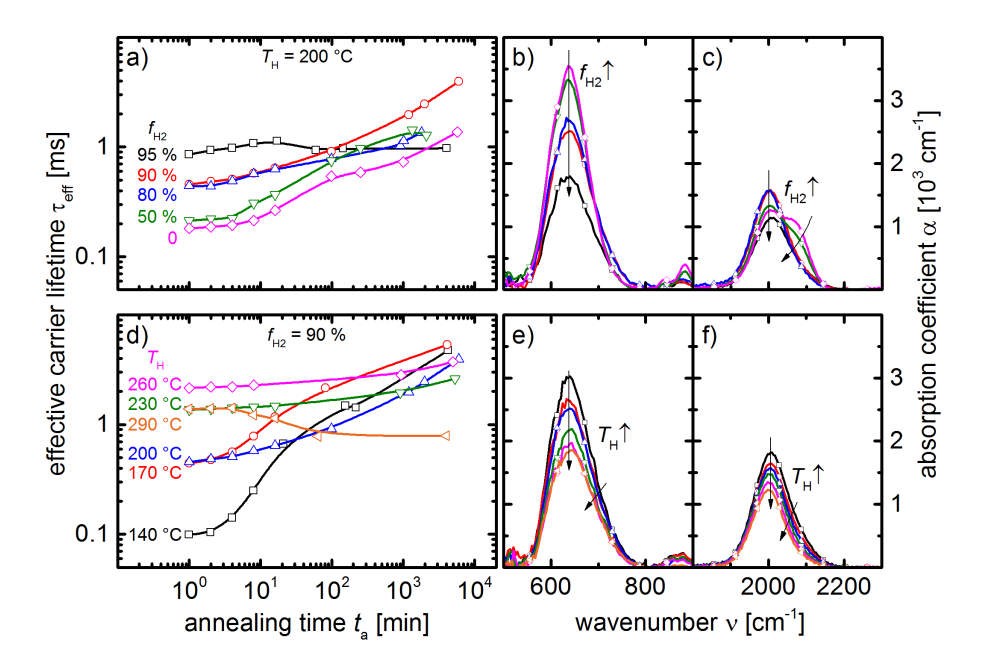


Figure 5.9.: a) Evolution of the effective carrier lifetime (τ_{eff}) at an excess charge carrier density of $10^{15}\,\mathrm{cm}^{-3}$ for polished < n > (111) wafers (280 $\mu\mathrm{m}$, 30 cm) passivated with 5 nm of < i > a-Si:H on both sides. The a-Si:H depositions were performed at various H_2 gas flow fractions (f_{H_2}) with a constant total gas flow of 100 sccm. Afterwards, the samples were annealed at 220 °C in air. The lines are a guide to the eye. b) FTIR spectra of < i > a-Si:H layers in the range of the Si-H (b) mode. The layers were deposited on a Si substrate at the same deposition conditions as the layers in a) with a thickness of $100-300\,\mathrm{nm}$. c) FTIR spectra in the range of the (Si₃)Si-H (s) modes for a variation of f_{H_2} . d) Effect of t_a on τ_{eff} of < n > (111) wafers passivated with < i > a-Si:H layers deposited at a different heater temperature (T_H). e) Effect of T_H on the FTIR spectra of < i > a-Si:H films in the Si-H (b) region. f) FTIR spectra in the (Si₃)Si-H (s) region for a variation of T_H .

of Si at the a-Si:H/c-Si interface [74], which can be controlled by adjusting $f_{\rm H_2}$, $T_{\rm H}$, deposition power (P), and deposition pressure (p) [74]. Correspondingly, the total $c_{\rm H}$ decreased towards increasing $T_{\rm H}$ and the (Si₃)Si-H (s) mode shifted towards 2000 cm⁻¹ (Fig. 5.9 e), f)). In fact, similar values for the absorption coefficient (α) of the (Si₃)Si-H (s) mode as well as the (Si₃)Si-H (b) mode were observed for both

samples series around the transition towards epitaxially grown Si. Therefore, the FTIR spectra of the passivation layers might be useful to identify the proximity of the deposition regime to the region of epitaxial growth, which is detrimental to the passivation properties.

Overall, high $\tau_{\rm eff}$ could be achieved by depositing the $\langle i \rangle$ a-Si:H at low $T_{\rm H}$ in a state of high $c_{\rm H}$, far from the region of epitaxial growth, in combination with a long t_a. Following the deposition of the a-Si:H passivation layers, harsh processing conditions can damage the a-Si:H/c-Si interface and diminish $\tau_{\rm eff}$ (see also Sec. 6.2.1). Conversely, a-Si:H layers prepared in the presented manner were suited to withstand the deposition conditions for the subsequent doped nc-SiO_x:H layers on polished wafer substrates. However, the oxide, which formed during the annealing, might present a strong barrier to the charge carrier transport in a solar cell and has, therefore, to be removed prior to depositing subsequent layers. Commonly, hydrofluoric acid (HF) is used to remove the native oxide from Si wafer surfaces. Furthermore, it was reported to result in a surface recombination velocity (S) of 0.25 cm s⁻¹ at the surface of (111) oriented wafers by nearly perfect termination of dangling bonds with H [166]. This would correspond to a "surface lifetime" of about 18×10^3 ms for a Si wafer with $d = 280 \,\mu\text{m}$ (Eq. 6.3). Therefore, HF could be expected to enhance or at least preserve $\tau_{\rm eff}$ if used to remove the post-annealing oxide for the $\langle i \rangle$ a-Si:H passivated wafers. In fact, similar $\tau_{\rm eff}$ were achieved on each half of a passivated wafer with and without an HF-dip after depositing <n> and $\langle p \rangle$ nc-SiO_x:H.

5.2.2. $\langle n \rangle$ nc-SiO_x:H front surface field layers

Following the development of the <i>a-Si:H passivation layers, they were applied in rear-emitter SHJ solar cells. The processing sequence is similar to the one depicted in Fig. 3.1, with the exception that <n>(111) Si wafers were used. After the deposition of 5 nm of <i>a-Si:H, the wafers were thermally annealed between 40 and 90 h to achieve a high $\tau_{\rm eff}$ and then dipped in 1% HF for 2 min prior to the deposition of the <n>nc-SiO_x:H front surface field (FSF) and the <p>nc-SiO_x:H emitter layer. The total layer stack is depicted in Fig. 5.10.

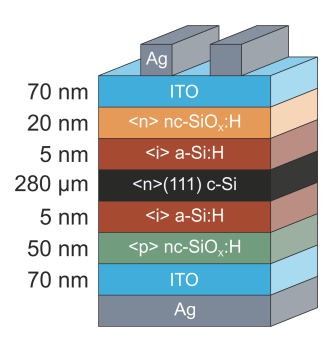


Figure 5.10.: Layer stack of the intrinsic (<i>) hydrogenated amorphous silicon (a-Si:H) passivated rear-emitter SHJ solar cells with varying n-type doped (<n>) nc-SiO_x:H front surface field (FSF) layers. A polished <n> float-zone (FZ) Si wafer in (111) orientation and with a nominal resistivity of $1-5\Omega$ cm was used as the substrate.

The solar cell parameters of the best cells on each processed wafer with different <n> nc-SiO_x:H FSF layers are presented in Fig. 5.11. Furthermore, the best cells of the nc-SiO_x:H emitter layer variation of the front-emitter a-SiO_x:H passivated SHJ solar cells are added for comparison (see also Sec. 5.1.2). Except for the passivation layers, the same sequence of layers with the same thicknesses were used for both series of cells. By varying $f_{\rm CO_2}$ during the deposition, E_{04} of the FSF layer was adjusted. According to investigations on a-SiO_x:H passivation layers, the change in E_{04} should mainly affect the valence band offset $(\Delta E_{\rm V})$ of the nc-SiO_x:H FSF layer [61]. This would increase the transport barrier for holes at the interface between the nc-SiO_x:H and the passivation layer. In the investigated configuration of the rear-emitter solar cells an increase in $\Delta E_{\rm V}$ would not affect the electronic transport due to holes being repelled by the $\langle n \rangle$ FSF layer towards the absorber. Still, FFof the solar cells decreased for an increasing E_{04} of the FSF layer (Fig. 5.11 a)). This was the result of an overall decreasing σ_D of the FSF layer due to a decreasing fraction of nc-Si, which affects the amount of active dopants in the overall film. At very high $f_{\rm CO_2}/E_{04}$ this can result in a negative space charge region being induced in the nc-SiO_x:H layer in contact to the ITO and the <n> absorber [167]. This would essentially lead to an n/n⁺ diode in reverse to the p/n junction and produce an S-shaped I-V curve, as observed for the highest E_{04} of the FSF layer with FF = 12%. Furthermore, iFF and the pseudo fill factor (pFF) of the solar cells are compared

to FF in Fig. 5.12 b). Independently of the applied FSF layer a high iFF prior to the ITO deposition and a high pFF for the complete solar cell were observed. This indicates that the reduced FF is purely a result of an increasing $R_{\rm s}$, which is related to the decreasing $I_{\rm c}$.

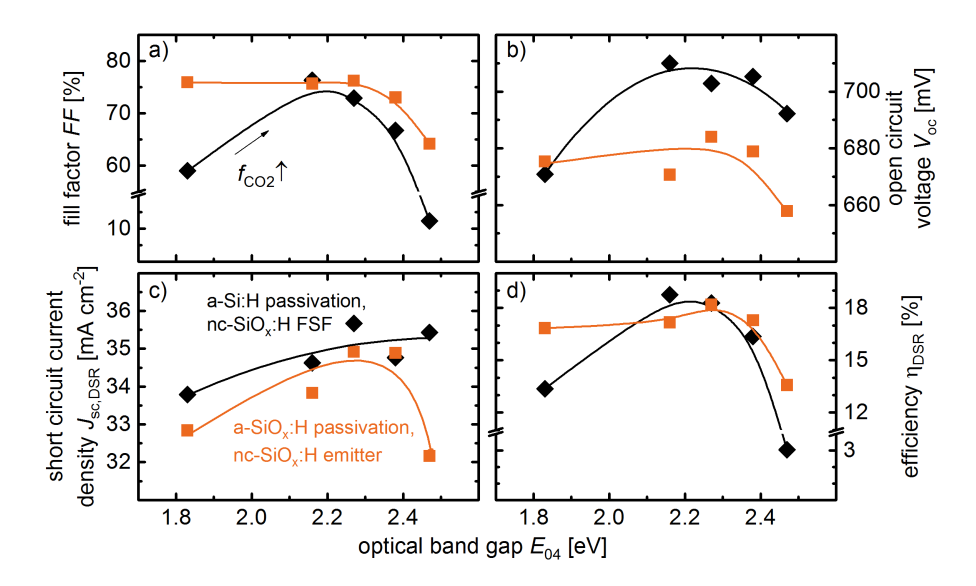


Figure 5.11.: Effect of changing E_{04} of the < n > nc-SiO $_x$: H front surface field (FSF) layer for a-Si:H passivated rear-emitter SHJ solar cells (black diamonds). The properties of the FSF layers were adjusted by changing f_{CO_2} similar to the variation in Fig. 5.5. Interdependence of E_{04} of the FSF layer and a) the fill factor (FF), b) the open circuit voltage (V_{oc}), c) the integrated short circuit current density from the EQE spectrum ($J_{sc,DSR}$), and d) the solar energy conversion efficiency (η) of the best solar cells on each wafer. The ITO layers of the a-Si:H passivated solar cells were deposited at $T_H = 125\,^{\circ}\mathrm{C}$. The best cells of the nc-SiO $_x$:H emitter layer variation for the a-SiO $_x$:H passivated front-emitter SHJ solar cells (Fig. 5.5) are added for comparison (orange squares). The lines serve as a guide to the eye.

A notable exception is the μ c-Si:H FSF layer, deposited at $f_{\rm CO_2}=0$ with $E_{04}\approx 1.8\,{\rm eV}$ and $I_{\rm c}\approx 80\%$ for a 400 nm thick layer deposited on a glass substrate. Here, a low FF indicates a highly resistive FSF layer in contrast to the high $I_{\rm c}$. In literature, layers of 20 nm μ c-Si:H with a high $\sigma_{\rm D}$ have been deposited on glass

substrates, while the same deposition conditions resulted in fully amorphous films when grown on a-Si:H layers [158]. The poor nucleation of nc-Si on a-Si:H substrates has also been reported in [91, 139, 156, 168]. To facilitate the crystallite growth, a short CO₂ plasma treatment step can be applied to the a-Si:H substrate [25,91,158]. Similarly, the low FF for the μ c-Si:H FSF layer grown on the $\langle i \rangle$ a-Si:H layer could be explained by an inhibited nucleation of the nc-Si phase. Contrary, for passivation layers of <i> a-SiO_x:H, which should be similar to the a-Si:H films subjected to the CO_2 plasma, nucleation of nc-Si could still take place and a high FF was achieved. This poor nucleation even affected V_{oc} of the solar cells, including iV_{oc} (Fig. 5.12 a)). Accordingly, the contribution of the FSF layer to the passivation of the front surface via field effect also decreased due to the lowly doped a-Si:H FSF layer. However, a small addition of CO₂ at $f_{\text{CO}_2} = 10\%$ led to an increase in FF as well as V_{oc} indicating an improved nucleation. This might stem from a surface treatment of the a-Si:H passivation layer similarly to a CO₂ plasma treatment. At the same time, it might indicate a different nucleation mechanism of the nc-Si phase during the deposition of nc-SiO_x:H as compared to μ c-Si:H films. The reduced incubation layer thickness reported for nc-SiO_x:H on glass substrates in comparison to μ c-Si:H films would support the latter statement [109]. Additionally, transmission electron microscopy (TEM) images have indicated the nc-Si to exist in a globulitic fashion in nc-SiO_x:H [22, 24] in contrast to a cone-like growth in μ c-Si:H films [157].

In addition to FF, the reduction in $I_{\rm c}$ also affected $V_{\rm oc}$ (Fig. 5.11 b)) due to a decrease of the free charge carrier density, as discussed in Sec. 5.1.2 for the front-emitter cells. Furthermore, $J_{\rm sc,DSR}$ was increased by the decrease in parasitic absorption due to an increase in E_{04} of the FSF layer. The overall η of the solar cells, however, was dominated by the influence of the FSF layer on FF (Fig. 5.11 d)).

Comparing the a-Si:H passivated rear-emitter solar cells and the a-SiO_x:H passivated front-emitter solar cells in Fig. 5.11, all a-SiO_x:H passivated solar cells showed an enhanced FF, which might be related to an improved nucleation of nc-Si on the a-SiO_x:H layers. However, $V_{\rm oc}$ of the a-Si:H passivated cells is up to 40 mV higher than for the a-SiO_x:H passivated cells for any given nc-SiO_x:H FSF layer, which can mainly be attributed to the superior passivation quality provided by the <i> a-Si:H. A minor contribution might also stem from the different doping types

of the Si wafers, as higher $\tau_{\rm eff}$ are expected for <n> wafers as compared to (see also Sec. 5.1.3). The improvement in $J_{\rm sc,DSR}$ for the a-Si:H passivated solar cells is mainly due to the application of the higher $\mu_{\rm e}$ ITO layers (see also Sec. 5.1.2), which resulted in reduced parasitic absorption in the range of $\lambda > 800\,\rm nm$. Due to a similar layer stack being employed, the effect of the FSF layer variation on the EQE and the IQE was highly similar to the emitter layer variation in Fig. 5.7, except for the improved response in the infrared due to the different ITO. However, a white bias light of about 0.1 sun had to be applied to the a-Si:H passivated solar cells with the FSF layer deposited at $f_{\rm CO_2} = 0$ and 40% to achieve full charge carrier extraction.

In summary, the best performance for the <i>a-Si:H passivated rear-emitter solar cell was achieved with a similar nc-SiO_x:H FSF layer as for the emitter layer of the a-SiO_x:H passivated solar cells in Sec. 5.1.2. Optically similar results were observed for both solar cell designs. However, nucleation of nc-Si may be affected by the a-Si:H passivation layers and can lead to a lower σ of the FSF layer, thereby reducing FF of the solar cell. Nevertheless, passivation layers of <i>a-Si:H can be considered superior to <i>a-SiO_x:H due to a significant improvement of the surface passivation and thereby $V_{\rm oc}$ by about 20 mV.

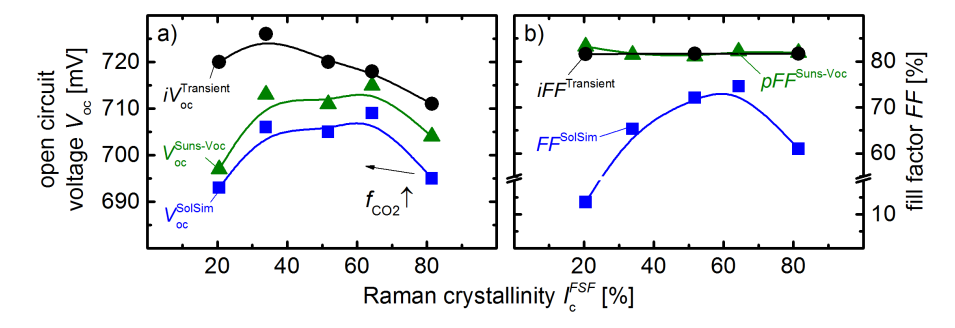


Figure 5.12.: Variation of the Raman crystallinity (I_c) in the < n > nc-SiO_x:H FSF layer in the a-Si:H passivated rear-emitter SHJ solar cells. a) Relation between I_c of the < n > nc-SiO_x:H and the implied open circuit voltage (iV_{oc}) determined from photoconductance lifetime testing (PLT) and V_{oc} measured via the Suns-Voc stage and the solar simulator. b) Interdependence of I_c with the implied fill factor (iFF) from PLT, the pseudo fill factor (pFF) from Suns-Voc, and the real FF from the solar simulator measurements. The lines serve as a quide to the eye.

5.2.3. OPAL 2 simulations of the front layer stack

So far, the solar cell properties were related to the $nc-SiO_x$:H layer properties of thick films, deposited on glass, while the deposited layers in the solar cells were only a few tens of nm thick and deposited on an a-Si:H passivated surface. To investigate whether the optical properties of the solar cell can be adequately described by the determined film properties, optical simulations with a freeware program for the optical analysis of the front surface of a solar cell (OPAL 2) were performed. A limiting factor to these simulations is that they only consider the front of the solar cell as described in Sec. 3.3. Therefore, they can only be used to investigate the reflectance losses of the solar cells and the parasitic absorptance (A_{paras}) in the front layer stacks in a λ range in which the incident light is fully absorbed during the first passage through the absorber material.

Figure 5.13 and 5.14 summarize the results of the optical simulations of the <i> a-Si:H passivated rear-emitter SHJ solar cells with <n> nc-SiO_x:H FSF layers and a nc-SiO_x:H emitter layer. The effect of varying the nc-SiO_x:H FSF layer on the R spectra of the solar cells is evaluated in Fig. 5.13. The experimental data in a) shows a shift of the R minimum towards higher λ with a decreasing n of the FSF layer. At the same time, R around $\lambda = 400 \,\mathrm{nm}$ was strongly affected by the high n of a-Si:H and c-Si in this λ range and, thereby, by the phase composition within the nc-SiO_x:H FSF layer. The simulated spectra in Fig. 5.13 b) replicate the changes in R accurately. To achieve a good resemblance of the experimental results the thicknesses of the ITO and the nc-SiO_x:H FSF layer had to be slightly adjusted in a range of 65-69 nm and 17-20 nm, respectively, for each solar cell. This variation of the thicknesses is well within the range of the error margin during the deposition due to minor changes in the deposition rates of the films. In contrast, fixing the thicknesses at the nominal values of 70 nm and 20 nm resulted in a poor fit to the experimental data as exemplified by the position of the absorptance (A) maximum in Fig. 5.13 c). With slightly adjusted thicknesses, however, a good fit was achieved.

Ideally, the A maximum (R minimum) of a planar solar cell should be engineered towards the maximum of the solar irradiance spectrum around $\lambda = 600 \,\mathrm{nm}$. This is also evident from the current density loss due to reflexion (J_{R}) in Fig. 5.13 d), which represents a convolution of the AM1.5G spectrum with the R spectrum of

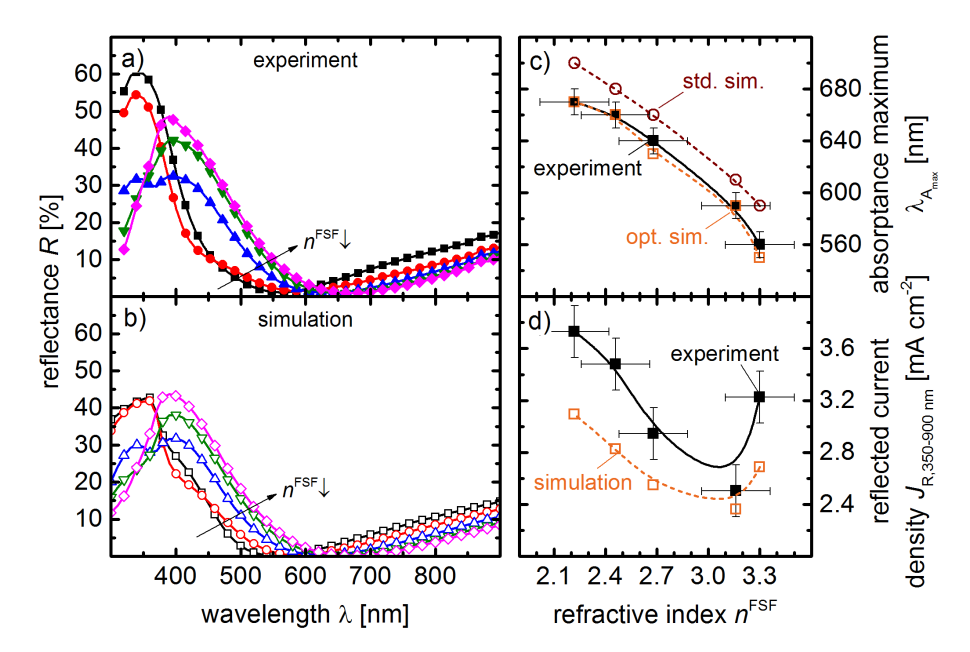


Figure 5.13.: OPAL 2 simulations of the <i>a-Si:H passivated rear-emitter SHJ solar cells with varying the <n>nc-SiO_x:H front surface field (FSF). a) Measured reflectance (R) of the grid-less cells on each wafer (cell 6). b) Simulated R of the front layer cell stack with varying the real part of the refractive index (n) of the nc-SiO_x:H FSF layer. c) Position of the absorption maximum in the R spectra with changing n of the FSF layer. The experimental results are compared to two sets of simulated results. The first ("std. sim.") used fixed ITO and nc-SiO_x:H thicknesses at 70 nm and 20 nm, respectively, while the second ("opt. sim.") allowed for a variation of the thicknesses in 65-69 nm and 17-20 nm, respectively. d) The current density loss due to reflexion (J_R) in 350 \leq $\lambda \leq$ 900 nm for the experimental and the simulated results in dependence on n of the FSF layer. The added lines serve as a guide to the eye.

the solar cells in $350 \le \lambda \le 900$ nm. Again, a good correlation is found between the simulated and the experimental data and the trends due to a changing n of the FSF layer are well reproduced. The offset between the simulated and the experimental data can be explained by an offset in the minimal value of R. While all the simulated spectra reached R = 0 at some λ , the minimum R for the experimental spectra was around 1%, which lies within the accuracy of the measurement setup of 1%.

This offset of 1% would result in a J_R of about $0.33\,\mathrm{mA\,cm^{-2}}$ for $350 \le \lambda \le 900\,\mathrm{nm}$, corresponding well to the observed offset in J_R in Fig. 5.13 d).

In addition to the R spectra, the transmittance (T) through the front layer stack can be considered as an approximation of the EQE of the solar cell. However, this is only valid for light at wavelengths, which get predominantly absorbed in the wafer during the first passage. Here, $\lambda = 900\,\mathrm{nm}$ was chosen as the critical wavelength of single passage because for the smallest Si absorber thickness used in this work $(170\,\mu\mathrm{m})$ only about $0.6\,\%$ of the transmitted light would reach the rear of the absorber at this λ . This was estimated by using the Lambert-Beer law and $\alpha = 303\,\mathrm{cm}^{-1}$ of $\langle i \rangle$ Si at $\lambda = 900\,\mathrm{nm}$ [169]. The simulated "EQE" is compared to the real EQE in Fig. 5.14 a). Overall, the experimental EQE spectra were well reproduced by the simulation even up to about $\lambda = 980\,\mathrm{nm}$ due to the thick Si absorber (280 $\mu\mathrm{m}$). Beyond this value, the light exited the solar cell after being reflected at the rear of the solar cell and passing it a second time. Contrary, in the simulation an infinite Si absorber is assumed to follow the front layer stack, producing a high EQE beyond $\lambda = 1000\,\mathrm{nm}$ in Fig. 5.14 a).

Furthermore, noticeable differences between the simulated and the experimental spectra were evident for $\lambda < 450\,\mathrm{nm}$, especially for solar cells with a nc-SiO_x:H FSF layer with a high E_{04} . This was also reflected in an overestimated $A_{\rm paras}$ in the front layer stack by the simulation as shown in Fig. 5.14 b). Here, the experimental A_{paras} was approximated by the difference between A and the EQE. Therefore, A_{paras} includes absorbed light that does not create electron/hole pairs, as well as loss of generated charge carriers due to recombination. The overestimated $A_{\rm paras}$ by the simulation might be a result of different layer properties between the several hundred nm thick samples deposited on glass, which provided the input data for the simulation, to the 20 nm thick layers deposited on <i> a-Si:H in the solar cell. As was shown in Sec. 4.3, $c_{\rm O}$ of the nc-SiO_x:H increases towards a lower layer d, while I_c decreases due to the existence of an incubation layer [109, 159]. As a consequence of the increased $c_{\rm O}$, this incubation layer can be expected to have a higher $E_{\rm 04}$ than the reference film deposited on glass. Therefore, $A_{\rm paras}$ by the 20 nm thick nc-SiO_x:H layer is less in the solar cell as compared to the simulation. This effect seemed to increase as $f_{\rm CO_2}$ during the deposition of the nc-SiO_x:H was increased (higher E_{04}

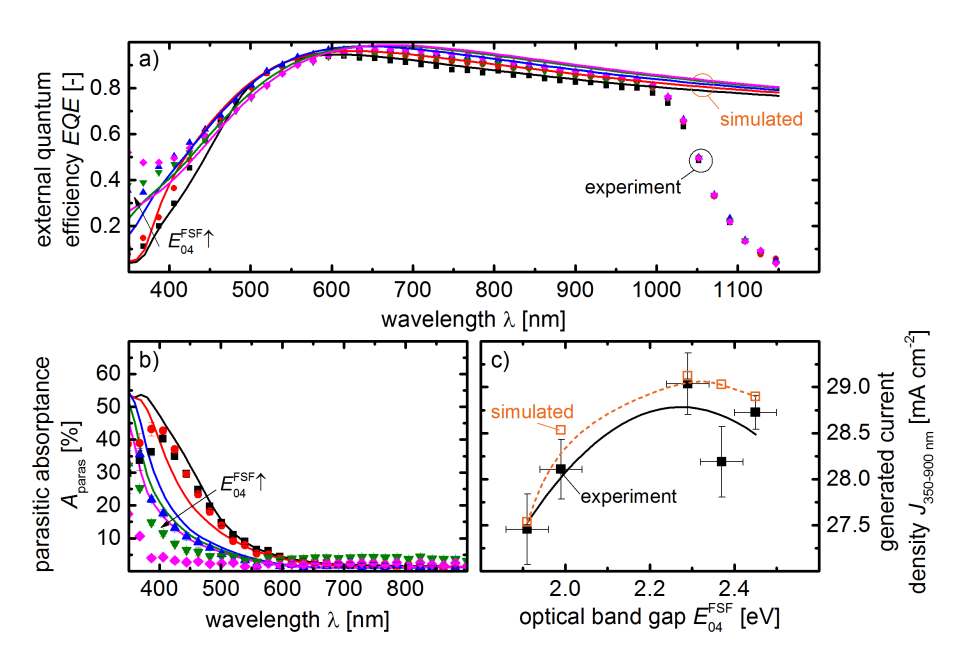


Figure 5.14.: a) Experimental EQE spectra and simulated transmittance (T) through the front layer stack of the $\langle i \rangle$ a-Si:H passivated rear-emitter SHJ solar cells with varying the $\langle n \rangle$ nc-SiO_x:H front surface field (FSF). b) Simulated and experimental spectra of the parasitic absorptance (A_{paras}) for varying nc-SiO_x:H FSF layers. c) Generated current density in the solar cells in $350 \leq \lambda \leq 900\,\mathrm{nm}$ in relation to E₀₄ of the FSF layer. The lines serve as a guide to the eye.

FSF layer). For the FSF layer deposited at $f_{\rm CO_2}=10\%$ (red curve in Fig. 5.14 b)) $A_{\rm paras}$ is underestimated probably due to an increased amount of a-Si:H instead of nc-Si in the 20 nm layer as compared to the highly crystalline 350 nm thick film on glass. However, the parasitic absorption of the μ c-Si:H FSF layer is surprisingly low if one assumes a much more amorphous structure due to the deposition on the a-Si:H passivation layer as compared to the crystalline film on glass. Nevertheless, Fig. 5.14 c) shows a good agreement between the generated current density in the range of $350 \le \lambda \le 900\,\mathrm{nm}$ for the simulations and the experimental EQE spectra. The slight overestimation by the simulated current density is likely due to the decreased R as compared to the experimental R spectra, which resulted in a slight

increase of the EQE in the long λ range.

Overall, the calculated R, T (EQE) and A_{paras} were well suited to reproduce the changes in the optical properties of the rear-emitter solar cells due to the variation of the $nc-SiO_x$:H FSF layer. Therefore, OPAL 2 simulations represent a fast and reasonably accurate method to predict and optimize the layer stack at the front of the SHJ solar cells. Especially, when combined with the favorable n of the $nc-SiO_x$:H layers for AR purposes. Additionally, the simulations support the results in Sec. 4.3, which indicated an O-rich incubation layer with a low I_c in the $nc-SiO_x$:H films towards the substrate. Here, this was shown to result in a stronger reduction of A_{paras} with increasing E_{04} than expected from the material data acquired from thicker $nc-SiO_x$:H films. This also infers that σ_D of the 20 nm layers are likely lower than for the thick films, which is probably partly compensated by the anisotropic growth of the nc-Si phase (see also Sec. 4.2.1).

5.3. Nano-imprint lithography for anti-reflection coatings

The previous sections established nc-SiO_x:H emitter layers and FSF layers as an effective way to reduce $A_{\rm paras}$ at the front of SHJ solar cells. However, to fully utilize the optical benefits of the nc-SiO_x:H the light incoupling into the planar solar cells has to be increased. Here, nano-imprint lithography (NIL) excels at providing countless possible textures to enhance the incoupling of light at the front [107,170] or provide light trapping at the rear [171–173] of a solar cell. Especially, the amount of recombination active area is not increased as compared to direct texturing of the Si wafer. Furthermore, this approach is suitable to substitute wet-chemical texturing for ultra-thin or multi-crystalline Si absorbers. In the following, a Si random pyramid textured anti-reflection (AR) coating was applied to planar rear-emitter SHJ solar cells to enhance the light incoupling and assess the interplay with various nc-SiO_x:H FSF layers.

Figure 5.15 a) shows the layer stack of the investigated SHJ solar cells. As depicted there, the NIL step was applied subsequently to the fabrication of the solar

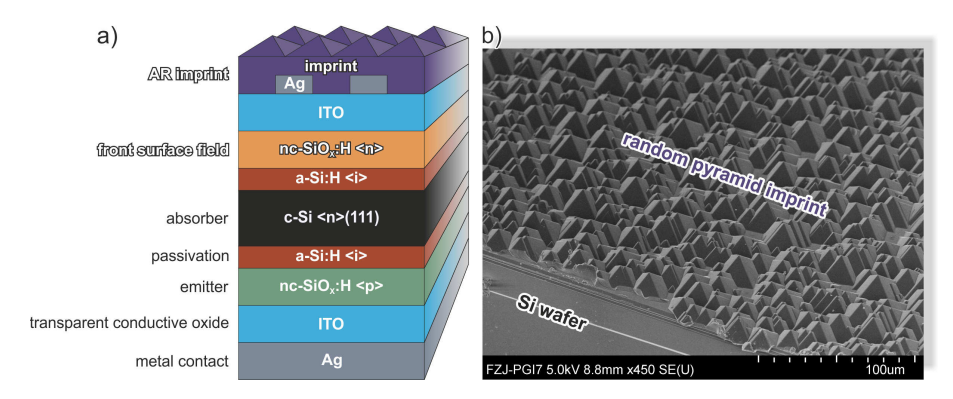


Figure 5.15.: a) Schematic structure of a rear-emitter SHJ solar cell with a Si random pyramid texture anti-reflection (AR) coating applied via nano-imprint lithography (NIL). The layer thicknesses are not to scale and are the same as in Fig. 5.1 except for the <i>a-Si:H passivation layers, which are 5 nm thick. b) SEM image of the NIL AR layer on a polished Si substrate.

cells and covered the Ag grid of the solar cell as well. Only above the contacting pads small openings were carefully scratched into the AR layers to electrically contact the solar cells. OrmoComp® from "micro resist technology GmbH" was used as the imprint resin. In the cured state its optical properties are close to silicon dioxide (SiO₂) with $n \approx 1.5$. A wet-chemically textured Si wafer was used as the master structure and the random pyramid texture was well reproduced with nearly perfect coverage and smooth facets. Figure 5.15 b) demonstrates the high quality of the transferred texture.

The effect on R of the solar cell is shown in Fig. 5.16. The planar solar cells displayed a high total reflectance (TR) that mainly stemmed from specular reflectance (SR) with a diffuse reflectance (DR) below 5%. By applying the AR imprint layer, TR was strongly reduced across the full λ range and the main mode of reflection was DR due to scattering of the incoming light at the pyramid surfaces. SR was reduced below 5% across most of the spectrum and the remaining part is probably related to a small planar fraction within the AR imprint, which can also be seen in Fig. 5.15 b). Overall, the Si random pyramid textured AR imprint drastically reduced R of the solar cell. The changes in EQE of a planar solar cell due to the AR layer are displayed in Fig. 5.17 a). Most of the gain in A (as

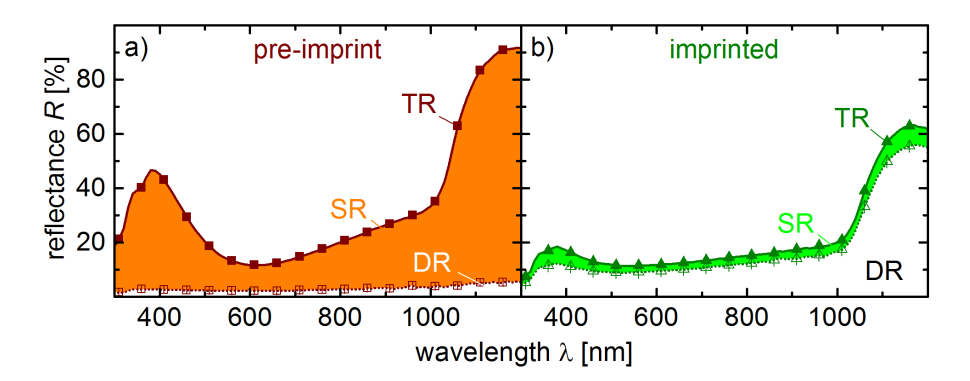


Figure 5.16: a) The total reflectance (TR) (full symbols) and diffuse reflectance (DR) (open symbols) of a planar SHJ solar cell in a spectral range of $300-1200\,\mathrm{nm}$. The difference between TR and DR represents the specular reflectance (SR) (colored area). The measurements were done in an aperture area configuration including the front Ag grid. b) TR, DR, and SR of a SHJ solar cell with a Si random pyramid texture anti-reflection (AR) imprint.

1-R) is transferred to an increase in the EQE across the full spectrum. Albeit, the EQE around the A maximum of the bare solar cell is slightly reduced. This is because the planar layer stack provided a nearly ideal AR at a specific λ due to destructive interference of the incoming light, whereas the AR imprint disrupts this interference by the random pyramid texture. Nevertheless, a net gain of about $2\,\mathrm{mA\,cm^{-2}}$ was achieved by applying the AR imprint. Furthermore, the IQE of the solar cell (Fig. 5.17 b)) was hardly affected by the AR imprint, demonstrating the high transparency of this layer. A slight decrease in the IQE was only detected for $\lambda > 1000\,\mathrm{nm}$, which is attributed to an increased length of the light path through the front ITO layer and a thereby increased A_{paras} due to free charge carriers (see also Sec. 5.1.2). In contrast, the light path enhancement in the ITO at the rear of the solar cell is expected to be negligible as the gradual increase of n from the imprint surface towards the Si absorber led to a gradual redirection of the light ray path towards the geometric normal of the layer stack.

In a next step, the rear-emitter SHJ solar cells with varying nc-SiO_x:H FSF layers from Sec. 5.2.2 were investigated in combination with the AR imprint. The

5. Planar silicon heterojunction solar cells

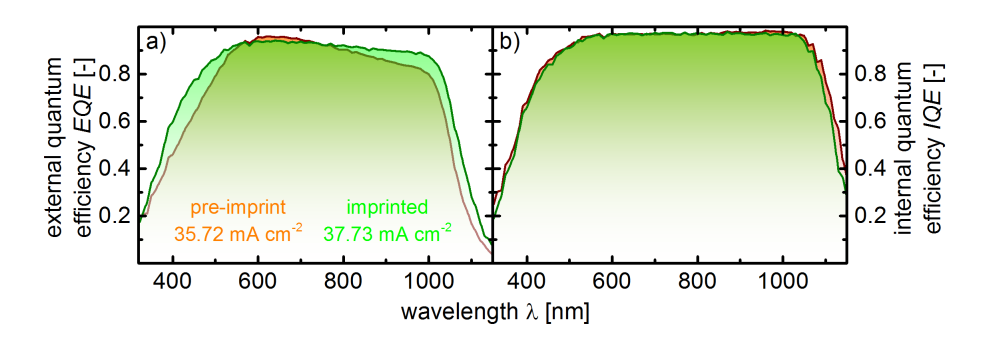


Figure 5.17.: a) EQE of a planar SHJ solar cell in a spectral range of $320-1150\,\mathrm{nm}$ before (orange) and after (green) applying a Si random pyramid texture anti-reflection (AR) imprint. b) IQE in the pre- and the post-imprint state.

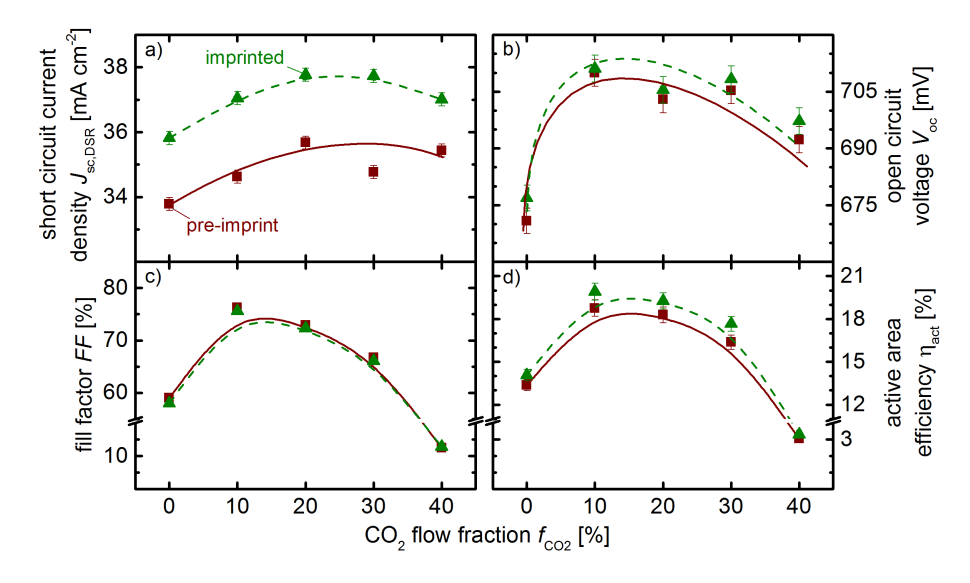


Figure 5.18.: a) $J_{sc,DSR}$, b) V_{oc} , c) FF, and d) η_{act} of rear-emitter SHJ solar cells with varying < n > nc-SiO_x:H FSF layers (see also Sec. 5.2.2) before and after applying a Si random pyramid texture anti-reflection (AR) imprint. The points represent the cell parameters of the best cell for each FSF layer within the series. The added lines are a guide to the eye.

resulting solar cell parameters are presented in Fig. 5.18. Here, a gain of up to 3mAcm⁻² was observed depending on the FSF layer of the solar cell. This corresponds to an average increase of about 6% in the active area $J_{\rm sc}$ for each cell. The aperture area $J_{\rm sc}$ of the solar cell was enhanced even more with about 7% as determined by DSR. This could be attributed to light that is reflected from the grid towards the surface of the imprint and then partially reflected back towards active areas of the solar cell. Furthermore, $V_{\rm oc}$ of the solar cells increased by a few mV due to the enhanced photocurrent. An increase of $J_{\rm sc}$ from about $35\,{\rm mA\,cm^{-2}}$ to $37 \,\mathrm{mA\,cm^{-2}}$ would result in an increase of V_{oc} by about 1.4 mV [174], which is within the measurement error, but could still be observed for all cells. FF of the solar cells was maintained with only minor losses of about 0.5% absolute (Fig. 5.18 c)), which might be due to a slightly increased voltage loss by R_s due to the enhanced current at the maximum power point (mpp). However, the effect of the AR imprint on FFand $V_{\rm oc}$ was minute in comparison to its effect on $J_{\rm sc,DSR}$. In total, an increase in $\eta_{\rm act}$ by over 1% absolute was achieved by the Si random pyramid AR imprints for cells which are not limited by a poor FF.

The detailed optical response of each solar cell is presented in Fig. 5.19. $f_{\rm CO_2}$ during the deposition of the <n> nc-SiO_x:H FSF layer was increased from the top to the bottom figures and led to an increase of E_{04} from 1.8 to 2.5 eV and a reduction of n at $\lambda = 600 \, \mathrm{nm}$ from 3.7 to 2.3. The AR imprint led to an increase of A beyond 80 % for $\lambda < 1000 \,\mathrm{nm}$ for all of the cells due to the enhanced light incoupling. Thereby, very similar A spectra were achieved for all cells, in contrast to the strong variation in A for the solar cells without the AR imprint. Consequently, the AR imprint mitigated the effect of a shift in the A spectra on the EQE. The amount of A_{paras} in the FSF layer then determined how effectively the increase in A was transferred to an increase in the EQE (Fig. 5.19 f)-j)). For the cells with a FSF layer of $E_{04} < 2.3\,\mathrm{eV}$ only a small gain in the EQE was observed in the short λ range, even though A was increased significantly. Albeit, a FSF layer with $E_{04} > 2.2 \,\mathrm{eV}$ granted an improved enhancement of the EQE in $400\,\mathrm{nm} < \lambda < 600\,\mathrm{nm}$. However, part of the gain in the short λ range is due to a shift in the A maximum of the pre-imprint solar cell (see also Fig. 5.13). In the cell without an imprint layer, a lower n of the FSF layer led to a shift of the A spectrum towards longer λ . With the AR imprint, however, this shift in the A spectrum was equalized. Therefore, the gain in the

5. Planar silicon heterojunction solar cells

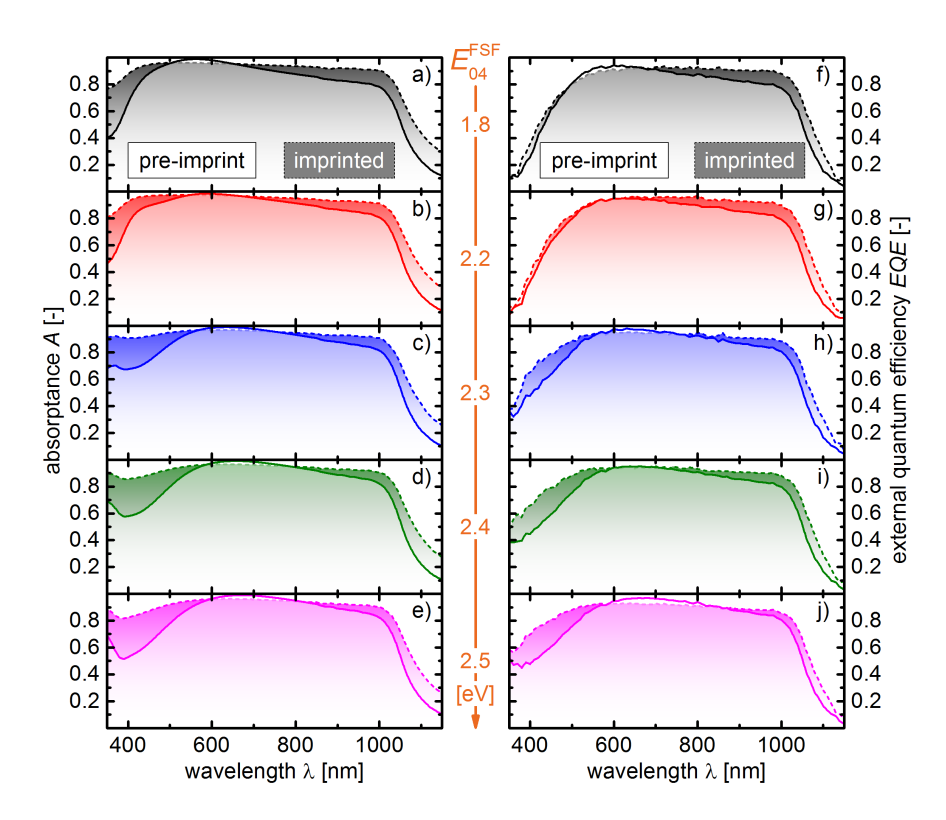


Figure 5.19.: a)-e) A spectra of rear-emitter SHJ solar cells with varying $\langle n \rangle$ nc-SiO_x:H FSF layers without (light, full) and with (dark, dashed) a Si random pyramid texture anti-reflection (AR) imprint. The optical band gap (E₀₄) of the nc-SiO_x:H FSF layer is increasing from a) to e). f)-j) EQE spectra of the solar cells in a spectral range of $350-1150\,\mathrm{nm}$.

EQE due to the AR imprint increased in the short λ range with a decreasing n of the nc-SiO_x:H FSF layer, while it gradually decreased in the long λ range.

All in all, a significant enhancement of $J_{\rm sc}$ was achieved by the application of a Si random pyramid AR imprint layer at the front of the planar solar cells. Meanwhile, FF and $V_{\rm oc}$ were maintained. The optical benefit from the improved light incoupling was strongly affected by the optical properties of the applied nc-SiO_x:H FSF layer in the SHJ solar cells. Here, the AR imprint also provided a way to diminish the shift in the A spectrum with varying optical properties of the FSF layer of the planar

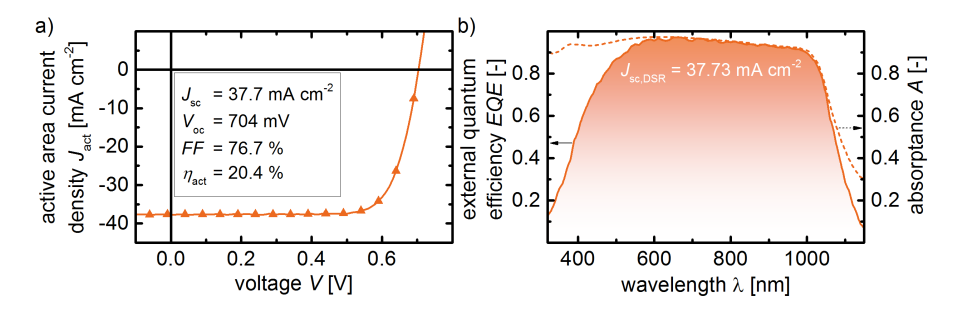


Figure 5.20.: a) J-V curve and cell parameters of the best rear-emitter SHJ solar cell with a $\langle n \rangle$ nc-SiO_x:H FSF layer and a NIL Si random pyramid texture AR imprint. The FSF layer was deposited at $f_{CO_2} = 20 \,\%$, resulting in $E_{04} = 2.3 \,\mathrm{eV}$ and $\sigma_D = 0.1 \,\mathrm{S\,cm^{-1}}$. b) EQE and A spectra of the best solar cell with an AR imprint.

layer stack. The performance of the best <i> a-Si:H passivated planar rear-emitter SHJ solar cell with an AR imprint produced in this work is presented in Fig. 5.20. A high $V_{\rm oc}$ due to the optimized a-Si:H passivation layers was paired with a high $J_{\rm sc}$ by applying a transparent nc-SiO_x:H FSF layer in combination with the improved light incoupling due to the AR imprint. In total, this resulted in a $\eta_{\rm act}$ of 20.4%. A of the cell was kept above 90% up to $\lambda=1000\,{\rm nm}$ with an IQE close to unity from 600 to 1000 nm. Ultimately, yielding a high $J_{\rm sc,DSR}$ of 37.7 mA cm⁻² in a planar SHJ solar cell. This corresponded to an aperture area $J_{\rm sc}$ of about 35.7 mA cm⁻² and an aperture area solar energy conversion efficiency $(\eta_{\rm ap})$ of 19.3%.

Surface texturing is a common and industrially applied technique to enhance the optical properties of a solar cell. For crystalline silicon (c-Si) based solar cells Si wafers in (100)-orientation are, typically, wet-chemically textured in solutions of potassium hydroxide (KOH), sodium hydroxide (NaOH) or tetramethylammonium hydroxide (TMAH) with isopropyl alcohol (IPA). Thereby, the wafer surface is anisotropically etched, so that the resulting surface is mainly comprised of (111)-oriented facets [175]. These facets generate randomly distributed and randomly sized pyramids on the wafer surface with a characteristic angle of 54.74° for purely (111)-oriented facets [134]. Depending on the applied etchant and the processing parameters, the pyramid size distribution and the fraction of planar area can be varied [175-177]. On the one hand, textured solar cells offer a significantly higher solar energy conversion efficiency in comparison to planar solar cells due to an increased light incoupling in combination with efficient light trapping, both of which result in an increase in the short circuit current density (J_{sc}) of the solar cell. On the other hand, the surface area is enlarged which leads to an enhanced recombination of generated charge carriers at the surface of the solar cell absorber.

This chapter covers the results on textured silicon heterojunction (SHJ) solar cells with doped hydrogenated nanocrystalline silicon oxide (nc-SiO_x:H) layers. The first section describes the passivation of textured wafer surfaces with intrinsic ($\langle i \rangle$) hydrogenated amorphous silicon (a-Si:H) layers and relates them to the results on planar wafer surfaces. The second part comprises the successful implementation of nc-SiO_x:H layers in textured SHJ solar cells and a comparison to current literature data. Furthermore, it includes simulations of varying surface textures to

further minimize optical losses in the textured solar cells. Lastly, a short investigation on the stability of the best performing SHJ solar cell with nc-SiO $_x$:H layers during storage and under extended light exposure is presented in the third section.

6.1. a-Si:H passivation for textured solar cells

The wafers used in this study were bought as-textured using a KOH solution, producing a Si random pyramid texture (Fig. 6.2 b)). As implied earlier, the increased surface area and changes in the surface morphology as a consequence of the wafer texturing, may lead to changes in the passivation quality. Accordingly, the achieved effective carrier lifetime ($\tau_{\rm eff}$) on a textured wafer surface can be expected to vary from the results obtained on a polished wafer substrate.

To investigate these differences in detail, the heater temperature $(T_{\rm H})$ variation during the deposition of <i> a-Si:H layers from Sec. 5.2.1 was repeated on the textured Si wafers and the results are presented in Fig. 6.1 a). However, the deposition time $(t_{\rm dep})$ had to be increased by a factor of 1.7 to account for the angle of the pyramid facets and to achieve the same thickness (d) orthogonally to the pyramid surface as on the planar substrate [57,178]. Overall, the dependence of $\tau_{\rm eff}$ on $T_{\rm H}$ in the as-deposited state is very similar to the results on the polished substrates. Although, the achieved $\tau_{\rm eff}$ in the as-deposited as well as the annealed state were significantly lower than on the polished wafers. This can be attributed to an increase in the surface area and will be discussed in more detail in a later paragraph.

Nevertheless, similarly to the results in Sec. 5.2.1, an increase in $T_{\rm H}$ led to an increasing $\tau_{\rm eff}$, which was strongly enhanced by annealing, especially for wafers utilizing a-Si:H layers deposited at low $T_{\rm H}$ and, thereby, with a high hydrogen content $(c_{\rm H})$. However, $\tau_{\rm eff}$ in the as-deposited state decreased at $T_{\rm H}=260\,^{\circ}{\rm C}$ already in contrast to $T_{\rm H}=290\,^{\circ}{\rm C}$ for the polished wafers. Similarly, a decrease in $\tau_{\rm eff}$ after about 1h of annealing was observed for $T_{\rm H}\geq 200\,^{\circ}{\rm C}$, which only occurred at a higher $T_{\rm H}$ of 290 °C on the planar (111)-oriented substrates. The decrease in $\tau_{\rm eff}$ with increasing annealing time $(t_{\rm a})$ and at high $T_{\rm H}$ in the as-deposited state, can be explained by epitaxial growth of Si (see also Sec.5.2.1) [179]. For textured wafers the onset of epitaxial growth was evidently lower than for the polished (111)-oriented

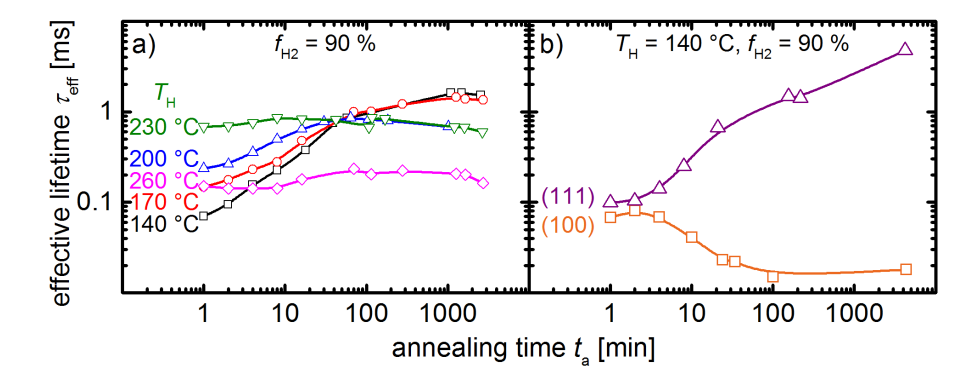


Figure 6.1.: a) Effect of varied heater temperatures (T_H) and annealing times (t_a) on the effective carrier lifetime $(\tau_{\rm eff})$ at an excess charge carrier density of $10^{15}\,{\rm cm^{-3}}$ for textured < n > (100) wafers $(FZ, 280\,\mu{\rm m}, 3\Omega\,{\rm cm})$ passivated with 5 nm of < i > a-Si:H on both sides. The a-Si:H was deposited at a f_{H_2} of 90%. The samples were annealed at 220°C in air and they were briefly taken out in between to determine $\tau_{\rm eff}$. b) Annealing results on a planar (111)- and a (100)-oriented Si wafer $(FZ, 280\,\mu{\rm m}, 3\Omega\,{\rm cm})$ with 5 nm of < i > a-Si:H deposited at $T_H = 140\,{\rm ^{\circ}C}$ on both sides. The added lines serve as a guide to the eye.

substrates, despite the surface of the textured wafers being mainly comprised of (111)-oriented pyramid facets. However, at the pyramid edges and grooves the atomic environment of a Si atom deviates from the ideal (111)-surface, resulting in a different bonding configuration and stress. Accordingly, epitaxial growth of Si has been predominantly observed at the edges and grooves of the Si pyramids and was related to stress induced defects [91,180,181].

The effect of epitaxial growth on the annealing behavior of a-Si:H passivation layers can also be demonstrated on planar substrates. A solely (111)-oriented surface can be well passivated by a-Si:H. In contrast, (100) surfaces typically yield a lower passivation quality for a a-Si:H layers [77] and are more prone to epitaxial growth of Si [181]. This is exemplified in Fig. 6.1 b) by a deposition of $\langle i \rangle$ a-Si:H on a (111)- and a (100)-oriented polished Si wafer. While a $\tau_{\rm eff}$ of about 5 ms was achieved on the (111)-oriented substrate, the same deposition conditions and annealing treatment resulted in a poor passivation of the (100)-oriented wafer, even though similar $\tau_{\rm eff}$ were observed in the as-deposited state. After a few minutes of annealing

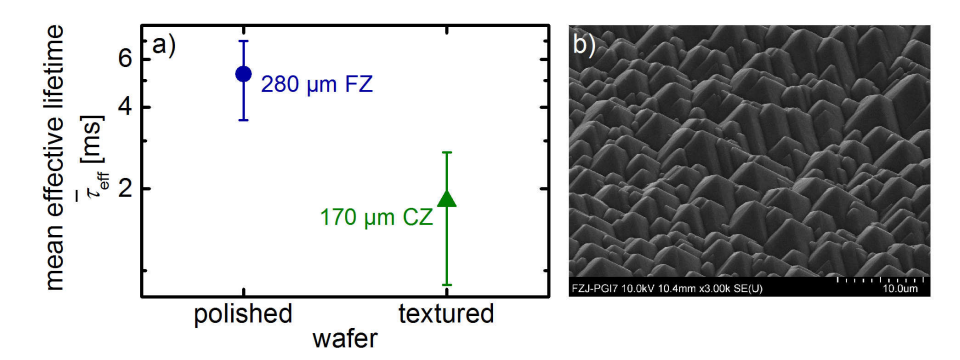


Figure 6.2.: a) Mean effective carrier lifetime (τ_{eff}) achieved by 5 nm of <i> a-Si:H layers on polished (111)-oriented Si wafers (FZ, 280 µm, 3Ω cm) and on wet-chemically textured (100)-oriented Si wafers (CZ, 170 µm, 3Ω cm). τ_{eff} of 14 planar and 11 textured wafers were statistically evaluated and the error bars represent the standard deviation of τ_{eff} . The a-Si:H layers were deposited at $T_H = 140$ °C and $f_{H_2} = 90$ % and each sample was annealed for 40-70 h. b) SEM image of the textured wafer surface.

 $au_{\rm eff}$ decreased with increasing $t_{\rm a}$ similarly to wafers passivated with a-Si:H that was deposited in the regime of epitaxial growth (high $T_{\rm H}$ or $f_{\rm H_2}$). On the Si pyramid textured surface, epitaxial growth was observed at lower $T_{\rm H}$ as compared to a planar (111) wafer. Nevertheless, at a $T_{\rm H}$ of 140°C the deposition regime was sufficiently far away from the a-Si:H/c-Si transition region and no epitaxial growth of Si on the textured wafer was evident from the annealing behavior (Fig. 6.1 a)). Consequently, a high quality a-Si:H passivation on textured wafers could be achieved in the same way as for the polished wafers, at $T_{\rm H}=140\,^{\circ}{\rm C}$ in combination with extended annealing.

The thus obtained $\tau_{\rm eff}$ is compared for the two different substrates in Fig. 6.2 a). The mean $\tau_{\rm eff}$ for the textured wafers, symmetrically passivated with <i> a-Si:H, was reduced to about a third of $\tau_{\rm eff}$ of polished wafers.

In general, $\tau_{\rm eff}$ of a passivated substrate can be divided into a bulk and a surface component

$$\frac{1}{\tau_{\text{eff}}} = \frac{1}{\tau_{\text{bulk}}} + \frac{1}{\tau_{\text{surface}}}.$$
 (6.1)

For a symmetrically passivated sample with an equal surface recombination velocity

(S) at the front and the rear surface, the surface component of $\tau_{\rm eff}$ can be expressed as [182]

$$\tau_{\text{surface}} = \frac{d}{2S} + \frac{1}{D} \left(\frac{d}{\pi}\right)^2. \tag{6.2}$$

Here, D denotes the charge carrier diffusion coefficient and d the wafer thickness. D is typically in the range of 10-30 cm² s⁻¹ [182]. Consequently, the first term of Eq. 6.2 dominates τ_{surface} as long as S is smaller than about $100 \, \text{cm s}^{-1}$, which is readily achieved by $\langle i \rangle$ a-Si:H layers [183, 184]. Accordingly, τ_{surface} can be simplified to

$$\tau_{\text{surface}} = \frac{d}{2S},\tag{6.3}$$

An increase in the surface area would result in a proportional increase in S according to [101, 180]

$$S_{\text{text}} = S_{\text{plan}} \frac{A_{\text{text}}}{A_{\text{plan}}}.$$
 (6.4)

In combination with Eq. 6.3 and assuming that $\tau_{\text{bulk}} \gg \tau_{\text{surface}}$, this leads to

$$\tau_{\text{eff,text}} = \frac{d_{\text{text}}}{2 S_{\text{plan}}} \frac{A_{\text{plan}}}{A_{\text{text}}}$$
(6.5)

for the textured wafer, and to

$$\tau_{\rm eff,plan} = \frac{d_{\rm plan}}{2 S_{\rm plan}} \tag{6.6}$$

for the planar reference. Finally, combining Eq. 6.5 and 6.6, a comparison of $\tau_{\rm eff}$ for both wafers can be made, considering the effect of the surface area enhancement and the different wafer d

$$\tau_{\text{eff,text}} = \tau_{\text{eff,plan}} \frac{d_{\text{text}}}{d_{\text{plan}}} \frac{A_{\text{plan}}}{A_{\text{text}}}.$$
(6.7)

The surface area enhancement factor is $\sqrt{3} \approx 1.73$ for an ideal Si pyramid surface texture [180]. With this, a simple estimation via Eq. 6.7 gives $\tau_{\rm eff,text} \approx 0.35\,\tau_{\rm eff,plan}$. So, the determined mean $\tau_{\rm eff}$ of 5.29 ms on polished wafers would correspond to $\tau_{\rm eff} = 1.86\,\rm ms$ on the textured wafer, which relates well to the observed mean $\tau_{\rm eff}$ of 1.80 ms in Fig. 6.2 a). Therefore, the reduced $\tau_{\rm eff}$ for the textured substrates can be mainly attributed to the enlarged surface area and the reduced d of the wafer. In contrast, epitaxial growth of Si does not seem to have a significant effect on $\tau_{\rm eff}$ of the textured wafers for the given deposition conditions in combination with the thermal annealing treatment.

6.2. nc-SiO_x:H in textured SHJ solar cells

After a passivation scheme had been established for the textured Si wafers, <n> and <p>nc-SiO_x:H layers were used to produce high performance SHJ solar cells. In detail, this section covers the results for a textured SHJ solar cell with a nc-SiO_x:H emitter and front surface field (FSF) layer. Furthermore, the distinct features of the solar cell are highlighted and a comparison to similar SHJ solar cells in literature is made to determine opportunities for future development. In the last part of this section OPAL 2 is used to investigate the potential for an optical optimization of the wafer texture by inverted pyramids.

6.2.1. Successful implementation of nc-SiO_x:H

The implementation of the nc-SiO_x:H layers, developed at very high frequency (VHF) in Sec. 4, turned out to damage the <i> a-Si:H passivation layers. Especially due to the deposition of the <n> nc-SiO_x:H, $\tau_{\rm eff}$ was reduced from a few milliseconds to below 100 µs even for <i> a-Si:H passivation layers as thick as 15 nm. The main reason for this is believed to lie in the high $f_{\rm H_2}$ in combination with the VHF deposition process, both of which contribute to a high density of atomic H, which has been ascribed to an enhanced etching of the growing film [135,136]. Furthermore, the existence of a growth zone that extends more than 10 nm into an underlying a-Si:H layer has been proposed [185]. Within this region the a-Si:H is transformed by interactions with particles from the plasma. Similarly, a deterioration of the a-Si:H passivation layers has also been reported during the deposition of doped hydrogenated microcrystalline silicon (µc-Si:H) layers in SHJ solar cells by Mazzarella et al. [91].

Unfortunately, the very same conditions that enable a high optoelectronic performance of $\operatorname{nc-SiO}_x$:H films by reducing the amount of the a-Si:H phase in favor of O-rich hydrogenated amorphous silicon oxide (a-SiO_x:H) and nanocrystalline silicon (nc-Si) seem to affect an underlying a-Si:H passivation layer as well, which imposes additional restrictions on the development of high performance $\operatorname{nc-SiO}_x$:H films. Surprisingly, the a-Si:H passivation layers were only harmed by the $\operatorname{nc-SiO}_x$:H deposition on textured wafers, while no evidence of severe damage to the passiva-

tion layers was found on planar substrates. Accordingly, the surface geometry might result in weak points within the deposited a-Si:H film at the edges and valleys of the pyramids, so that they are more prone to etching than their counterparts deposited on flat substrates. Consequently, the surface texture should have an impact on the etching of the passivation layer.

Another solution for the etching issue was found in switching to similar $\operatorname{nc-SiO}_x$:H layers deposited at a different plasma enhanced chemical vapor deposition (PECVD) system ("6K system"). Here, the $\operatorname{nc-SiO}_x$:H layers had been developed at a lower H₂ flow (200 sccm instead of 500 sccm) and at radio frequency (RF) [32]. The "softer" deposition conditions for these layers were reflected in a fourfold increase in the deposition rate ($r_{\rm dep}$) as compared to the best performing $\operatorname{nc-SiO}_x$:H layers from Sec. 5.2. Nevertheless, they exhibited similar optoelectronic properties and are expected to yield a similar performance in the SHJ solar cells.

The layer stack of the SHJ solar cells on the textured wafers is presented in Fig. 6.3 a). In comparison to the cells in Sec. 5, the deposition times had to be adjusted (×1.7) to ensure a sufficient coverage of the Si pyramid facets in the direction of their normal vector. The solar cell parameters and the J-V curve of the best SHJ solar cell are shown in Fig. 6.3 b). For a total cell area of $4\,\mathrm{cm}^2$ an active area solar energy conversion efficiency ($\eta_{\rm act}$) of 21.4% was achieved with an active area current density ($J_{\rm act}$) of $39.4\,\mathrm{mA\,cm}^{-2}$.

The development of the presented SHJ solar cell is combining various technological aspects to provide the presented solar energy conversion efficiency (η) . The gradual implementation of these features can be discussed via the evolution of the best performing solar cells in this study. These are summarized in Fig. 6.4. Starting at a a-SiO_x:H passivated front-emitter solar cell with $\eta=18.9\%$, a significant improvement of the open circuit voltage $(V_{\rm oc})$ was achieved by substituting a-SiO_x:H with a-Si:H. Furthermore, a rear-emitter design was employed to replace the <p>absorber by a <n> Si wafer and still be able to benefit from the higher optoelectronic performance of <n> nc-SiO_x:H. With this, the external quantum efficiency (EQE) and reflectance (R) of the solar cell were only slightly changed by an increase of R in the short wavelength (λ) range, leading to a decrease in the EQE, which was partially offset by an increase of the EQE in the long λ range (Fig. 6.4 b)).

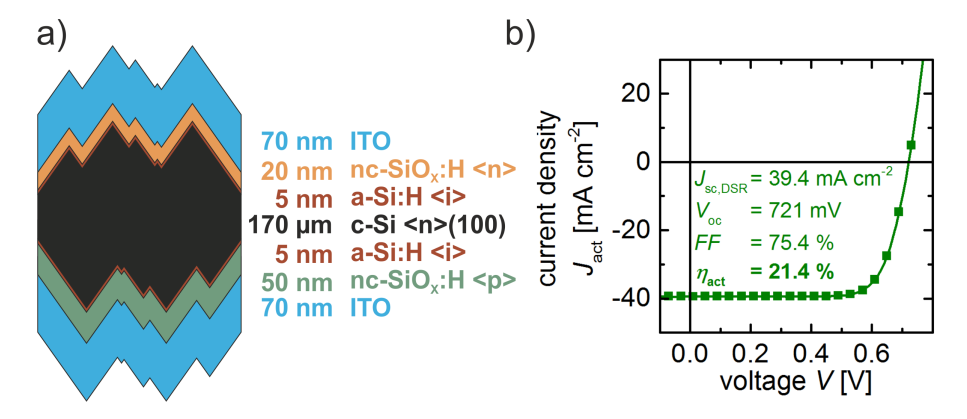


Figure 6.3.: a) Layer stack of the $\langle i \rangle$ a-Si:H passivated SHJ solar cell on a Si random pyramid textured wafer with a $\langle p \rangle$ nc-SiO_x:H emitter layer and a $\langle n \rangle$ nc-SiO_x:H FSF layer. All the deposition times were multiplied by 1.7 with respect to the planar solar cells. b) J-V curve of the best performing $2x2\,\mathrm{cm}^2$ SHJ solar cell. The current density was rescaled to an active area current density (J_{act}) to match the integrated short circuit current density from the EQE spectrum $(J_{Sc.DSR})$.

In the next step, $J_{\rm sc}$ of the solar cell was improved by enhancing the light incoupling via an anti-reflection (AR) coating with a Si random pyramid texture. This led to a significant reduction of R in the short as well as the long λ region and equally resulted in an increase of the EQE. Finally, using a textured Si wafer enhanced $J_{\rm sc}$ even more due to the additional light path enhancement within the absorber. This was mainly evident in a decrease of R and an increase of the EQE for $\lambda > 600\,\mathrm{nm}$ (Fig. 6.4 b)). Additionally, a thinner absorber of 170 $\mu\mathrm{m}$ increased $V_{\rm oc}$ of the solar cell due to a higher photo-generated charge carrier density within the smaller absorber volume, while the passivation quality at the surface was kept at a similar level as for the planar solar cells.

Figure 6.5 presents a detailed optical comparison of the textured SHJ solar cell and a planar cell with a Si random pyramid textured imprint on the front side. All layer depositions for both solar cells were performed in the same way except for the increased $t_{\rm dep}$ on the textured wafer. The EQE (Fig. 6.5 a)) of both solar cells was similar for $\lambda < 600\,\mathrm{nm}$. Apparently, the reduction of the front side R (Fig. 6.4 b)) is dominated by the geometrical shape of the texture and less

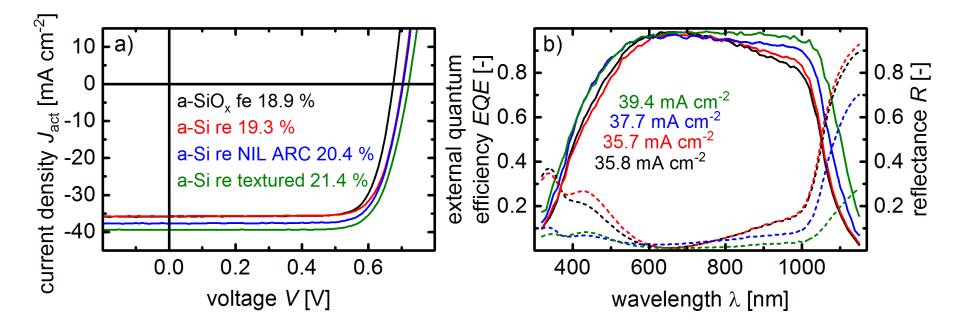


Figure 6.4.: a) J-V curves and solar energy conversion efficiencies (η) of the best SHJ solar cells, realized within this study. Included are an a-SiO_x:H passivated front-emitter (fe) solar cell, an a-Si:H passivated rear-emitter (re) solar cell with and without a nano-imprint lithography (NIL) anti-reflection (AR) coating, and an a-Si:H passivated rear-emitter solar cell on a textured 170 μ m Si wafer. b) The external quantum efficiency (EQE) and reflectance (R) for each of the solar cells. Each integrated short circuit current density from the EQE spectrum ($J_{\text{Sc.DSR}}$) is also included.

influenced by the real part of the refractive index (n) of the textured material. For $\lambda > 600\,\mathrm{nm}$, however, the EQE of the textured solar cell was notably higher than for the imprinted cell, which indicates an improved light incoupling in this λ range. Furthermore, light trapping led to an increase of the EQE in the infrared region, even though a significantly thinner absorber was used for the textured solar cells. However, the improved light incoupling and light trapping also resulted in an increase in parasitic absorptance (A_{paras}) for the textured as compared to the imprinted solar cell (Fig. 6.5 b)). Especially, the weakly absorbed part of the light with $\lambda > 1000\,\mathrm{nm}$ showed a significant increase in A_{paras} which can be related to an increased light path length within the indium tin oxide (ITO) and the nc-SiO_x:H layers and the, thereby, increased A_{paras} by their free charge carriers and defects. However, a slight increase in A_{paras} at shorter wavelengths ($\lambda < 600\,\mathrm{nm}$) was observed as well, designating an increase in A within the front ITO, the nc-SiO_x:H FSF layer and the a-Si:H passivation layer due to longer path lengths in these layers.

Figure 6.6 shows the direct and diffuse components of R for both types of solar cells. Again, the lower R of the textured solar cell for $\lambda > 600 \,\mathrm{nm}$ was evident in the total reflectance (TR) (Fig. 6.6 a)). Furthermore, the textured solar cell showed a

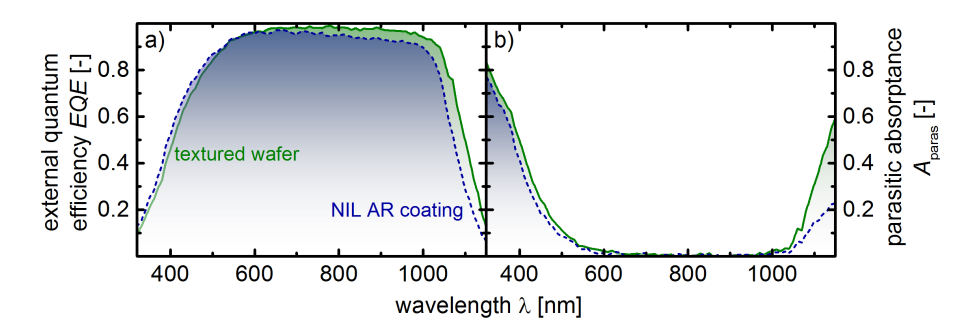


Figure 6.5.: a) Comparison of the EQE of rear-emitter SHJ solar cells on a planar Si wafer with an anti-reflection (AR) coating produced via nano-imprint lithography (NIL) and on a Si random pyramid textured wafer. The same layer stack was used for both cells. b) The parasitic absorptance (A_{paras}) of both cells, as estimated by $A_{paras} = 1 - R - EQE$.

nearly perfect overlap of TR and the diffuse reflectance (DR), indicating that all light was scattered off the incident angle. This was also expressed in the specular reflectance $SR \approx 0$ in Fig. 6.6 b). In contrast, a few percent of SR were still visible for the solar cells with a NIL AR coating, which could be related to a small fraction of planar area for the imprinted texture (see also Fig. 5.15 b)).

6.2.2. Comparison to literature

The solar cell parameters of the best textured SHJ solar cell are compared to reported values of similar SHJ solar cells in literature in Tab. 6.1. For a direct comparison, $J_{\text{sc,DSR}}$ was evaluated from the EQE spectra from literature by using the same solar spectrum and the same λ range for all cells. The first cell, used for comparison, from the Helmholtz-Zentrum Berlin für Materialien und Energie (HZB) was employing <p> nc-SiO_x:H as the emitter layer with a <n> a-Si:H back surface field (BSF) on a 270 μ m FZ wafer. Furthermore, Al-doped zinc oxide (AZO) was used at the rear to reduce A_{paras} by the free charge carriers in the case of the more commonly used ITO. Further optimizations included the application of a <p> μ c-Si:H contact layer between the ITO and the nc-SiO_x:H emitter on the front and a plasma treatment of the a-Si:H passivation layers to enhance the nucleation of nc-Si within the <p> nc-SiO_x:H [25]. The second cell from Ecole Polytechnique Fédérale de Lau-

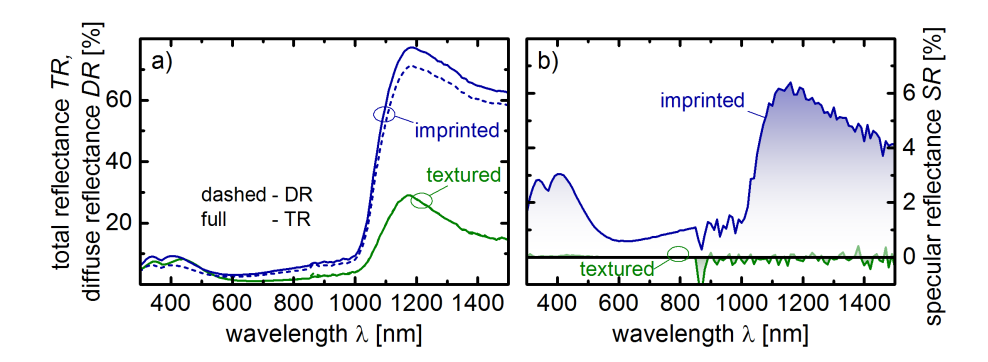


Figure 6.6.: a) Comparison of the total reflectance (TR) and the diffuse reflectance (DR) for a rear-emitter SHJ solar cell with a Si random pyramid textured wafer and a cell with a planar Si absorber with an anti-reflection (AR) coating, produced via nano-imprint lithography (NIL). b) Calculated specular reflectance (SR) for both types of solar cells.

sanne (EPFL) can be considered a classical SHJ solar cell with doped and <i>a-Si:H layers on each side of a 280 μ m thick FZ absorber. Here, the ITO and the front side <p>a-Si:H layers were optimized extensively to maximize J_{sc} of the solar cell [96].

In comparison to the nc-SiO_x:H SHJ solar cell of the HZB, a superior fill factor (FF) and an improved V_{oc} could be achieved at the Forschungszentrum Jülich GmbH (FZJ) by the application of a more conductive <n> nc-SiO_x:H with a similar optical band gap (E_{04}) in comparison to the <p> nc-SiO_x:H, even though a contacting layer towards the ITO was used in the latter case. However, some part

Table 6.1.: Solar cell parameters of selected recent SHJ solar cells from literature in comparison to the best performing cell from this study. The cell results were published by the EPFL and the HZB in 2012 and 2015, respectively [25, 96]. J_{sc} and η denote the aperture area values, while $J_{sc,DSR}$ and η_{act} represent the active area values.

institute	cell size	wafer d	FF	$V_{ m oc}$	$J_{ m sc}$	η	$J_{ m sc,DSR}$	$\eta_{ m act}$
	$[{ m cm}^2]$	$[\mu\mathrm{m}]$	[%]	[mV]	$[\mathrm{mAcm^{-2}}]$	[%]	$[\mathrm{mAcm^{-2}}]$	[%]
FZJ	4	170	75.4	721	36.5	19.8	39.4	21.4
HZB	1	270	72.9	688	40.4	20.3	40.6	20.4
EPFL	4	280	75.3	727	38.1	20.8	39.5	21.6

of the superior $V_{\rm oc}$ was also due to the thinner absorber layer. At the same time, a thinner absorber led to a lowered $J_{\rm sc}$ due to a decrease of A in the long λ range (Fig. 6.7). Nevertheless, the higher $J_{\rm sc}$ of the HZB cell could be mainly attributed to an optimized front layer stack and a very low R in combination with a lower $A_{\rm paras}$ at the rear transparent conductive oxide (TCO) of the solar cell (Fig. 6.7). Nevertheless, without the effect of grid shadowing and by using an identical method to determine $J_{\rm sc,DSR}$, a higher $\eta_{\rm act}$ was obtained with the presented solar cell due to the excellent electronic performance.

With respect to the a-Si:H SHJ solar cell from the EPFL, a similar FF and $V_{\rm oc}$ were achieved with the presented cell design. This is an essential prerequisite for the substitution of a-Si:H layers by nc-SiO_x:H as the main objection to its application is a reduced electronic performance. Nevertheless, the surface passivation of the a-Si:H cell seemed to be superior due to a higher $V_{\rm oc}$ despite the thicker Si absorber. In fact, a multi-step <i> a-Si:H deposition was applied for that cell with intermittent H₂-plasma treatments to produce a high quality passivation with a $\tau_{\rm eff}$ of 7 ms on a textured wafer [77]. Considerable effort was also directed towards an optimization of the front layer stack of this solar cell. This included a reduction of the a-Si:H

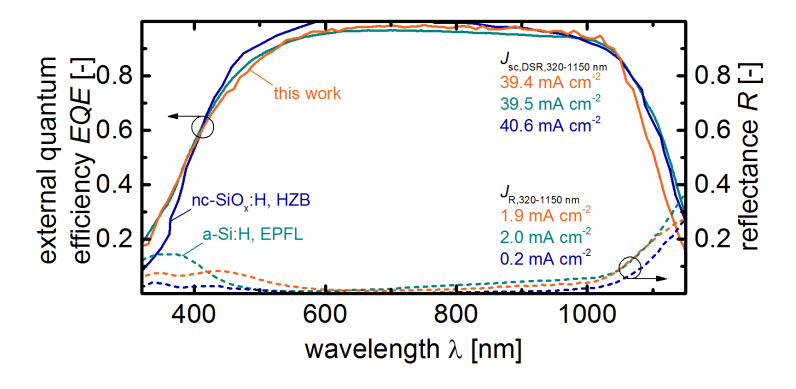


Figure 6.7.: Comparison of the active area EQE spectra and R of the textured SHJ solar cell with nc-SiO_x:H layers and SHJ solar cells from literature [25,96]. The literature data was rescaled to the active area by using the fraction of shadowed area provided in the publications. The integrated short circuit current density from the EQE spectrum ($J_{sc,DSR}$) and the current density loss due to reflexion (J_R) are included for each cell.

thickness to 10 nm and an optimization of the ITO properties. With this, a high $J_{\rm sc,DSR}$ was achieved with a very similar EQE for $\lambda < 600\,\mathrm{nm}$ as compared to the nc-SiO_x:H based SHJ solar cell of this study (Fig. 6.7). However, with a similar optimization, a front layer stack employing nc-SiO_x:H should outperform the a-Si:H at least optically as demonstrated by the HZB solar cell. In the long λ range beyond 1000 nm the a-Si:H solar cell surpassed the EQE of the FZJ cell due to the optimized ITO layers at the front and the rear of the a-Si:H solar cell, which minimized $A_{\rm paras}$ within the ITO layers. In total, $\eta_{\rm act}$ of the HZB and of the FZJ solar cell were highly similar, even though a vastly different layout was used.

From the comparison to the discussed solar cells, several optimization steps towards a higher η can be inferred. First, a detailed optimization or even a replacement of the ITO layers needs to be performed to reduce the significant $A_{\rm paras}$ in the long λ region. Possible candidates to substitute the ITO are AZO [186] or hydrogen doped indium oxide (IOH) [98]. Second, the a-Si:H passivation could be improved further by following the approach of Descoeudres et al. [77] and alternating between an <i> a-Si:H deposition step and a H₂-plasma treatment step. This would also eliminate the need for a post-deposition annealing of the passivation layers. Third, an optimization of the front layer thicknesses towards a minimal $J_{\rm R}$ could provide a straightforward way to increase $J_{\rm sc}$. OPAL 2 has been successfully used for this purpose in SHJ solar cells [25, 96]. Moreover, $J_{\rm R}$ could be reduced even further by applying a different texture for the absorber layer instead of the Si random pyramid texture. This approach will be discussed in the following section.

6.2.3. Surface texture optimization via OPAL 2

The OPAL 2 simulation of the 1-R and $A_{\rm paras}$ of the textured solar cell from Fig. 6.3 a) is presented in Fig. 6.8 a). Similarly to Sec. 5.2.3, the experimental results were well reproduced by the OPAL 2 simulations. A significant difference in $A_{\rm paras}$ was observed for $\lambda < 400\,\mathrm{nm}$, which resulted in an overestimation of the parasitic loss in $J_{\rm sc}$ of about $0.1\,\mathrm{mA\,cm^{-2}}$ for $320\,\mathrm{nm} < \lambda < 400\,\mathrm{nm}$. An offset in $J_{\rm R}$ between the simulated and the experimental spectra had also been found for the planar solar cells and can largely be attributed to the accuracy of the spectrophotometer (see also Sec. 5.3). To evaluate the accuracy of the predictions made by

the simulations, a 70nm thick layer of magnesium fluoride (MgF₂) was added to the solar cell. The resulting 1-R and $A_{\rm paras}$ spectra are shown in Fig. 6.3 b) and compared to the expected changes according to OPAL 2. The general shape of the spectra were well reproduced. Furthermore, a decrease in $J_{\rm R}$ by about $0.2\,{\rm mA\,cm^{-2}}$ due to the MgF₂ layer was predicted by the simulation and observed experimentally. At the same time, the current loss due to $A_{\rm paras}$ increased by about $0.3\,{\rm mA\,cm^{-2}}$ also in accordance with the simulations. Therefore, OPAL 2 simulations can be expected to yield a good prediction of the relative change in the R spectra and $J_{\rm sc,DSR}$ for changes in the front layer stack.

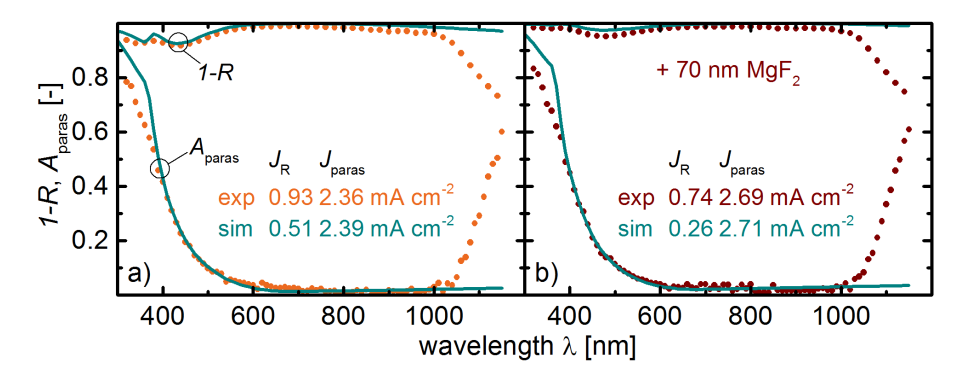


Figure 6.8.: a) 1-reflectance (R) and parasitic absorptance (A_{paras}) of the textured SHJ solar cell. Full lines indicate the results from OPAL 2 simulations of the front side layer stack with a front ITO thickness of 75 nm and a < n > nc-SiO_x:H thickness of 24 nm. A_{paras} was determined by calculating 1 - R - EQE. The losses in J_{sc} due to R and A_{paras} for $350 \, \mathrm{nm} < \lambda < 900 \, \mathrm{nm}$ are indicated in mAcm⁻² as well. b) Simulated and experimental 1 - R and A_{paras} of the textured solar cell with an additional magnesium fluoride (MgF₂) layer of 70 nm.

The simulated R spectra of SHJ solar cells with different surface textures are displayed in Fig. 6.9 a). The overall shape of the spectra is very similar. However, the absolute values of R change with different textures. For a typical texture of random upright pyramids 68% of the normally incident light rays bounce twice on the textured surface before escaping, while 26% bounce three times and the remaining 6% bounce more than three times [187]. In contrast, for a texture of regular upright pyramids 89% of the normally incident light rays bounce twice on

the textured surface and only 11% bounce three times [187]. Ultimately, this resulted in an increase of R and J_R (Fig. 6.9 d)) for the regular upright pyramid texture. At the same time, however, the amount of A_{paras} decreased slightly (Fig. 6.9 c)) due to the decreasing total number of reflections. Nevertheless, a small net loss in the generated current density was observed in Fig. 6.9 b).

Inverting the regular pyramid texture led to a reduction of R in comparison to the random pyramid texture. This is because for an ideal inverted pyramid texture 42% of the normally incident light rays bounce three times, while only 58% bounce twice [187]. This led to a decrease of J_R by about $0.05\,\mathrm{mA\,cm^{-2}}$ and a similar increase in the generated current density. Now, this constitutes the ideal case of no planar area in between the individual inverted pyramids. For a planar fraction of about 10%, which has been found experimentally by Branham et al. for example [188], R was increased significantly and the generated current density decreased accordingly by about $0.2\,\mathrm{mA\,cm^{-2}}$, even falling below the generated current density of the regular upright pyramid textured solar cells. In total, the inverted pyramid texture led to the lowest J_R and highest generated current density, slightly outperforming the common random upright pyramid texture.

Further optimization of the promising inverted pyramid texture is presented in Fig. 6.10. Here, the characteristic angle of the pyramids was adjusted from 40° to 70° to investigate the influence on R and the generated current. The same front layer stack as in Fig. 6.3 a) was applied to the Si wafer and the silicon solar cell with a Si random upright pyramid texture is included for reference. R in Fig. 6.10 a) decreased strongly with increasing the pyramid angle to 70° due to an increasing fraction of light rays being reflected multiple times at the steep pyramid facets of the textured solar cell surface [134]. At a characteristic angle of 70° R did not exceed 0.4% at any point of the R spectrum with the ITO and the nc-SiO_x:H FSF layer providing the AR effect. With this configuration all of the incident light rays were reflected at least four times within the pyramids before emerging. Accordingly, J_R in Fig. 6.10 d) was nearly zero, while it amounted to about $2 \, \text{mAcm}^{-2}$ for a characteristic angle of 40° , corresponding to an obtuse pyramid tip. Then again, the losses due to A_{paras} increased towards larger characteristic angles due to the increasing number of reflections and an increasing path length in the front layers

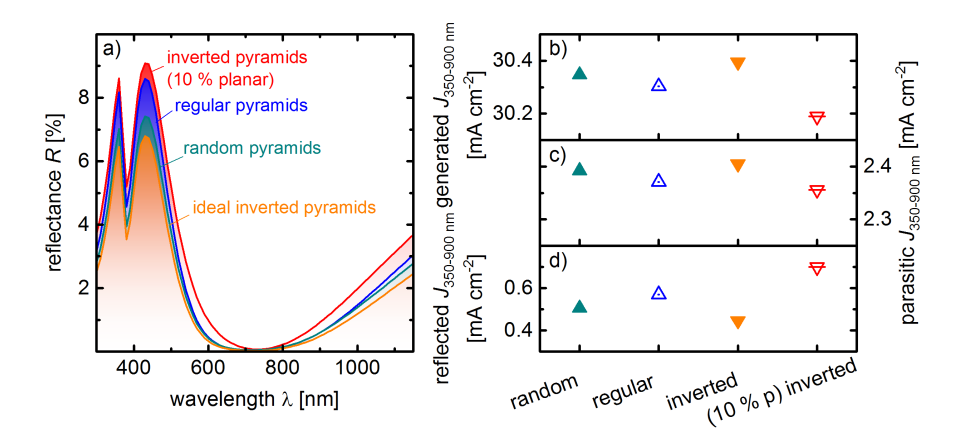


Figure 6.9.: a) Simulated reflectance (R) spectra for different pyramidal textures of a SHJ solar cell. An ideal pyramid angle of 54.7° was adopted for all textures. An inverted pyramid texture with a planar area fraction of 10% was considered as well. b) Generated current density in the SHJ solar cells in 350 nm $< \lambda < 900$ nm for different surface textures. c) Loss in J_{sc} due to parasitic absorptance (A_{paras}) in 350 nm $< \lambda < 900$ nm. d) current density loss due to reflexion (J_R) in 350 nm $< \lambda < 900$ nm.

for the steeper pyramid facets. In total, however, the increase in parasitic loss amounted to just about $0.4 \, \mathrm{mA\,cm^{-2}}$ (Fig. 6.10 c)). Therefore, a significant gain in the generated current density was observed in Fig. 6.10 b) with decreasing J_{R} . Overall, switching from a texture of random upright to regular inverted pyramids could result in an increase of J_{sc} by at least $0.35 \, \mathrm{mA\,cm^{-2}}$ with a layer stack of 75 nm ITO and 24nm nc-SiO_x:H due to a reduced R. However, the full impact on the light trapping within the wafer still needs to be investigated as the rear side of the solar cell was not included in the simulations. Furthermore, the effect of these atomically poorly defined pyramid facets on the passivation quality needs to be examined and considered as well.

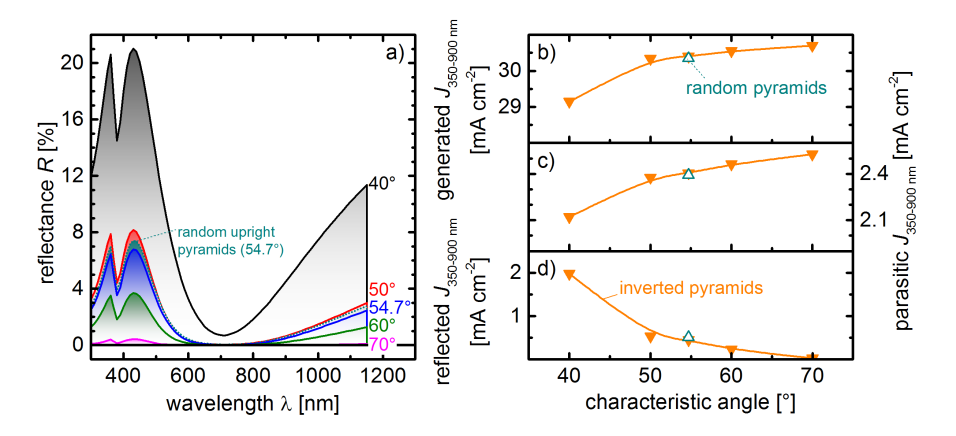


Figure 6.10.: OPAL 2 simulations of SHJ solar cells with regular inverted pyramid textures. The characteristic angle of the pyramids was varied. The properties of the Si random pyramid textured solar cell are included for comparison. a) R spectra, b) generated current density in $350\,\mathrm{nm} < \lambda < 900\,\mathrm{nm}$, c) parasitic loss in $350\,\mathrm{nm} < \lambda < 900\,\mathrm{nm}$, and d) current density loss due to reflexion (J_R) in $350\,\mathrm{nm} < \lambda < 900\,\mathrm{nm}$. The lines serve as a guide to the eye.

6.3. Stability of nc-SiO_x:H SHJ solar cells

The stability of the best performing SHJ solar cell with a nc-SiO_x:H FSF and emitter layer will be tentatively investigated in this section. Here, the textured solar cell with the additional MgF₂ layer was used for the experiments. The results are summarized in Fig. 6.11. Please note the different scales used in Fig. 6.11 a)/c) in comparison to b)/d). Some of the measurements were done at different solar simulators, but for simplicity the presented values were individually rescaled to the values obtained on the initial simulator, which was also described in Sec. 3.3. In a first step, the solar cell was stored in the dark for 4 months in air. This mainly led to a degradation of FF, while $V_{\rm oc}$ also slightly decreased. This might be a result of physical adsorption of atmospheric species (reversible) [189] or chemical changes, e.g. oxidation or H₂-effusion (irreversible) [190]. Afterwards, a 2 hours annealing step at 220 °C was again performed in air to mitigate the changes due to the extended storage. This step caused a decrease in $V_{\rm oc}$ by about 2% (15 mV) and a similar decrease of FF. This might be related to a restructuring of the H at the

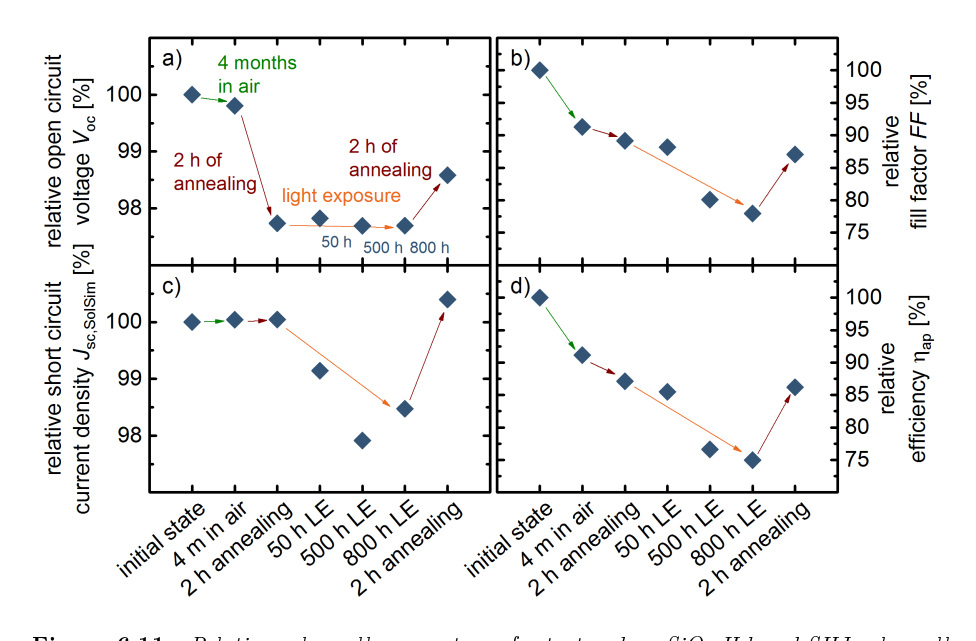


Figure 6.11.: Relative solar cell parameters of a textured nc-SiO_x:H based SHJ solar cell with respect to the initial state of the solar cell. The solar cell was subjected to extended storage in air, extensive light exposure (LE) and annealing treatments in air. The solar cell parameters were measured after each step. The measured parameters include a) the open circuit voltage (V_{oc}), b) the fill factor (FF), c) the aperture area short circuit current density (J_{sc}), and d) the aperture area solar energy conversion efficiency (η_{ap}).

<i> a-Si:H/c-Si interface, which has also been observed for extended annealing of passivation test samples with <i> a-Si:H layers.

Next, the solar cell was subjected to extensive light exposure (LE) by two tungsten halogen lamps set to an illumination intensity of $1\,\mathrm{kW\,m^{-2}}$ (1 sun). Meanwhile the solar cell was kept at $50\,^\circ\mathrm{C}$ by a water cooling system. Furthermore, the cell temperature was reduced to $25\,^\circ\mathrm{C}$ for $30\,\mathrm{min}$ to determine the cell properties at the following time steps: $1\,\mathrm{h}$, $5\,\mathrm{h}$, $10\,\mathrm{h}$, $25\,\mathrm{h}$, $50\,\mathrm{h}$, $100\,\mathrm{h}$, $200\,\mathrm{h}$, $300\,\mathrm{h}$, $400\,\mathrm{h}$, $500\,\mathrm{h}$, $600\,\mathrm{h}$, $700\,\mathrm{h}$, and $800\,\mathrm{h}$. Selected measurements of this sequence are included in Fig. 6.11. During the first $50\,\mathrm{h}$ of the LE a decrease in J_{sc} as well as FF was observed, while V_{oc} slightly increased. Kobayashi et al. [191] reported on the degradation behavior of a-Si:H based SHJ solar cells under extended LE. They found a small increase in

 $V_{\rm oc}$ and FF within the first 50h of LE and tentatively attributed it to a reversal of the Staebler-Wronski effect (SWE) [192] by a shift of the Fermi-level closer to one of the band edges due to the doped a-Si:H layers [191]. Furthermore, they observed a decrease in defect density with increasing LE for lifetime test structures. For the presented cell, this reversal of the SWE might also have caused the slight increase in $V_{\rm oc}$ during the initial stage of the LE (Fig. 6.11 a)). However, no increase in FF was evident (Fig. 6.11 b)). Up to the final LE time of 800h $V_{\rm oc}$ slightly decreased again and FF was drastically reduced to about 78% of the initial value, indicating a degradation of the electrical transport in contrast to a recombination related degradation. Overall, these changes in FF dominated the degradation of η (Fig. 6.11 d)).

The changes were almost fully restored by a subsequent annealing step, which indicates a partial reversibility of the light induced degradation beyond the first 50 h of LE, similarly to the SWE. Apart from major changes in FF, $J_{\rm sc}$ was reduced by about 1.5% (0.5 mA cm⁻²) during the LE. This could mainly be attributed to a decrease in the IQE of the solar cell across the full λ range by about 5% relative (Fig. 6.12 b)). Furthermore, R of the solar was reduced by about 3% absolute (Fig. 6.12 a)), which could not compensate the loss in IQE, so that the overall EQE decreased. The reason for the change in R is unclear so far. After annealing, the IQE recovered only partially: no change was observed for $\lambda < 500$ nm and almost

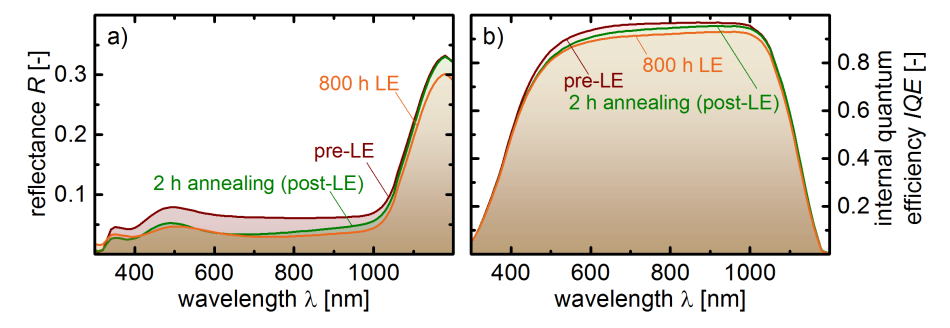


Figure 6.12.: a) Aperture area R spectra of the discussed textured SHJ solar cell before the light exposure (LE) ("pre-LE"), after 800 h of LE, and after a 2h thermal annealing treatment at 220 °C following the LE. b) IQE spectra of the same solar cell.

full recovery was achieved beyond 1000 nm. This indicates that the changes due to LE were only reversible at the rear of the solar cell, while the changes at the front could not be recovered. This finding implies a distinct degradation behavior for each of the absorber interfaces. In contrast to the IQE, R was not restored by the annealing treatment, so that the total $J_{\rm sc}$ slightly increased in comparison to the initial state (Fig. 6.11 c)). Figure 6.11 a) shows that $V_{\rm oc}$ of the solar cell was increased by the annealing treatment after the LE, even though the changes to $V_{\rm oc}$ during the LE were marginal.

Further investigations are necessary to reveal the specific reasons for the degradation of the SHJ solar cells with functional nc-SiO_x:H layers, especially to distinguish between the different effects of R reduction and the partial reversibility of the properties. Nevertheless, the presented findings already indicate that storage, extended LE, and excessive annealing can be detrimental to the performance of SHJ solar cells with nc-SiO_x:H layers, especially affecting the FF.

7. Summary and outlook

Solar cells play an essential part in facilitating a worldwide transition from fossil energy fuels towards renewable sources. However, a substantial contribution by photovoltaics (PV) can only be provided if the costs of PV systems are reduced to a minimum. An important driver for a reduction in the levelized costs of electricity of PV systems is the solar energy conversion efficiency (η) of the individual solar cells. Here, Si solar cells based on the silicon heterojunction (SHJ) technology are advancing to become the highest η technology due to their superior open circuit voltages (V_{oc}) . Nevertheless, several loss mechanisms diminish the ratio between the generated power and the incident solar energy for this technology. One of them is the parasitic absorptance (A_{paras}) of light in the most commonly used hydrogenated amorphous silicon (a-Si:H) layers. $A_{\rm paras}$ of the a-Si:H contributes significantly to a reduction of η , but can be reduced by a substitution with more transparent materials like hydrogenated nanocrystalline silicon oxide (nc-SiO_x:H). nc-SiO_x:H is a hybrid material that combines the high transparency of a hydrogenated amorphous silicon oxide (a-SiO_x:H) matrix with the electrical conductivity of nanocrystalline silicon (nc-Si). Usually, a trade-off between these two contradictory properties has to be tolerated and adjusted according to the specific application.

Accordingly, the first objective of this thesis was to develop nc-SiO_x:H films via plasma enhanced chemical vapor deposition (PECVD) at very high frequency (VHF) in order to improve its optoelectronic trade-off and achieve a reduced parasitic loss in SHJ solar cells. The second objective was to establish a link between the material properties and the solar cell performance and advance the development of nc-SiO_x:H based SHJ solar cells. In detail, p-type doped (<p>) and n-type doped (<n>) nc-SiO_x:H films were extensively optimized and categorized according to their properties and their microstructure. In a next step, they were applied in

7. Summary and outlook

SHJ solar cells in combination with different passivation layers and varying Si wafer absorbers. A summary of the main results and conclusions of this thesis is presented in this chapter. Furthermore, a pathway towards further optimization of the nc-SiO_x:H layers and the SHJ solar cells is devised.

7.1. Summary

A short summary of the main results from each section is presented in the following, spanning from the development of nc-SiO_x :H films at VHF to their application in various SHJ solar cells.

Material development

Parameter optimization In the first part of the thesis doped layers of nc-SiO_x:H were optimized by adjusting the deposition conditions during the VHF PECVD of these films. The optimization included variations in the deposition pressure (p), the deposition power (P), the CO₂ gas flow fraction (f_{CO_2}) , the H₂ gas flow fraction $(f_{\rm H_2})$, the B(CH₃)₃ gas flow fraction $(f_{\rm B(CH_3)_3})$ and the PH₃ gas flow fraction $(f_{\rm PH_3})$. For the variation of p and P two distinct regimes were identified according to the P/p ratio as adapted from [33]. Especially the Raman crystallinity (I_c) and the electrical dark conductivity (σ_D) of the nc-SiO_x:H layers depended strongly on p and P. Generally, an increase of P had the opposite effect as an increase in p. At $50 \,\mathrm{Pa}$ a high I_{c} region with improved phase separation between the nc-Si and O-rich a-SiO_x: H was identified. Next, an increasing amount of trimethylborane (B(CH₃)₃) as a boron-source for $\langle p \rangle$ nc-SiO_x:H led to increased doping at the expense of the nc-Si phase. This amorphization was accompanied by an incorporation of carbon in the nc-SiO_x:H films from the methyl groups of the B(CH₃)₃. An important parameter to adjust the amount of a-SiO_x:H in the films was f_{CO_2} , the increase of which was usually accompanied by a reduction in the amount of nc-Si.

A concluding overview of the deposited nc-SiO_x:H films indicated the existence of an incubation layer of $100-200\,\mathrm{nm}$ thickness with an increased amount of a-SiO_x:H for the nc-SiO_x:H films. Furthermore, the overview demonstrated

the superior optoelectronic performance of the <n>nc-SiO_x:H in comparison to <p>nc-SiO_x:H. Overall, the properties of the VHF nc-SiO_x:H were found to match the best performing films in literature, developed at radio frequency (RF). Nevertheless, a significant improvement of the <p>nc-SiO_x:H films was achieved at the employed deposition system by the optimization at VHF.

Classification of nc-SiO_x:H films For all optimizations of the nc-SiO_x:H films a trade-off between the optical band gap (E_{04}) and $\sigma_{\rm D}$ was found and only a careful adjustment of the deposition parameters in the correct deposition regime provided an increase in E_{04} at a given $\sigma_{\rm D}$. Therefore, a microstructure model for the classification of nc-SiO_x:H films was developed to supply guidelines for the deposition of an optimal phase composition, namely, nc-SiO_x:H films with high amounts of O-rich a-SiO_x:H in combination with conductive nc-Si. In detail, the films were divided in four distinct deposition regions:

- the "fully amorphous region", defined by films containing no nc-Si phase,
- the "onset of nc-Si formation" region, encompassing films with a low amount of nc-Si and a-SiO_x:H,
- the "O and nc-Si enrichment" region, characterized by a high amount of nc-Si and a-SiO_x:H in the nc-SiO_x:H films,
- \bullet the "nc-Si deterioration" region, which exhibits a preferred incorporation of a-SiOx:H against nc-Si in the films.

The optimal optoelectronic trade-off for the nc-SiO_x:H films was identified between the "O and nc-Si enrichment" and the "nc-Si deterioration" region. The utility of the classification was demonstrated for a variation of $f_{\rm PH_3}$ and $f_{\rm CO_2}$. $f_{\rm PH_3}$ was shown to mainly affect $\sigma_{\rm D}$ via doping and have no significant influence on the microstructure in either the "O and nc-Si enrichment" region nor the "nc-Si deterioration" region of nc-SiO_x:H deposition. The subsequent variation of $f_{\rm CO_2}$ in the optimal deposition regions resulted in nc-SiO_x:H films with excellent optoelectronic properties.

Microstructure A detailed investigation of the microstructure was performed via atom probe tomography (APT) which confirmed the phase distribution that was proposed by the microstructure model. Furthermore, for the first time a three di-

7. Summary and outlook

mensional distribution of the interconnected nc-Si network within <n> and <p> nc-SiO_x:H was presented, confirming the anisotropic growth of nc-Si, first revealed by transmission electron microscopy (TEM). This electrically conductive 3D network of nc-Si was surrounded by an O-rich a-SiO_x:H phase providing the high transparency of the films. Moreover, a nearly uniform distribution of the dopant atoms across the phases was found for the <p> as well as the <n> nc-SiO_x:H film.

Planar solar cells

Passivation layers In the first part of the solar cell development, the reproducibility of intrinsic (<i>) a-SiO_x:H was tested and the homogeneity of the deposited films was investigated. The thickness distribution of the passivation layers was related to the performance of the individual SHJ solar cells and thereby a maximal total thickness of 11 nm was suggested to maintain a high fill factor (FF). Furthermore, the a-SiO_x:H thickness at the rear side of the solar cell, namely at the <p> nc-SiO_x:H back surface field (BSF), was found to limit V_{oc} . Thereby, demanding a higher <i> a-SiO_x:H thickness at the rear interface.

A superior passivation quality could be achieved by $\langle i \rangle$ a-Si:H passivation layers. These were optimized by adjusting the substrate temperature $(T_{\rm sub})$ via the heater temperature $(T_{\rm H})$ and by adjusting $f_{\rm H_2}$. High effective carrier lifetime $(\tau_{\rm eff})$ of up to 5ms were achieved by depositing the a-Si:H in the amorphous region with a high hydrogen content $(c_{\rm H})$ and extended thermal annealing to rearrange the mobile H and effectively saturate the Si dangling bonds at the absorber surface. The superior passivation quality of the a-Si:H led to an increase in $V_{\rm oc}$ of about $20\,{\rm mV}$ as compared to $\langle i \rangle$ a-SiO_x:H passivation layers.

Doped nc-SiO_x:H layers In a next step, the doped nc-SiO_x:H layers developed at VHF were applied in SHJ solar cells. Here, the nc-SiO_x:H was applied as an emitter layer, a BSF, and a front surface field (FSF) layer. A limitation of FF by the <n>nc-SiO_x:H emitter layer was found for nc-SiO_x:H layers with low amounts of nc-Si by a variation of the nc-SiO_x:H emitter in front-emitter solar cells with a-SiO_x:H passivation layers on <p> wafers. At the same time, A_{paras} at the front decreased towards an increasing amount of a-SiO_x:H within the nc-SiO_x:H and a,

thereby, increased E_{04} of the nc-SiO_x:H. The best trade-off between FF and the short circuit current density $(J_{\rm sc})$ was achieved with an <n> nc-SiO_x:H emitter layer with $E_{04}=2.3\,{\rm eV}$ and $\sigma_{\rm D}=0.1\,{\rm S\,cm^{-1}}$.

A similar variation of an <n> nc-SiO_x:H FSF layer was performed in rear-emitter solar cells with a-Si:H passivation layers on <n> wafers with a nc-SiO_x:H emitter layer. Here, a poorer nucleation of the nc-Si within the nc-SiO_x:H was found for the a-Si:H passivation layers in comparison to a-SiO_x:H. This effect was especially prominent for hydrogenated microcrystalline silicon (μ c-Si:H) films and indicated a different growth mechanism of the nc-Si phase for μ c-Si:H films in comparison to nc-SiO_x:H films. These implications were in accordance with findings during the material development which pointed at a lower incubation layer thickness for nc-SiO_x:H and reports from literature which found the nc-Si in a globular arrangement in nc-SiO_x:H in contrast to a cone-like growth in μ c-Si:H. Despite this, a similar effect of the nc-SiO_x:H FSF layer variation was found as for the nc-SiO_x:H emitter layers and an overall active area solar energy conversion efficiency (η act)= 19.3% was reached mainly due to the improved passivation quality by the <i> a-Si:H.

Further insights into the properties of nc-SiO_x:H layers at a device relevant thickness of 20 nm were gained by simulations of the optical solar cell properties via a freeware program for the optical analysis of the front surface of a solar cell (OPAL 2). Overall the experimental reflectance (R) and external quantum efficiency (EQE) of the rear-emitter SHJ solar cells were well reproduced by simulations with nc-SiO_x:H layer properties extracted from several hundreds of nm thick films. However, A_{paras} in the short wavelength (λ) range of light was overestimated. Accordingly, the thin nc-SiO_x:H layers in the solar cells show an increased optical transparency in agreement with the increased oxygen content (c_{O}) in the nc-SiO_x:H incubation layer and can be expected to contain an increased amount of a-SiO_x:H and reduced amount of nc-Si as compared to thick nc-SiO_x:H films.

Solar cell design optimization Improvements in the solar cell design were achieved by switching to a rear-emitter design to benefit from the innately higher $\tau_{\rm eff}$ of <n> Si wafers while still exploiting the increased optoelectronic performance of <n> nc-SiO_x:H films at the front of the solar cell. Additionally, the rear-emitter

7. Summary and outlook

design offers some potential in the optimization of the front indium tin oxide (ITO) layer. Furthermore, increasing $T_{\rm H}$ during the ITO deposition resulted in a reduced electron density $(n_{\rm e})$ of the ITO which in turn significantly reduced $A_{\rm paras}$ in the long λ range.

The low $A_{\rm paras}$ in nc-SiO_x:H could not be fully exploited in planar SHJ solar cells due to the poor light incoupling. Therefore, a novel approach was implemented to produce anti-reflection (AR) coatings via nano-imprint lithography (NIL), fabricating SiO₂-like imprint layers with Si random pyramid textures. These AR coatings effectively increased the absorptance (A) across the full light spectrum which translated to an increase in the EQE, especially for solar cells with a transparent nc-SiO_x:H FSF layer. In total, this yielded an $\eta_{\rm act}$ of 20.4% and a $J_{\rm sc,DSR}$ of 37.7 mA cm⁻² for a planar SHJ solar cell.

Textured solar cells

Effect on passivation Wet-chemically texturing a Si wafer offers the advantage of strongly increasing light incoupling in combination with efficient light trapping. However, passivation of the textured surface can be an issue. Therefore, part of the $\langle i \rangle$ a-Si:H optimization was repeated on textured Si substrates. The onset of the decrease of $\tau_{\rm eff}$ in the as-deposited and the annealed state was found at lower $T_{\rm H}$ in comparison to the planar Si wafers and explained by epitaxial growth of Si at the pyramid grooves and edges. Nevertheless, by the low $T_{\rm H}$ deposition in combination with annealing, a high $\tau_{\rm eff}$ could be achieved which corresponded to about 35% of $\tau_{\rm eff}$ on the planar reference. This difference was shown to be due to the increase in surface area and a reduced wafer thickness. Therefore, the surface passivation quality by the deposited and annealed $\langle i \rangle$ a-Si:H on textured and planar wafers was found to be comparable.

The application of the novel VHF nc-SiO_x:H layers led to a deterioration of the passivation quality which was explained by the high density of atomic H during the deposition because similar nc-SiO_x:H layers deposited at a lower H flow and RF did not deteriorate the a-Si:H passivation. The atomic H is essential to produce high performance nc-SiO_x:H films with a low a-Si:H content and O-rich a-SiO_x:H and nc-Si as the main components. Albeit, it presumably lead to a strong etching

of the a-Si:H passivation layers. However, this etching was only found for textured surfaces and was not observed on planar a-Si:H passivated surfaces. Accordingly, weak points within the passivation layer due to the surface geometry (e.g. edges, vertices) might result in a stronger sensitivity to H etching than planar areas.

nc-SiO_x:H in textured solar cells A rear-emitter SHJ solar cell on a textured <n> absorber with a nc-SiO_x:H FSF and emitter layer was successfully produced. Thereby, yielding a $2x2\,\mathrm{cm}^2$ solar cell with the highest η_{act} of 21.4% developed in this thesis. The electrical performance with $V_{\mathrm{oc}} = 721\,\mathrm{mV}$ and FF = 75.4% was comparable to the parameters reported on a-Si:H based SHJ solar cells by the EPFL [96] and outperformed an optically optimized nc-SiO_x:H based SHJ solar cell reported by the HZB [25]. However, the optical performance was inferior to the latter cell. Accordingly, optimization steps towards even higher η were derived from a detailed comparison to these solar cells. Nevertheless, even in the non-optimized state a high active area current density (J_{act}) of 39.4 mA cm⁻² was achieved.

Simulation An optical optimization of the front side texture was performed for the deposited layer stack via simulations in OPAL 2. An inverted pyramid texture was found to show a slight decrease in R in comparison to the Si random pyramid texture, resulting in a decrease of the current density loss due to reflexion $(J_{\rm R})$ by about $0.05\,{\rm mA\,cm^{-2}}$. Furthermore, the angle of the inverted pyramids was varied and almost no R was found for a characteristic angle of $70\,^{\circ}$, indicating an increase in $J_{\rm sc}$ by about $0.35\,{\rm mA\,cm^{-2}}$ with respect to the Si random pyramid texture.

Stability Lastly, the stability of the nc-SiO_x:H based SHJ solar cell was examined. Storage for several months resulted in a decrease of $V_{\rm oc}$ and especially FF which were not recoverable by annealing. Similarly, extended light exposure (LE) up to 800 h led to a decrease in $V_{\rm oc}$, $J_{\rm sc}$ and FF. Here, the changes in $V_{\rm oc}$ and FF were recovered by a subsequent annealing. Albeit, the internal quantum efficiency (IQE) was only recovered in the long λ range of light, designating a different degradation at the front and the rear. Overall, the cell degradation was governed by changes in FF, indicating a predominant effect on the electrical transport.

7. Summary and outlook

7.2. Outlook

Several directions for further improvement emerge from the presented results in the development of $\operatorname{nc-SiO}_x$:H films and the SHJ solar cells employing them in various functions. Accordingly, some recommendations are presented in the following grouped in material investigations and device optimization.

nc-SiO_x:H development

Taking the optoelectronic properties of nc-SiO_x:H to its limits necessitates the coexistence of a silicon dioxide (SiO₂)-like phase with a highly conductive network of nc-Si. Ideally, any a-Si:H should be fully substituted by nc-Si which has a higher conductivity and a higher transparency in the short λ range. To achieve this, a high amount of atomic H in the plasma can be used. However, this may also damage the passivation layer and deteriorate $V_{\rm oc}$ of the SHJ solar cell. The detailed reasons for the damage to the passivation layer and appropriate countermeasures still need to be investigated to be able to make use of these high performance nc-SiO_x:H films. Especially, the role of the surface texture is still unclear.

Furthermore, alternative and more stable passivation layers like SiO_2 might be resistant to the harsh processing conditions during the deposition of high performance nc-SiO_x:H layers. A similar approach has already been used in case of hydrogenated microcrystalline silicon carbide (μ c-SiC:H) layers to prevent damage by atomic H to the absorber surface [193]. The combination with a SiO₂ passivation layer would also allow to explore high temperature depositions of nc-SiO_x:H and examine the annealing behavior of the material at elevated temperatures which could provide access to unique microstructures, e.g. by increasing the nc-Si crystallite size through Ostwald ripening.

Another topic of material research for $\operatorname{nc-SiO}_x$:H is a dedicated and systematic study of the nc-Si network within the films. Here, APT could provide means to characterize the nc-Si network for films deposited at vastly different deposition conditions but with similar optoelectronic properties. Especially the detailed phase distributions would be accessible by this method and allow for a correlation with the $\operatorname{nc-SiO}_x$:H properties. For example the $\operatorname{nc-SiO}_x$:H films developed at lower H

flows and RF could be compared to films deposited at high $f_{\rm H_2}$ and VHF.

Moreover, the nucleation behavior of $\operatorname{nc-SiO}_x$:H, especially on a-Si:H covered substrates, needs to be investigated and optimized to be able to reduce the thickness of the $\operatorname{nc-SiO}_x$:H layer below 20 nm. Highly doped layers of a-Si:H are only 5 – 10 nm thick in high- η SHJ solar cells and thereby show a low A_{paras} . To compete, $\operatorname{nc-SiO}_x$:H layers have to be reduced to similar thicknesses which might even improve the electrical properties of the solar cell due to the superior dopant efficiency in nc-Si as compared to a-Si:H. Alternatively, the dopant concentration could be increased to reduce the size of the space charge region within the nc-Si and prevent a full depletion of the material. Whereas in the present study f_{PH_3} was limited to 5% due to the phosphine (PH₃) precursor gas being diluted in silane (SiH₄). Another approach might be to employ a thinner highly crystalline nc-SiO_x:H with a nominally low E_{04} , considering that the formation of the incubation layer will result in an increased c_{O} and therefore E_{04} in the solar cell.

nc-SiO_x:H based SHJ solar cells

The effects of nc-SiO_x:H layers should be discussed in high-performance devices to access the full impact of the substitution of a-Si:H by nc-SiO_x:H, especially regarding the electronic properties of the solar cells. Furthermore, the ever increasing η at the industrial scale necessitates a constant improvement of η at the research level as well, to provide relevant insights into the operation of these solar cells. Therefore, a further optimization of the solar cell design presented in this study is highly desirable. Some steps towards an improved η were derived from a comparison to similar SHJ solar cells in Sec. 6.2.2. These include:

- a detailed optoelectronic optimization of the ITO layers and their thicknesses to reduce $A_{\rm paras}$ due to the free charge carriers, especially considering the rear-emitter design of the solar cells
- a replacement of the ITO layers by another transparent conductive oxide (TCO) with lower A_{paras} like hydrogen doped indium oxide (IOH) or Al-doped zinc oxide (AZO)
- an optimization of the a-Si:H passivation quality in the as-deposited state

7. Summary and outlook

• a reduction of the current density loss due to reflexion by optimization of the front layer stack and wafer texture

Additionally, the following adjustments and research activities could result in a higher η :

- the implementation of alternative textures to enhance the light incoupling and light trapping within the cells, e.g. inverted pyramid textures
- an optimization of the <i> a-Si:H passivation layer thicknesses at the front and the rear of the solar cells to achieve an improvement in FF or V_{oc}
- switching to a screen-printed metal grid on the front side to reduce shadow losses and achieve a competitive aperture area solar energy conversion efficiency (η_{ap})
- an optimization of the rear-emitter layer in the rear-emitter solar cells
- \bullet the application of $<\!\!\mathrm{i}\!\!>$ a-SiO $_{\!x}:\!\!H$ at the front of the solar cells to enhance the hole-repelling effect of the $<\!\!\mathrm{n}\!\!>$ FSF layer due to its high valence band offset
- upscaling of the solar cell size to reduce edge effects and become more industrially relevant

A. Symbols and abbreviations

```
(b)
             bending
(\mathbf{s})
             stretching
<i>
             intrinsic
             n-type doped
<n>
             p-type doped
absorption coefficient
\alpha
             sub-band gap absorption at a photon energy of 1\,\mathrm{eV}
\alpha_{1\mathrm{eV}}
\Delta E_{\rm C}
             conduction band offset
\Delta E_{\rm V}
             valence band offset
             solar energy conversion efficiency
\eta
             active area solar energy conversion efficiency
\eta_{\rm act}
             aperture area solar energy conversion efficiency
\eta_{
m ap}
\lambda
             wavelength
             charge carrier mobility
μ
            hydrogenated microcrystalline silicon
μc-Si:H
\mu c	ext{-SiC:H} hydrogenated microcrystalline silicon carbide
μc-SiO<sub>x</sub>:H hydrogenated microcrystalline silicon oxide
             Hall electron mobility
             wavenumber
             resistivity
             electrical conductivity
             electrical dark conductivity
\sigma_{\mathrm{D}}
             effective carrier lifetime
	au_{	ext{eff}}
             absorptance
A
             parasitic absorptance
A_{\rm paras}
```

A. Symbols and abbreviations

a-Si:H hydrogenated amorphous silicon

 $\text{a-SiO}_{\mathbf{x}} \text{:H} \quad \text{hydrogenated amorphous silicon oxide}$

AC alternating current

APT atom probe tomography

AR anti-reflection

AZO Al-doped zinc oxide

b-Si black silicon BCback contact trimethylborane $B(CH_3)_3$ BSFback surface field c-Si crystalline silicon hydrogen content c_{H} oxygen content c_{O} CO_2 carbon dioxide

CVD chemical vapor deposition

 $egin{array}{ll} {
m CZ} & {
m Czochralski} \\ d & {
m thickness} \end{array}$

 $\begin{array}{ll} D & \text{diffusion coefficient} \\ \text{DC} & \text{direct current} \\ d_{\text{el}} & \text{electrode spacing} \\ DR & \text{diffuse reflectance} \end{array}$

 ${\bf DSR} \qquad \quad {\bf differential \ spectral \ response}$

 E_{04} optical band gap $E_{\rm C}$ conduction band edge

 E_{F} Fermi level

EFTEM energy filtered transmission electron microscopy

EPFL Ecole Polytechnique Fédérale de Lausanne

EQE external quantum efficiency

 $E_{
m V}$ valence band edge

 $f_{\mathrm{B(CH_3)_3}}$ B(CH₃)₃ gas flow fraction $f_{\mathrm{CO_2}}$ CO₂ gas flow fraction

FF fill factor

 $f_{\rm H_2}$ H₂ gas flow fraction

 $f_{\mathrm{PH_3}}$ PH₃ gas flow fraction

FSF front surface field

FTIR Fourier transform infrared spectroscopy

FZ float-zone

FZJ Forschungszentrum Jülich GmbH

 H_2 hydrogen

HF hydrofluoric acid

HIT[®] heterojunction with intrinsic thin layer

HRTEM high resolution transmission electron microscopy

HZB Helmholtz-Zentrum Berlin für Materialien und Energie

I electrical current

IBC interdigitated back contact

 $I_{\rm c}$ Raman crystallinity iFF implied fill factor

IOH hydrogen doped indium oxide

IPA isopropyl alcohol

IQE internal quantum efficiency

IR intermediate reflector

ITO indium tin oxide

 $iV_{\rm oc}$ implied open circuit voltage

IZO indium zinc oxide

 J_0 dark saturation current density

 $J_{\rm act}$ active area current density

 $J_{\rm R}$ current density loss due to reflexion

 $J_{\rm sc}$ short circuit current density

 $J_{
m sc,DSR}$ integrated short circuit current density from the EQE spectrum

k imaginary part of the refractive index

KOH potassium hydroxide

 $\begin{array}{ll} LE & light\ exposure \\ LiF_x & lithium\ fluoride \\ MgF_2 & magnesium\ fluoride \\ MoO_x & molybdenum\ oxide \\ \end{array}$

mpp maximum power point

A. Symbols and abbreviations

MWT metal wrap through

n real part of the refractive index

NaOH sodium hydroxide nc-Si nanocrystalline silicon

nc-SiO_x:H hydrogenated nanocrystalline silicon oxide

 $n_{\rm e}$ electron density

NIL nano-imprint lithography

 O_2 oxygen

OPAL 2 freeware program for the optical analysis of the front surface of a solar

cell

p deposition pressure P deposition power

PDS photothermal deflection spectroscopy

PECVD plasma enhanced chemical vapor deposition

pFF pseudo fill factor

PH₃ phosphine

PLT photoconductance lifetime testing

 ${\rm PV} \qquad \quad {\rm photovoltaic}$

PVD physical vapor deposition

QSSPC quasi steady-state photo conductance

R reflectance

RBS Rutherford backscattering spectrometry

 $r_{
m dep}$ deposition rate RF radio frequency $R_{
m s}$ series resistance RT room temperature

S surface recombination velocity

 ${
m SCOUT}$ software for the simulation and analysis of optical spectra

SEM scanning electron microscopy

SHJ silicon heterojunction

SiH₄ silane

 SiO_2 silicon dioxide

SiO_x sub-stoichiometric silicon oxide

SIPOS semi-insulating polycrystalline silicon

SMU source measurement unit

 SnO_2 tin dioxide

SR specular reflectance SWE Staebler-Wronski effect

T transmittance $t_{\rm a}$ annealing time

 $T_{\rm a}$ annealing temperature

TCO transparent conductive oxide

 $t_{\rm dep}$ deposition time

TEM transmission electron microscopy

TF thin-film

 $T_{
m H}$ heater temperature

TMAH tetramethylammonium hydroxide
TPC transient photo conductance

TR total reflectance

 $T_{
m sub}$ substrate temperature

 $egin{array}{lll} UV & & ext{ultraviolet} \ V & ext{voltage} \ V_{ ext{bias}} & ext{bias voltage} \ V_{ ext{built}} & ext{built in voltage} \ \end{array}$

VHF very high frequency $V_{
m oc}$ open circuit voltage

 WO_{x} tungsten oxide

B. List of publications

Publications related to this work

Journal publications

- A. Richter, L. Zhao, F. Finger, and K. Ding, Nano-composite microstructure model for the classification of hydrogenated nanocrystalline silicon oxide thin films, Surface and Coatings Technology 295, 119 – 124 (2015)
- A. Richter, F. Lentz, M. Meier, F. Finger, and K. Ding, Light management in planar silicon heterojunction solar cells via nanocrystalline silicon oxide films and nano-imprint textures, Physica Status Solidi (A) 213, 1976 – 1982 (2016)
- A. Richter, V. Smirnov, A. Lambertz, K. Welter, K. Ding, and F. Finger, Versatility of doped nanocrystalline silicon oxide for applications in silicon thin-film and heterojunction solar cells, Solar Energy Materials and Solar Cells 174, 196 – 201 (2018)
- M. Smeets, F. Lentz, A. Richter, Y. Augarten, K. Bittkau, K. Ding, R. Carius, U. Rau, and U. W. Paetzold, Prototyping of nanophotonic grating back contacts for light trapping in planar silicon solar cells, Physica Status Solidi A 213, 1949 – 1954 (2016)
- M. Smeets, K. Bittkau, F. Lentz, A. Richter, K. Ding, R. Carius, U. Rau, and U. W. Paetzold, Post passivation light trapping back contacts for silicon heterojunction solar cells, Nanoscale 8, 18726 – 18733 (2016)
- U. Aeberhard, P. Czaja, M. Ermes, B. E. Pieters, G. Chistiakova, K. Bittkau,
 A. Richter, K. Ding, S. Giusepponi, and M. Celino, Towards a multi-scale approach to the simulation of silicon hetero-junction solar cells, Journal of Green Engineering 5, 11 32 (2016)

B. List of publications

- 7. M. Pomaska, A. Richter, F. Lentz, T. Niermann, F. Finger, U. Rau, and K. Ding, Wide gap microcrystalline silicon carbide emitter for amorphous silicon oxide passivated heterojunction solar cells, Japanese Journal of Applied Physics 56, 022302 (2017)
- 8. D. Y. Kim, F. Lentz, Y. Liu, A. Singh, A. Richter, M. Pomaska, A. Lambertz, and K. Ding, Selective dry etching of p-type Si films for photolithography of interdigitated back contact silicon heterojunction solar cells, IEEE Journal of Photovoltaics 7, 1292 1297 (2017)

Publications in conference proceedings

1. A. Richter, L. Zhao, F. Finger, and K. Ding, Microstructure model for nanocrystalline hydrogenated silicon oxide thin films in silicon heterojunction solar cells, IEEE 42nd Photovoltaic Specialist Conference (PVSC) 2015, 1-4 (2015)

C. Curriculum Vitae

Personal details

Name Alexei Richter

Date of birth November 25th, 1986
Place of birth Esil, Kazakhstan

Citizenship German

Education

2014-2017 PhD student at IEK-5 (Photovoltaik)

Forschungszentrum Jülich GmbH

2007-2012 Diplom in Material Science at TU Dresden

Area of specialization: functional materials

and computational materials science

Master thesis at IfW Dresden

 ${\bf Title:\ Phasenbildung,\ Struktur\ und\ magnetische\ Eigenschaften}$

mittels PLD hergestellter epitaktischer Y-Co-Dünnschichten

1999-2006 Hümmling-Gymnasium, Sögel

- [1] Renewable Energy Policy Network for the 21st Century (REN21), Renewables 2016 Global Status Report, Technical report, 2016.
- [2] C. Battaglia, A. Cuevas, and S. De Wolf, Energy & Environmental Science (2016).
- [3] International Energy Agency (IEA), Technology Roadmap: Solar Photovoltaic Energy, Technical report, 2014.
- [4] V. Devabhaktuni, M. Alam, S. Shekara Sreenadh Reddy Depuru, R. C. Green, D. Nims, and C. Near, Renewable and Sustainable Energy Reviews 19, 555 (2013).
- [5] A. Louwen, W. van Sark, R. Schropp, and A. Faaij, Solar Energy Materials and Solar Cells 147, 295 (2016).
- [6] International Renewable Energy Agency (IRENA), REthinking Energy 2017, Technical report, 2017.
- [7] A. Polman, M. Knight, E. C. Garnett, B. Ehrler, and W. C. Sinke, Science 352, 1 (2016).
- [8] K. Masuko, M. Shigematsu, T. Hashiguchi, D. Fujishima, M. Kai, N. Yoshimura, T. Yamaguchi, Y. Ichihashi, T. Mishima, N. Matsubara, T. Yamanishi, T. Takahama, M. Taguchi, E. Maruyama, and S. Okamoto, IEEE Journal of Photovoltaics 4, 1433 (2014).
- [9] M. Taguchi, A. Yano, S. Tohoda, K. Matsuyama, Y. Nakamura, T. Nishiwaki, K. Fujita, and E. Maruyama, IEEE Journal of Photovoltaics 4, 96 (2014).
- [10] T. Matsushita, T. Aoki, T. Otsu, H. Yamoto, H. Hayashi, M. Okayama, and Y. Kawana, Japanese Journal of Applied Physics 15, 35 (1976).

- [11] W. Füssel, W. Henrion, and R. Scholz, Microelectronic Engineering 22, 355 (1993).
- [12] S. S. Chao, G. Lucovsky, S. Y. Lin, C. K. Wong, P. D. Richard, D. V. Tsu, Y. Takagi, J. E. Keem, J. E. Tyler, and P. Pai, Journal of Non-Crystalline Solids 77/78, 929 (1985).
- [13] K. Haga, K. Yamamoto, M. Kumano, and H. Watanabe, Japanese Journal of Applied Physics 25, L39 (1986).
- [14] G. Lucovsky, Solar Energy Materials 8, 165 (1982).
- [15] K. Haga and H. Watanabe, Japanese Journal of Applied Physics 29, 636 (1990).
- [16] P. Sichanugrist, T. Yoshida, Y. Ichikawa, and H. Sakai, Journal of Non-Crystalline Solids 164-166, 1081 (1993).
- [17] V. Smirnov, A. Lambertz, S. Moll, M. Bär, D. E. Starr, R. G. Wilks, M. Gorgoi, A. Heidt, M. Luysberg, B. Holländer, and F. Finger, Physica Status Solidi (A) 213, 1814 (2016).
- [18] P. Cuony, D. T. L. Alexander, I. Perez-Wurfl, M. Despeisse, G. Bugnon, M. Boccard, T. Söderström, A. Hessler-Wyser, C. Hébert, and C. Ballif, Advanced Materials 24, 1182 (2012).
- [19] A. Lambertz, F. Finger, R. E. I. Schropp, U. Rau, and V. Smirnov, Progress in Photovoltaics: Research and Applications 23, 939 (2015).
- [20] M. Pomaska, A. Richter, F. Lentz, T. Niermann, F. Finger, U. Rau, and K. Ding, Japanese Journal of Applied Physics 56, 022302 (2017).
- [21] A. Sarker, C. Banerjee, and A. K. Barua, Journal of Physics D: Applied Physics 35, 1205 (2002).
- [22] H. Tan, P. Babal, M. Zeman, and A. H. M. Smets, Solar Energy Materials and Solar Cells 132, 597 (2015).
- [23] M. Klingsporn, S. Kirner, C. Villringer, D. Abou-Ras, I. Costina, M. Lehmann, and B. Stannowski, Journal of Applied Physics 119, 223104 (2016).
- [24] L. V. Mercaldo, P. Delli Veneri, I. Usatii, E. M. Esposito, and G. Nicotra, Solar Energy Materials and Solar Cells 119, 67 (2013).

- [25] L. Mazzarella, S. Kirner, B. Stannowski, L. Korte, B. Rech, and R. Schlatmann, Applied Physics Letters 106, 023902 (2015).
- [26] H. A. Gatz, J. K. Rath, M. A. Verheijen, W. M. M. Kessels, and R. E. I. Schropp, Physica Status Solidi (A) 213, 1932 (2016).
- [27] J. Stuckelberger, G. Nogay, P. Wyss, Q. Jeangros, C. Allebé, F. Debrot, X. Niquille, M. Ledinsky, A. Fejfar, M. Despeisse, F.-J. Haug, P. Löper, and C. Ballif, Solar Energy Materials and Solar Cells 158, 2 (2016).
- [28] G. Lucovsky, Journal of Non-Crystalline Solids 227-230, 1 (1998).
- [29] P. Delli Veneri, L. Mercaldo, and I. Usatii, Progress in Photovoltaics: Research and Applications 21, 148 (2013).
- [30] W. Zhao, L.-Y. Du, Z.-Y. Jiang, C.-C. Yin, W. Yu, and G.-S. Fu, Chinese Physics B 24, 108102 (2015).
- [31] C. Shin, S. M. Iftiquar, J. Park, S. Ahn, S. Kim, J. Jung, S. Bong, and J. Yi, Materials Chemistry and Physics 159, 64 (2015).
- [32] A. Lambertz, T. Grundler, and F. Finger, Journal of Applied Physics 109, 113109 (2011).
- [33] O. Gabriel, S. Kirner, M. Klingsporn, F. Friedrich, B. Stannowski, and R. Schlatmann, Plasma Processes and Polymers 12, 82 (2015).
- [34] K. Nomoto, H. Sugimoto, A. Breen, A. Ceguerra, T. Kanno, S. P. Ringer, I. P. Wurfl, G. J. Conibeer, and M. Fujii, The Journal of Physical Chemistry C 120, 17845 (2016).
- [35] B. Liedke, K.-H. Heinig, A. Mücklich, and B. Schmidt, Applied Physics Letters 103, 133106 (2013).
- [36] M. Ivanda, H. Gebavi, D. Ristić, K. Furić, S. Musić, M. Ristić, S. Žonja, P. Biljanović, O. Gamulin, M. Balarin, M. Montagna, M. Ferarri, and G. C. Righini, Journal of Molecular Structure 834-836, 461 (2007).
- [37] D. Wolfe and G. Lucovsky, Journal of Non-Crystalline Solids 269, 1009 (2000).
- [38] B. G. Lee, D. Hiller, J. W. Luo, O. E. Semonin, M. C. Beard, M. Zacharias, and P. Stradins, Advanced Functional Materials 22, 3223 (2012).
- [39] Z. Ni, X. Pi, and D. Yang, Physical Review B 89, 035312 (2014).

- [40] A. Lambertz, Development of Doped Microcrystalline Silicon Oxide and its Application to Thin-Film Silicon Solar Cells, Phd thesis, Universiteit Utrecht, 2015.
- [41] A. Richter, F. Lentz, M. Meier, F. Finger, and K. Ding, Physica Status Solidi (A) 213, 1976 (2016).
- [42] A. Lambertz, V. Smirnov, T. Merdzhanova, K. Ding, S. Haas, G. Jost, R. E. I. Schropp, F. Finger, and U. Rau, Solar Energy Materials and Solar Cells 119, 134 (2013).
- [43] M. Stuckelberger, R. Biron, N. Wyrsch, F.-J. Haug, and C. Ballif, Renewable and Sustainable Energy Reviews (2017).
- [44] V. Smirnov, W. Böttler, A. Lambertz, H. Wang, R. Carius, and F. Finger, Physica Status Solidi (C) 1056, NA (2010).
- [45] P. Delli Veneri, L. Mercaldo, and I. Usatii, Applied Physics Letters 97, 023512 (2010).
- [46] V. Smirnov, A. Lambertz, S. Tillmanns, and F. Finger, Canadian Journal of Physics 92, 932 (2014).
- [47] V. Smirnov, A. Lambertz, B. Grootoonk, R. Carius, and F. Finger, Journal of Non-Crystalline Solids 358, 1954 (2012).
- [48] J. Sritharathikhun and T. Krajangsang, International Journal of Photoenergy **2014**, 8 (2014).
- [49] K. Ding, U. Aeberhard, F. Finger, and U. Rau, Physica Status Solidi (RRL)- Rapid Research Letters 6, 193 (2012).
- [50] S. Rattanapan, T. Watahiki, S. Miyajima, and M. Konagai, Japanese Journal of Applied Physics 50, 082301 (2011).
- [51] W. Chen, V. Depauw, F. Haddad, J.-L. Maurice, and P. Roca i Cabarrocas, Solar Energy Materials and Solar Cells 157, 154 (2016).
- [52] W. Fuhs, K. Niemann, and J. Stuke, Heterojunctions of Amorphous Silicon and Silicon Single Crystals, in *Tetrahedrally Bonded Amorphous Semiconduc*tors: International Conference, pages 345–350, 1974.
- [53] Y. Hamakawa, K. Fujimoto, K. Okuda, Y. Kashima, S. Nonomura, and

- H. Okamoto, Applied Physics Letters 43, 644 (1983).
- [54] M. Taguchi, M. Tanaka, T. Matsuyama, T. Matsuoka, S. Tsuda, S. Nakano, Y. Kishi, and Y. Kuwano, Improvement of the conversion efficiency of polycrystalline silicon thin film solar cell, in *Technical Digest of the International* PVSEC-5, Kyoto, pages 689–692, 1990.
- [55] S. Noguchi, H. Iwata, and K. Sano, US Patent 5213628, 1993.
- [56] A. Descoeudres, Z. C. Holman, L. Barraud, S. Morel, S. De Wolf, and C. Ballif, IEEE Journal of Photovoltaics 3, 83 (2013).
- [57] S. De Wolf, A. Descoeudres, Z. C. Holman, and C. Ballif, Green 2, 7 (2012).
- [58] T. F. Schulze, L. Korte, F. Ruske, and B. Rech, Physical Review B 83, 165314 (2011).
- [59] W. Fuhs, L. Korte, and M. Schmidt, Journal of Optoelectronics and Advanced Materials 8, 1989 (2006).
- [60] S. Kirner, L. Mazzarella, L. Korte, B. Stannowski, B. Rech, and R. Schlatmann, IEEE Journal of Photovoltaics 5, 1601 (2015).
- [61] M. Mews, M. Liebhaber, B. Rech, and L. Korte, Applied Physics Letters 107, 013902 (2015).
- [62] A. Kanevce and W. K. Metzger, Journal of Applied Physics 105, 094507 (2009).
- [63] J. P. Seif, D. Menda, A. Descoeudres, L. Barraud, O. Özdemir, C. Ballif, and S. De Wolf, Journal of Applied Physics 120, 054501 (2016).
- [64] J. P. Seif, A. Descoeudres, M. Filipič, F. Smole, M. Topič, Z. Charles Holman, S. De Wolf, and C. Ballif, Journal of Applied Physics 115, 24502 (2014).
- [65] M. Taguchi, K. Kawamoto, S. Tsuge, T. Baba, H. Sakata, M. Morizane, K. Uchihashi, N. Nakamura, S. Kiyama, and O. Oota, Progress in Photovoltaics: Research and Applications 8, 503 (2000).
- [66] A. Richter, M. Hermle, and S. W. Glunz, IEEE Journal of Photovoltaics 3, 1184 (2013).
- [67] M. A. Green, Progress in Photovoltaics: Research and Applications (2017).
- [68] K. Yoshikawa, H. Kawasaki, W. Yoshida, T. Irie, K. Konishi, K. Nakano,

- T. Uto, D. Adachi, M. Kanematsu, H. Uzu, and K. Yamamoto, Nature Energy 2, 17032 (2017).
- [69] S. De Wolf, S. Olibet, and C. Ballif, Applied Physics Letters 93, 1 (2008).
- [70] A. Descoeudres, L. Barraud, R. Bartlome, G. Choong, S. De Wolf, F. Zicarelli, and C. Ballif, Applied Physics Letters 97, 4 (2010).
- [71] B. Strahm, A. A. Howling, L. Sansonnens, and C. Hollenstein, Plasma Sources Science and Technology 16, 80 (2007).
- [72] D. Deligiannis, R. Vasudevan, A. H. M. Smets, R. a. C. M. M. van Swaaij, and M. Zeman, AIP Advances 5, 097165 (2015).
- [73] M. Z. Burrows, U. K. Das, R. L. Opila, S. De Wolf, and R. W. Birkmire, Journal of Vacuum Science & Technology A: Vacuum, Surfaces, and Films 26, 683 (2008).
- [74] H. Fujiwara and M. Kondo, Applied Physics Letters 90, 013503 (2007).
- [75] S. De Wolf and M. Kondo, Applied Physics Letters 90, 042111 (2007).
- [76] L. Zhang, W. Guo, W. Liu, J. Bao, J. Liu, J. Shi, F. Meng, and Z. Liu, Journal of Physics D: Applied Physics 49, 165305 (2016).
- [77] A. Descoeudres, L. Barraud, S. De Wolf, B. Strahm, D. Lachenal, C. Guérin, Z. C. Holman, F. Zicarelli, B. Demaurex, J. P. Seif, J. Holovsky, and C. Ballif, Applied Physics Letters 99, 123506 (2011).
- [78] P. Roca i Cabarrocas, Journal of Non-Crystalline Solids 266-269, 31 (2000).
- [79] T. F. Schulze, H. N. Beushausen, C. Leendertz, A. Dobrich, B. Rech, and L. Korte, Applied Physics Letters 96, 252102 (2010).
- [80] T. Mueller, S. Schwertheim, M. Scherff, and W. R. Fahrner, Applied Physics Letters **92**, 033504 (2008).
- [81] J. Sritharathikhun, C. Banerjee, M. Otsubo, T. Sugiura, H. Yamamoto, T. Sato, A. Limmanee, A. Yamada, and M. Konagai, Japanese Journal of Applied Physics 46, 3296 (2007).
- [82] T. Mueller, S. Schwertheim, and W. R. Fahrner, Journal of Applied Physics 107, 014504 (2010).
- [83] H. Fujiwara, T. Kaneko, and M. Kondo, Applied Physics Letters 91, 3 (2007).

- [84] K. Ohdaira, T. Oikawa, K. Higashimine, and H. Matsumura, Current Applied Physics 16, 1026 (2016).
- [85] F. Einsele, W. Beyer, and U. Rau, Journal of Applied Physics 112 (2012).
- [86] H. Fujiwara and M. Kondo, Journal of Applied Physics 101, 054516 (2007).
- [87] C. Banerjee, J. Sritharathikhun, A. Yamada, and M. Konagai, Journal of Physics D: Applied Physics 41, 185107 (2008).
- [88] J. Sritharathikhun, F. Jiang, S. Miyajima, A. Yamada, and M. Konagai, Japanese Journal of Applied Physics 48, 101603 (2009).
- [89] K. Ding, U. Aeberhard, V. Smirnov, B. Holländer, F. Finger, and U. Rau, Japanese Journal of Applied Physics **52**, 122304 (2013).
- [90] L. Mazzarella, S. Kirner, O. Gabriel, L. Korte, B. Stannowski, B. Rech, and R. Schlatmann, Nanocrystalline Silicon Oxide Emitters for Silicon Hetero Junction Solar Cells, in *Energy Procedia*, volume 77, pages 304–310, 2015.
- [91] L. Mazzarella, S. Kirner, O. Gabriel, S. S. Schmidt, L. Korte, B. Stannowski, B. Rech, and R. Schlatmann, Physica Status Solidi (A) 7, 1 (2016).
- [92] J. Bullock, M. Hettick, J. Geissbühler, A. J. Ong, T. Allen, C. M. Sutter-Fella, T. Chen, H. Ota, E. W. Schaler, S. De Wolf, C. Ballif, A. Cuevas, and A. Javey, Nature Energy, 15031 (2016).
- [93] M. Mews, L. Korte, and B. Rech, Solar Energy Materials and Solar Cells 158, 77 (2016).
- [94] M. Balestrieri, D. Pysch, J.-P. Becker, M. Hermle, W. Warta, and S. Glunz, Solar Energy Materials and Solar Cells 95, 2390 (2011).
- [95] S. Kirner, M. Hartig, L. Mazzarella, L. Korte, T. Frijnts, H. Scherg-Kurmes, S. Ring, B. Stannowski, B. Rech, and R. Schlatmann, The influence of ITO dopant density on J-V Characteristics of silicon heterojunction solar cells: experiments and simulations, in *Energy Procedia*, volume 77, pages 725–732, 2015.
- [96] Z. C. Holman, A. Descoeudres, L. Barraud, F. Z. Fernandez, J. P. Seif, S. De Wolf, and C. Ballif, IEEE Journal of Photovoltaics 2, 7 (2012).
- [97] Z. C. Holman, M. Filipič, A. Descoeudres, S. De Wolf, F. Smole, M. Topič,

- and C. Ballif, Journal of Applied Physics 113, 1 (2013).
- [98] L. Barraud, Z. C. Holman, N. Badel, P. Reiss, A. Descoeudres, C. Battaglia, S. De Wolf, and C. Ballif, Solar Energy Materials and Solar Cells 115, 151 (2013).
- [99] M. Morales-Masis, S. M. De Nicolas, J. Holovsky, S. De Wolf, and C. Ballif, IEEE Journal of Photovoltaics 5, 1340 (2015).
- [100] H. Savin, P. Repo, G. von Gastrow, P. Ortega, E. Calle, M. Garín, and R. Alcubilla, Nature Nanotechnology 10, 624 (2015).
- [101] J. Oh, H.-C. Yuan, and H. M. Branz, Nature Nanotechnology 7, 2 (2012).
- [102] M. Smeets, K. Bittkau, F. Lentz, A. Richter, K. Ding, R. Carius, U. Rau, and U. W. Paetzold, Nanoscale 8, 18726 (2016).
- [103] M. Lammert and R. Schwartz, IEEE Transactions on Electron Devices 24, 337 (1977).
- [104] Kaneka Corporation, World's Highest Conversion Efficiency of 26.33% Achieved in a Crystalline Silicon Solar Cell, 2016.
- [105] G. Coletti, F. Ishimura, Y. Wu, E. E. Bende, G. Janssen, B. van Aken, K. Hashimoto, and Y. Watabe, 23% Efficiency metal wrap through silicon heterojunction solar cells, in 43rd IEEE Photovoltaic Specialists Conference (PVSC), pages 2417–2420, IEEE, 2016.
- [106] C. Battaglia, S. M. de Nicolas, S. De Wolf, X. Yin, M. Zheng, C. Ballif, and A. Javey, Hole Selective MoOx Contact for Silicon Heterojunction Solar Cells, in 40th IEEE Photovoltaic Specialist Conference (PVSC), pages 968–70, 2014.
- [107] M. Meier, U. W. Paetzold, M. Prömpers, T. Merdzhanova, R. Carius, and A. Gordijn, Progress in Photovoltaics: Research and Applications 22, 1226 (2013).
- [108] S. Kim, H. Lee, J.-W. Chung, S.-W. Ahn, and H.-M. Lee, Current Applied Physics 13, 743 (2013).
- [109] V. Smirnov, A. Lambertz, and F. Finger, Electronic and Structural Properties of n-type Microcrystalline Silicon Oxide Films for Applications in Thin Film Silicon Solar Cells, in *Energy Procedia*, volume 84, pages 71–77, 2015.

- [110] Y. Hishikawa, N. Nakamura, S. Tsuda, S. Nakano, Y. Kishi, and Y. Kuwano, Japanese Journal of Applied Physics 30, 1008 (1991).
- [111] D. Ritter and K. Weiser, Optics Communications 57, 336 (1986).
- [112] K. Ding, Nanostructured Si-alloys for silicon solar cells, PhD thesis, RWTH Aachen, 2014.
- [113] A. A. Langford, M. L. Fleet, B. P. Nelson, W. A. Lanford, and N. Maley, Physical Review B 45, 13367 (1992).
- [114] L. He, T. Inokuma, Y. Kurata, and S. Hasegawa, Journal of Non-Crystalline Solids 185, 249 (1995).
- [115] D. V. Tsu, G. Lucovsky, and B. N. Davidson, Physical Review B 40, 1795 (1989).
- [116] E. San Andrés, A. del Prado, I. Mártil, G. González-Díaz, D. Bravo, F. J. López, M. Fernández, W. Bohne, J. Röhrich, B. Selle, and I. Sieber, Journal of Applied Physics 94, 7462 (2003).
- [117] L.-N. He, D.-M. Wang, and S. Hasegawa, Journal of Non-Crystalline Solids **261**, 67 (2000).
- [118] H. Curtins and S. Veprek, Solid State Communications 57, 215 (1986).
- [119] H. Wagner and W. Beyer, Solid State Communications 48, 585 (1983).
- [120] T. Jana, S. Mukhopadhyay, and S. Ray, Solar Energy Materials and Solar Cells 71, 197 (2002).
- [121] G. Lucovsky, J. Yang, S. S. Chao, J. E. Tyler, and W. Czubatyj, Physical Review B 28, 3225 (1983).
- [122] J. Kočka, H. Stuchlíková, M. Ledinský, J. Stuchlík, T. Mates, and A. Fejfar, Solar Energy Materials and Solar Cells 93, 1444 (2009).
- [123] N. B. Colthup, L. H. Daly, and S. E. Wiberley, Introduction to Infrared and Raman Spectroscopy, Academic Press, Inc., 2nd edition, 1975.
- [124] W. Zhang, S. Zhang, Y. Liu, and T. Chen, Journal of Crystal Growth 311, 1296 (2009).
- [125] A. Lambertz, A. Dasgupta, W. Reetz, A. Gordijn, R. Carius, and F. Finger, Microcrystalline Silicon Oxide As Intermediate Reflector For Thin Film Silicon

- Solar Cells, in 22nd European Photovoltaic Solar Energy Conference, pages 1839–1842, 2007.
- [126] B. Gault, M. O. Moody, J. M. Cairney, and S. P. Ringer, *Atom Probe Microscopy*, Springer, 2012.
- [127] T. Kinno, M. Tomita, T. Ohkubo, S. Takeno, and K. Hono, Applied Surface Science 290, 194 (2014).
- [128] M. K. Miller and R. G. Forbes, Materials Characterization 60, 461 (2009).
- [129] T. F. Kelly and M. K. Miller, Review of Scientific Instruments 78 (2007).
- [130] H. Schumann and H. Oettel, Metallografie, Wiley-VCH, 2005.
- [131] Sinton-Instruments, User Manual v3.0 Photoconductance Lifetime Tester WCT-120, 2013.
- [132] M. A. Green, K. Emery, Y. Hishikawa, W. Warta, and E. D. Dunlop, Progress in Photovoltaics: Research and Applications 20, 12 (2012).
- [133] S. C. Baker-Finch and K. R. McIntosh, A freeware model for precise optical analysis of the front surface of a solar cell, in 35th IEEE photovoltaics specialists conference, pages 2184–2187, 2010.
- [134] K. R. McIntosh and S. C. Baker-finch, OPAL 2: rapid optical simulation of silicon solar cells, in 38th IEEE Photovoltaic Specialists Conference, page 000265, 2012.
- [135] F. Finger, P. Hapke, M. Luysberg, R. Carius, H. Wagner, and M. Scheib, Applied Physics Letters 65, 2588 (1994).
- [136] M. Kondo, M. Fukawa, L. Guo, and A. Matsuda, Journal of Non-Crystalline Solids 266-269, 84 (2000).
- [137] X. J. Hao, E.-C. Cho, C. Flynn, Y. S. Shen, G. Conibeer, and M. A. Green, Nanotechnology 19, 424019 (2008).
- [138] R. Saleh and N. H. Nickel, Applied Surface Science 254, 580 (2007).
- [139] M. Bailly, J. V. Carpenter III, Z. C. Holman, and S. Bowden, Substrate Dependent Growth of Microcrystalline Silicon, in 40th IEEE Photovoltaic Specialist Conference (PVSC), pages 1201–1205, 2014.
- [140] S. M. Iftiquar, Journal of Physics D: Applied Physics 31, 1630 (1998).

- [141] S. Kirner, O. Gabriel, B. Stannowski, B. Rech, and R. Schlatmann, Applied Physics Letters 102, 051906 (2013).
- [142] K. Haga and H. Watanabe, Journal of Non-Crystalline Solids 195, 72 (1996).
- [143] M. Heintze, R. Zedlitz, and G. H. Bauer, Journal of Physics D: Applied Physics 26, 1781 (1993).
- [144] U. Kroll, A. Shah, H. Keppner, J. Meier, P. Torres, and D. Fischer, Solar Energy Materials and Solar Cells 48, 343 (1997).
- [145] M. Petersen, M. T. Schulberg, and L. A. Gochberg, Applied Physics Letters 82, 2041 (2003).
- [146] A. Hohl, T. Wieder, P. A. van Aken, T. E. Weirich, G. Denninger, M. Vidal, S. Oswald, C. Deneke, J. Mayer, and H. Fuess, Journal of Non-Crystalline Solids 320, 255 (2003).
- [147] A. Matsuda, Thin Solid Films **337**, 1 (1999).
- [148] R. Janssen, A. Janotta, D. Dimova-Malinovska, and M. Stutzmann, Phys. Rev. B 60, 13561 (1999).
- [149] Y.-R. Luo and J.-P. Cheng, Bond Dissociation Energies, in *CRC Handbook of Chemistry and Physics*, pages 65–98, 2007.
- [150] A. Lambertz, F. Finger, B. Hollaender, J. Rath, and R. Schropp, Journal of Non-Crystalline Solids 358, 1962 (2012).
- [151] E. Talbot, R. Lardé, F. Gourbilleau, C. Dufour, and P. Pareige, EPL (Europhysics Letters) 87, 26004 (2009).
- [152] X. Pi, Journal of Nanomaterials **2012**, 1 (2012).
- [153] J. S. Custer, M. O. Thompson, D. C. Jacobson, J. M. Poate, S. Roorda, W. C. Sinke, and F. Spaepen, Applied Physics Letters 64, 437 (1994).
- [154] H. Fritzsche, M. Tanielian, C. C. Tsai, and P. J. Gaczi, Journal of Applied Physics 50, 3366 (1979).
- [155] Z. Remeš, M. Vaněček, P. Torres, U. Kroll, A. Mahan, and R. Crandall, Journal of Non-Crystalline Solids 227-230, 876 (1998).
- [156] P. Roca i Cabarrocas, N. Layadi, T. Heitz, B. Drévillon, and I. Solomon, Applied Physics Letters 66, 3609 (1995).

- [157] O. Vetterl, F. Finger, R. Carius, P. Hapke, L. Houben, O. Kluth, A. Lambertz, A. Mück, B. Rech, and H. Wagner, Solar Energy Materials and Solar Cells 62, 97 (2000).
- [158] N. Pellaton-Vaucher, B. Rech, D. Fischer, S. Dubail, M. Goetz, H. Keppner, N. Wyrsch, C. Beneking, O. Hadjadj, V. Shklover, and A. Shah, Solar Energy Materials and Solar Cells 49, 27 (1997).
- [159] A. Samanta and D. Das, Applied Surface Science 259, 477 (2012).
- [160] Y. Matsumoto, V. Sánchez R., and A. Avila G., Thin Solid Films 516, 593 (2008).
- [161] F. Einsele, Amorphe Siliziumoxidschichten zur Oberflächenpassivierung und Kontaktierung von Heterostruktur-Solarzellen aus amorphem und kristallinem Silizium, PhD thesis, RWTH Aachen, 2010.
- [162] H. P. Zhou, D. Y. Wei, S. Xu, S. Q. Xiao, L. X. Xu, S. Y. Huang, Y. N. Guo, S. Khan, and M. Xu, Journal of Physics D: Applied Physics 45, 395401 (2012).
- [163] J. Hotovy, J. Hüpkes, W. Böttler, E. Marins, L. Spiess, T. Kups, V. Smirnov, I. Hotovy, and J. Kováč, Applied Surface Science 269, 81 (2013).
- [164] M. Bivour, S. Schröer, M. Hermle, and S. W. Glunz, Solar Energy Materials and Solar Cells 122, 120 (2014).
- [165] S. De Wolf, C. Ballif, and M. Kondo, Physical Review B 85, 2 (2012).
- [166] E. Yablonovitch, D. L. Allara, C. C. Chang, T. Gmitter, and T. B. Bright, Physical Review Letters 57, 249 (1986).
- [167] M. W. M. van Cleef, F. A. Rubinelli, R. Rizzoli, R. Pinghini, R. E. I. Schropp, and W. F. van der Weg, Japanese Journal of Applied Physics 37, 3926 (1998).
- [168] J. P. Seif, A. Descoeudres, G. Nogay, S. Hanni, S. M. de Nicolas, N. Holm, J. Geissbuhler, A. Hessler-Wyser, M. Duchamp, R. E. Dunin-Borkowski, M. Ledinsky, S. De Wolf, and C. Ballif, IEEE Journal of Photovoltaics 6, 1132 (2016).
- [169] M. A. Green, Solar Energy Materials and Solar Cells 92, 1305 (2008).
- [170] C. Trompoukis, I. Abdo, R. Cariou, I. Cosme, W. Chen, O. Deparis,

- A. Dmitriev, E. Drouard, M. Foldyna, E. G. Caurel, I. Gordon, B. Heidari, A. Herman, L. Lalouat, K.-D. Lee, J. Liu, K. Lodewijks, F. Mandorlo, I. Massiot, A. Mayer, V. Mijkovic, J. Muller, R. Orobtchouk, G. Poulain, P. Prod'Homme, P. R. I. Cabarrocas, C. Seassal, J. Poortmans, R. Mertens, O. E. Daif, and V. Depauw, Physica Status Solidi (A) 212, 140 (2015).
- [171] J. Gjessing, E. S. Marstein, and A. Sudbø, Optics express 18, 5481 (2010).
- [172] J. Thorstensen, J. Gjessing, E. S. Marstein, and S. E. Foss, IEEE Journal of Photovoltaics 3, 709 (2013).
- [173] A. Mellor, H. Hauser, C. Wellens, J. Benick, J. Eisenlohr, M. Peters, A. Guttowski, I. Tobías, A. Martí, A. Luque, and B. Bläsi, Optics Express 21, A295 (2013).
- [174] F. Lindholm, J. Fossum, and E. Burgess, IEEE Transactions on Electron Devices 26, 165 (1979).
- [175] M. G. Kang, S. Tark, J. C. Lee, C.-S. Son, and D. Kim, Journal of Crystal Growth 326, 14 (2011).
- [176] B. Stegemann, J. Kegel, M. Mews, E. Conrad, L. Korte, U. Stürzebecher, and H. Angermann, Passivation of Textured Silicon Wafers: Influence of Pyramid Size Distribution, a-Si:H Deposition Temperature, and Post-treatment, in Energy Procedia, volume 38, pages 881–889, 2013.
- [177] L. Wang, F. Wang, X. Zhang, N. Wang, Y. Jiang, Q. Hao, and Y. Zhao, Journal of Power Sources 268, 619 (2014).
- [178] S. Olibet, E. Vallat-Sauvain, L. Fesquet, C. Monachon, A. Hessler-Wyser, J. Damon-Lacoste, S. De Wolf, and C. Ballif, Properties of interfaces in amorphous/crystalline silicon heterojunctions, PhD thesis, 2009.
- [179] S. De Wolf, Intrinsic and Doped a -Si:H/c-Si Interface, in Physics and Technology of Amorphous-Crystalline Heterostructure Silicon Solar Cells, pages 223–259, 2012.
- [180] S. C. Baker-Finch and K. R. McIntosh, IEEE Journal of Photovoltaics 1, 59 (2011).
- [181] S. Olibet, E. Vallat-Sauvain, L. Fesquet, C. Monachon, A. Hessler-Wyser,

- J. Damon-Lacoste, S. De Wolf, and C. Ballif, Physica Status Solidi (A) 207, 651 (2010).
- [182] A. B. Sproul, Journal of Applied Physics **76**, 2851 (1994).
- [183] J. Ge, M. Tang, J. Wong, Z. Zhang, T. Dippell, M. Doerr, O. Hohn, M. Huber, P. Wohlfart, A. G. Aberle, and T. Mueller, International Journal of Photoenergy 2014, 752967 (2014).
- [184] M. Taguchi, A. Terakawa, E. Maruyama, and M. Tanaka, Progress in Photovoltaics: Research and Applications 13, 481 (2005).
- [185] M. Tzolov, F. Finger, R. Carius, and P. Hapke, Journal of Applied Physics 81, 7376 (1997).
- [186] M. Steltenpool, J. Rutten, A. Tavakoliyaraki, H. de Groot, G. van der Hofstad, W. Vugts, A. J. M. van Erven, and G. Rajeswaran, High efficient commercial grade crystalline silicon solar cells with thin film amorphous silicon passivation, in 27th European Photovoltaic Solar Energy Conference and Exhibition, pages 1673–1676, 2012.
- [187] S. C. Baker-Finch and K. R. Mcintosh, Progress in Photovoltaics: Research and Applications 19, 406 (2011).
- [188] M. S. Branham, W.-C. Hsu, S. Yerci, J. Loomis, S. V. Boriskina, B. R. Hoard, S. E. Han, A. Ebong, and G. Chen, Advanced Optical Materials 4, 858 (2016).
- [189] V. Smirnov, S. Reynolds, F. Finger, R. Carius, and C. Main, Journal of Non-Crystalline Solids 352, 1075 (2006).
- [190] M. Günes, H. Cansever, G. Yilmaz, V. Smirnov, F. Finger, and R. Brügge-mann, Journal of Non-Crystalline Solids 358, 2074 (2012).
- [191] E. Kobayashi, S. De Wolf, J. Levrat, G. Christmann, A. Descoeudres, S. Nicolay, M. Despeisse, Y. Watabe, and C. Ballif, Applied Physics Letters 109, 153503 (2016).
- [192] D. L. Staebler and C. R. Wronski, Applied Physics Letters 31, 292 (1977).
- [193] K. Ding, M. Pomaska, A. Singh, F. Lentz, F. Finger, and U. Rau, Physica Status Solidi (RRL) - Rapid Research Letters 10, 233 (2016).

Acknowledgments

The number of people who contributed directly or indirectly to the completion of this work was growing by the day and it is impossible to name all of them here. Nevertheless, I will try to acknowledge at least some of them in the following:

- Dr. Kaining Ding for introducing me to the world of nc-SiO_x:H films and SHJ solar cells, for his relentless encouragement and guidance, and most importantly for keeping the door open for his PhD students even in the busiest of times.
- Prof. Dr. Uwe Rau for the opportunity to work on this exciting topic at the IEK-5 and for supervising and evaluating this thesis.
- Prof. Dr. Joachim Knoch for surveying this thesis.
- \bullet Dr. Vladimir Smirnov for proof reading the manuscript and for valuable discussions on nc-SiO $_{\rm x}$: H.
- The many people who actively participated in sample preparation and characterization: Dr. Lei Zhao, Kamil Janosz, and Silke Lynen for countless depositions; Johannes Wolff and Andreas Schmalen for their support at the CT-1; Manuela Meyer for all the ITO and a-Si:H depositions and her assistance in wafer cleaning; Dr. Florian Lentz for performing the NIL imprints and for SEM imaging; Oliver Thimm and Josef Klomfaß for PDS measurements; Christoph Zaren, Sabine Kasper, Wilfried Reetz, Thomas Birrenbach, and Dr. Li Ding for assistance with the solar simulator and the DSR setup; Sandra Moll and Dr. Andreas Lambertz for depositions at the 6K system; Keita Nomoto from the UNSW for performing the APT measurements.
- Michael Smeets for a fruitful collaboration on NIL based light trapping concepts in planar SHJ solar cells.

Acknowledgments

- All the colleagues at the IEK-5 for a great working atmosphere and all the valuable scientific as well as non-scientific discussions. Especially, I would like to thank Dr. Wolfhard Beyer, Dr. Bart Pieters, Dr. Karsten Bittkau, Dr. Yael Augarten, and Dr. Friedhelm Finger for precious suggestions and feedback.
- The PhD students at the IEK-5 for creating so many unforgettable moments during the conference visits and a great team spirit, especially regarding the football matches (Go, Photonensturm!).
- The SHJ group of the IEK-5 for fruitful discussions during our group meetings and many cakes and cookies.
- Manuel Pomaska, Florian Staub, and Florian Lentz, aka "Büro-Atzen", for being great colleagues and friends and for several enjoyable Kicker sessions.
- All the players from the BSG FZJ volleyball group for creating a well-needed counterbalance to the daily work and for all the exciting games we shared.
- Dr. Aude Berbezier, Aryak Singh, and Flaviano Dos Santos for being wonderful flat-mates and irreplaceable friends.
- \bullet Maria for all her support and for offering refuge in times of exhaustion.
- Lastly, my warmest thanks and deepest gratitude go to my parents, David and Elwira, my brother, Sergei, and my sister, Nicole, for supporting my ambitions and always believing in me.

Schriften des Forschungszentrums Jülich Reihe Energie & Umwelt / Energy & Environment

Band / Volume 403

Spatio-Temporal Estimation and Validation of Remotely Sensed Vegetation and Hydrological Fluxes in the Rur Catchment, Germany

M. Ali (2018), xvi, 116 pp ISBN: 978-3-95806-287-0

Band / Volume 404

Thermomechanical Characterization of Advanced Ceramic Membrane Materials

Y. Zou (2018), xvi, 168 pp ISBN: 978-3-95806-288-7

Band / Volume 405

Betrachtung der Kristallinitätsentwicklung in mikrokristallinem Dünnschicht-Silizium mit in-situ Raman-Spektroskopie

T. Fink (2018), XI, 166 pp ISBN: 978-3-95806-289-4

Band / Volume 406

Institute of Energy and Climate Research IEK-6: Nuclear Waste Management Report 2015 / 2016

Material Science for Nuclear Waste Management S. Neumeier, H. Tietze-Jaensch, D. Bosbach (Eds.) (2018), 221 pp

ISBN: 978-3-95806-293-1

Band / Volume 407

Reduction properties of a model ceria catalyst at the microscopic scale

J. Hackl (2018), VIII, 98 pp ISBN: 978-3-95806-294-8

Band / Volume 408

Comparative Analysis of Infrastructures:

Hydrogen Fueling and Electric Charging of Vehicles

M. Robinius, J. Linßen, T. Grube, M. Reuß, P. Stenzel, K. Syranidis, P. Kuckertz and D. Stolten (2018), VII, 108 pp

ISBN: 978-3-95806-295-5

Band / Volume 409

Reactions between nitrite and soil organic matter and their role in nitrogen trace gas emissions and nitrogen retention in soil

J. Wei (2018), XXII, 160 pp ISBN: 978-3-95806-299-3

Schriften des Forschungszentrums Jülich Reihe Energie & Umwelt / Energy & Environment

Band / Volume 410

The impact of soil water distribution on root development and root water uptake of winter wheat

G. Cai (2018), xviii, 143 pp ISBN: 978-3-95806-303-7

Band / Volume 411

Charakterisierung und Optimierung der Grenzfläche Elektrolyt/Kathode in metallgestützten Festelektrolyt-Brennstoffzellen

D. Udomsilp (2018), XI, 176 pp ISBN: 978-3-95806-304-4

Band / Volume 412

Formation of Secondary Organic Aerosol from Photo-Oxidation of Benzene: a Chamber Study

S. H. Schmitt (2018), III, 250 pp ISBN: 978-3-95806-305-1

Band / Volume 413

Mechanismen der chrombasierten Degradation von metallgestützten Festoxid-Brennstoffzellen

A. Beez (2018), VIII, 144 pp ISBN: 978-3-95806-306-8

Band / Volume 414

Entwicklung eines Werkzeugs zur Modellierung der Nettoerosion im Hauptraum der Brennkammer eines Tokamaks und Studium der Plasma-Wand-Wechselwirkung an DEMO1

M. Beckers (2018), XIX, 150 pp ISBN: 978-3-95806-307-5

Band / Volume 415

Fehlstellendotierung von Eisenoxid- und Bismutsulfid-Nanopartikeln

J. P. Mock (2018), v, 187 pp ISBN: 978-3-95806-309-9

Band / Volume 416

Nanocrystalline Silicon Oxide in Silicon Heterojunction Solar Cells

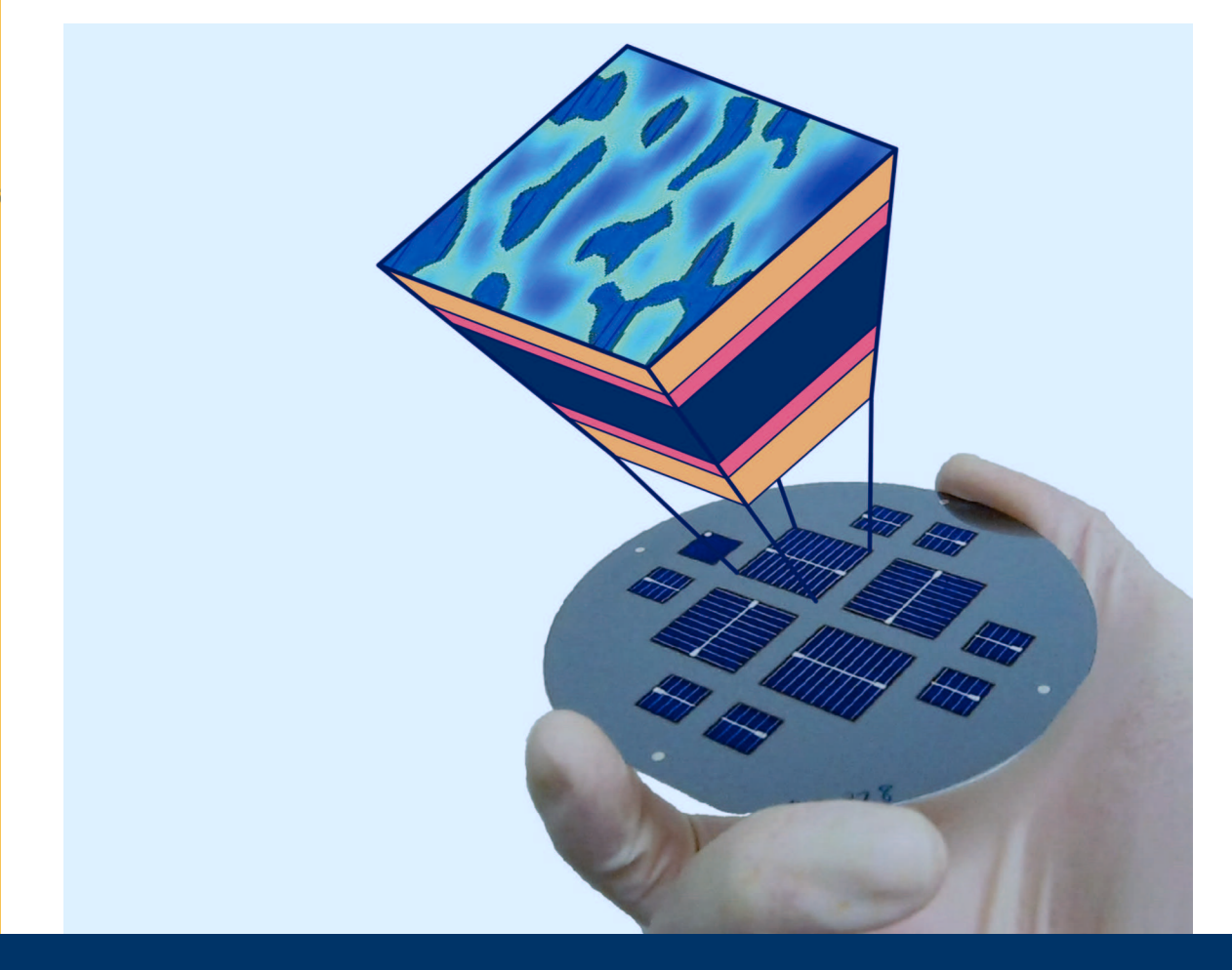
A. Richter (2018), 166 pp ISBN: 978-3-95806-310-5

Weitere Schriften des Verlags im Forschungszentrum Jülich unter

http://wwwzb1.fz-juelich.de/verlagextern1/index.asp

Energie & Umwelt Energy & Environment

Nanocrystalline Silicon Oxide in SHJ Solar Cells



416

Nanocrystalline Silicon Oxide in Silicon Heterojunction Solar Cells

Alexei Richter

Energie & Umwelt / Energy & Environment Band / Volume 416 ISBN 978-3-95806-310-5

xei Richte

Energie & Umwelt / Energy & Environment Band / Volume 416 ISBN 978-3-95806-310-5





